

Electronic Thesis and Dissertation Repository

---

4-23-2018 10:00 AM

## On the Reduction of the Driving Force in Shear-driven Flows

Sakib Shadman

*The University of Western Ontario*

Supervisor

Floryan, Jerzy M.

*The University of Western Ontario*

Graduate Program in Mechanical and Materials Engineering

A thesis submitted in partial fulfillment of the requirements for the degree in Master of Engineering Science

© Sakib Shadman 2018

Follow this and additional works at: <https://ir.lib.uwo.ca/etd>



Part of the [Aerodynamics and Fluid Mechanics Commons](#), [Fluid Dynamics Commons](#), and the [Heat Transfer, Combustion Commons](#)

---

### Recommended Citation

Shadman, Sakib, "On the Reduction of the Driving Force in Shear-driven Flows" (2018). *Electronic Thesis and Dissertation Repository*. 5289.

<https://ir.lib.uwo.ca/etd/5289>

This Dissertation/Thesis is brought to you for free and open access by Scholarship@Western. It has been accepted for inclusion in Electronic Thesis and Dissertation Repository by an authorized administrator of Scholarship@Western. For more information, please contact [wlsadmin@uwo.ca](mailto:wlsadmin@uwo.ca).

## **Abstract**

In shear-driven flows, an external driving force is needed to maintain the relative movement of horizontal plates. This thesis presents a systematic analysis on using spatially periodic heating and grooved surfaces to control this force. It is found that the use of periodic heating creates a buoyancy-driven effect that always reduces this force. The use of proper heating may even lead to the complete elimination of this force. It is further found that the use of isothermal grooved surfaces always enhances flow resistance, resulting in an increase of this force. When grooves and heating are applied together, their interaction induces a horizontal pressure force that can either increase or decrease the driving force, depending on the relative positions of the groove and heating patterns. Mechanisms leading to such changes of the driving force are discussed.

## **Keywords**

Flow control, Drag reduction, Force reduction, Shear flow, Couette flow, Low Reynolds number flows, Periodic heating, Spatial heating, Grooves, Surface irregularities.

## **Acknowledgments**

Firstly, I would like to thank my supervisor Prof. J. M. Floryan for his precious time and continuous support throughout my Masters. It is difficult to overstate my gratitude to him for his patience, motivation, and enthusiasm. The completion of this work would not have been possible without his immense knowledge, invaluable guidance, incomparable suggestions, and constructive discussions.

I would like to extend my heartiest appreciation to my advisory committee member, Prof. A. G. Straatman for his insightful comments. His curiosities in this project made me think about various aspects and applications of the research outcome.

I am also deeply indebted to Dr. Mohammad Zakir Hossain and Seyed Arman Abtahi. It would have been very difficult for me to finish my Masters without their help. Dr. Hossain has been more than helpful with his precious time for explaining to me the various physical concepts, his suggestions and guidance in writing and his contributions for verifying the results. I would also like to thank Arman for providing the primary framework for the solver and explaining me its potential capacity.

I would also like to thank all my colleagues (past and present), Dr. Hadi Vafadar Moradi, Dr. Alireza Mohammadi, Yanbei Wang for their friendship, cooperation, and helpful attitude.

Finally, I would like to mention that this work has been carried out with financial support from the Natural Sciences and Engineering Research Council (NSERC) of Canada.

# Table of Contents

<b>Abstract</b> .....	i
<b>Acknowledgments</b> .....	ii
<b>Table of Contents</b> .....	iii
<b>List of Figures</b> .....	vi
<b>List of Appendices</b> .....	xiv
<b>List of Abbreviations and Nomenclature</b> .....	xv
<b>Chapter 1</b> .....	1
<b>1 Introduction</b> .....	1
1.1 Objective.....	1
1.2 Motivation.....	2
1.3 Related literature survey .....	3
1.3.1 Effects of surface irregularities.....	3
1.3.2 Effects of heating irregularities.....	6
1.4 Outline of the present work.....	9
<b>Chapter 2</b> .....	10
<b>2 Model Problem</b> .....	10
2.1 Geometry.....	10
2.2 Heating pattern.....	11
2.3 Governing equations .....	12
2.4 Boundary conditions .....	13
2.5 Flow constraint.....	14
2.6 Reference isothermal case.....	14
2.7 Driving force.....	15
2.8 Flow rate .....	15

2.9 Heat transfer.....	15
<b>Chapter 3</b> .....	16
<b>3 Solution procedure</b> .....	16
3.1 Stream function formulation.....	16
3.2 Treatment of the irregular geometry.....	17
3.3 Field equations in the computational plane .....	18
3.4 Discretization of the field equations .....	18
3.5 Discretization of the boundary conditions .....	21
3.6 Discretization of the pressure gradient constraint.....	24
3.7 Numerical solution.....	25
<b>Chapter 4</b> .....	27
<b>4 Flow between heated smooth parallel plates in relative motion</b> .....	27
4.1 Purely periodic heating at the lower plate.....	28
4.2 Plates with unequal mean temperatures.....	39
4.3 Effects of the Prandtl number .....	40
4.4 Heat transfer effects .....	42
4.5 Heating of the upper plate.....	44
4.6 Summary.....	45
<b>Chapter 5</b> .....	47
<b>5 Flow between grooved isothermal plates in relative motion</b> .....	47
5.1 Flow geometry .....	47
5.2 Driving force applied to the moving plate .....	48
5.3 Sinusoidal grooves.....	49
5.4 Arbitrary grooves.....	52
5.5 Summary.....	56
<b>Chapter 6</b> .....	58

<b>6 Flow between heated grooved plates in relative motion .....</b>	<b>58</b>
6.1 Effects of the phase difference.....	59
6.2 Effects of the wavenumber .....	65
6.3 Effects of the Reynolds number.....	67
6.4 Effects of the groove amplitude.....	69
6.5 Effects of the heating intensity .....	72
6.6 Effects of the plates' mean temperature.....	74
6.7 Effects of the Prandtl number .....	75
6.8 Heat transfer effects .....	77
6.9 Summary.....	80
<b>Chapter 7 .....</b>	<b>81</b>
<b>7 Conclusions and Recommendations .....</b>	<b>81</b>
7.1 Conclusions.....	81
7.2 Future recommendations.....	83
<b>References .....</b>	<b>85</b>
<b>Appendices.....</b>	<b>94</b>
<b>Curriculum Vitae .....</b>	<b>97</b>

## List of Figures

**Figure 1-1:** Applications of shear-driven flow in (A) coating processes (Figure from (Durst, 2008)), (B) fluid movement in bearings (Figure from (Ashihara & Hashimoto, 2010))..... 2

**Figure 2-1:** Schematic diagram of the flow system. .... 11

**Figure 4-1:** Schematic diagram of the flow system ..... 27

**Figure 4-2:** The flow and temperature fields for  $Ra_p = 1000$ ,  $Pr = 0.71$ ,  $Ra_{uni} = 0$ ,  $\alpha = 2$  and (A)  $Re = 0$ , (B)  $Re = 1$ , (C)  $Re = 5$ , (D)  $Re = 50$ . Solid and dashed lines identify streamlines and isotherms, respectively. Thick streamlines mark borders of bubbles trapping the fluid. Enlargement of the box shown in Figure 4-2B is displayed in Figure 4-3. Flow conditions used in these plots are marked in Figure 4-10 using squares. .... 30

**Figure 4-3:** Enlargement of the box shown in Figure 4-2B. The streamline emanating from the in-flow stagnation points corresponds to  $\psi = 0.286322$ . .... 30

**Figure 4-4:** Variations of the local  $|\psi_{max}|$  associated with the upper plate (solid line), the clockwise rolls (dashed line), and the counterclockwise rolls (dashed-dotted line) as functions of  $Re$  for  $\alpha = 2$ ,  $Ra_p = 1000$ ,  $Pr = 0.71$ ,  $Ra_{uni} = 0$ . .... 31

**Figure 4-5:** Distribution of the shear stress  $\tau_U$  acting on the upper plate for  $\alpha = 2$ ,  $Ra_p = 1000$ ,  $Pr = 0.71$ ,  $Ra_{uni} = 0$  at  $Re = 1$  (solid line) and  $Re = 10$  (dashed line). Enlargement of the box shown in Figure 4-5A is displayed in Figure 4-5B including shear mean values. .... 32

**Figure 4-6:** Variations of  $\Delta F/Re$  as a function of  $\alpha$  for  $Pr = 0.71$ ,  $Ra_{uni} = 0$ ,  $Re = 1$  (solid lines) and  $Re = 10$  (dashed lines). Thin dotted lines identify asymptotes. The shaded area identifies conditions where the driving force must change direction and becomes a braking force. .... 32

**Figure 4-7:** The flow and temperature fields for  $Ra_p = 1000$ ,  $Pr = 0.71$ ,  $Ra_{uni} = 0$ ,  $Re = 1$  and  $\alpha = 1$  (A),  $\alpha = 5$  (B),  $\alpha = 8$  (C),  $\alpha = 10$  (D). Thick solid lines identify streamlines, thin solid lines identify negative isotherms while thin dashed lines identify positive isotherms. Thick streamlines mark borders of various bubbles trapping the fluid. .... 34

**Figure 4-8:** Variations of change of the flow rate driven by movement of the upper plate  $\Delta Q/Re$  as a function of  $\alpha$  for  $Pr = 0.71$ ,  $Ra_{uni} = 0$ ,  $Re = 1$  (solid lines) and  $Re = 10$  (dashed lines). Thin dotted lines identify asymptotes. Dashed-dotted line identifies the negative values of  $\Delta Q$  for  $Ra_p = 2000$ ,  $Re = 1$ . ..... 34

**Figure 4-9:** The flow and temperature fields for  $Ra_p = 2000$ ,  $Pr = 0.71$ ,  $Ra_{uni} = 0$ ,  $Re = 1$ ,  $\alpha = 0.25$ . Enlargement of the box in Figure 4-9A is displayed in Figure 4-9B. Thick solid lines identify streamlines, thin solid lines identify negative isotherms while thin dashed lines identify positive isotherms. Thick streamlines mark borders of various bubbles trapping the fluid. .. 35

**Figure 4-10:** Variations of (A)  $\Delta F$  and (B)  $\Delta Q$  as functions of  $Re$  for  $Pr = 0.71$ ,  $Ra_{uni} = 0$ ,  $\alpha = 2$  (solid lines) and  $\alpha = 1$  (dashed lines). Thin dotted lines identify asymptotes. Plots of flow and temperature field for conditions identified using squares are displayed in Figure 4-2. See text for other details. The shaded area in Figure 4-10A identifies conditions where the driving force must change direction and becomes a braking force. .... 36

**Figure 4-11:** Variations of (A)  $\Delta F$  and (B)  $\Delta Q$  as functions of  $Ra_p$  for  $Pr = 0.71$ ,  $Ra_{uni} = 0$ ,  $Re = 1$  (solid lines) and  $Re = 10$  (dashed lines). Plots of flow and temperature fields for conditions identified using squares are displayed in Figure 4-12. See text for other details. The shaded area identifies conditions where the driving force must change direction and becomes a braking force when  $Re = 1$  and the double shaded area identifies such conditions for  $Re = 10$ . .... 37

**Figure 4-12:** The flow and temperature fields for  $Re = 1$ ,  $Pr = 0.71$ ,  $Ra_{uni} = 0$ ,  $\alpha = 2$  at (A)  $Ra_p = 500$ , (B)  $Ra_p = 1000$ , (C)  $Ra_p = 2000$  and (D)  $Ra_p = 3000$ . Thick solid lines identify streamlines, thin solid lines identify negative isotherms while thin dashed lines identify positive isotherms. Thick streamlines mark borders of various bubbles trapping the fluid. Flow conditions used in these plots are marked in Figure 4-11 using squares. .... 38

**Figure 4-13:** Variations of  $\Delta F/Re$  as a function of (A)  $\alpha$  and (B)  $Ra_{uni}$  for  $Re = 1$  (solid lines) and  $Re = 10$  (dashed lines), and  $Ra_p = 1000$ ,  $Pr = 0.71$ . The shaded area identifies conditions where the driving force changes direction and becomes a braking force. .... 40

**Figure 4-14:** Variations of  $\Delta Q/Re$  as a function of (A)  $\alpha$  and (B)  $Ra_{uni}$  for  $Re = 1$  (solid lines) and  $Re = 10$  (dashed lines), and  $Ra_p = 1000$ ,  $Pr = 0.71$ . .... 40



**Figure 4-15:** Variations of (A)  $\Delta F/Re$  and (B)  $\Delta Q/Re$  as functions of  $Pr$  at  $Re = 1$  (solid lines) and  $Re = 10$  (dashed lines) for  $Ra_p = 1000$ ,  $Ra_{uni} = 0$ . ..... 41

**Figure 4-16:** Variations of (A)  $\Delta F/Re$  and (B)  $\Delta Q/Re$  as functions of  $\alpha$  at  $Re = 1$  (solid lines) and  $Re = 10$  (dashed lines) for  $Ra_p = 1000$ ,  $Ra_{uni} = 0$ . ..... 41

**Figure 4-17:** Variations of  $Nu_{av}$  in (A) as a function of  $\alpha$  for  $Re = 1$  (solid lines) and  $Re = 10$  (dashed lines), in (B) as a function of  $Re$  for  $\alpha = 1$  (dashed lines) and  $\alpha = 2$  (solid lines), and in (C) as a function of  $Ra_p$  for  $Re = 1$  (solid lines) and  $Re = 10$  (dashed lines), for  $Pr = 0.71$ ,  $Ra_{uni} = 0$ . Thin dotted lines identify asymptotes. .... 43

**Figure 4-18:** Variations of  $Nu_{av}$  as a function of (A)  $\alpha$  and (B)  $Ra_{uni}$  for  $Re = 1$  (solid lines) and  $Re = 10$  (dashed lines) for  $Ra_p = 1000$ ,  $Pr = 0.71$ . ..... 43

**Figure 4-19:** Variations of  $Nu_{av}$  in (A) as a function of  $\alpha$  and in (B) as a function of  $Pr$  for  $Re = 1$  (solid lines) and  $Re = 10$  (dashed lines) for  $Ra_p = 1000$ ,  $Ra_{uni} = 0$ . ..... 44

**Figure 4-20:** The flow and temperature fields for the same conditions as in Fig.4-7A but with the upper plate heated and the lower plate moving. Thick solid lines identify streamlines, thin solid lines identify negative isotherms while thin dashed lines identify positive isotherms. Thick streamlines mark borders of bubbles trapping the fluid. .... 45

**Figure 5-1:** Schematic diagram of the flow system. .... 48

**Figure 5-2:** Examples of typical flow fields for sinusoidal grooves at the lower plate and smooth upper plate for  $Re = 100$ ,  $y_b = 0.05$ . From left to right  $\alpha = 0.1, 1, 5$ . ..... 49

**Figure 5-3:** Variations of the difference  $\Delta\tau_U/Re$  between the shear stresses acting on the upper smooth plate with the sinusoidal grooves at the lower plate for  $\alpha = 1$ ,  $Re = 1$  (solid lines) and  $Re = 100$  (dashed lines). The mean values  $\Delta\tau_{U,mean}$  are marked using thin lines. .... 50

**Figure 5-4:** Variations of (A)  $\Delta F/F_0$  and (B)  $\Delta Q/Q_0$  as functions of  $\alpha$  for  $Re = 1$  (solid lines) and 100 (dash-dotted lines). Dotted lines identify asymptotes for  $\alpha \rightarrow 0$ . The upper plate is smooth while the lower plate has sinusoidal grooves. .... 51

**Figure 5-5:** Variations of (A)  $\Delta F/F_0$  and (B)  $\Delta Q/Q_0$  as functions of  $y_b$  for  $Re = 1$  (solid lines) and 100 (dash-dotted lines). Thin dotted lines identify asymptotes and the upper bounds. The upper plate is smooth while the lower plate has sinusoidal grooves. .... 52

**Figure 5-6:** Variations of (A)  $\Delta F$  and (B)  $\Delta Q$  as functions of  $Re$  for  $\alpha = 0.1$  (dashed lines),  $\alpha = 1$  (solid lines), and  $\alpha = 5$  (dashed-dotted lines). The upper plate is smooth while the lower plate has sinusoidal grooves. .... 52

**Figure 5-7:** Geometry of grooves used in the present study. .... 53

**Figure 5-8:** Variations of  $\Delta F/Re$  as a function of the number of Fourier modes used for geometry representation for  $Re = 1, y_b = 0.05, \alpha = 1$ . .... 53

**Figure 5-9:** Variations of the force increase  $\Delta F$  for different grooves as functions of (A)  $y_b$  for  $Re = 1, \alpha = 1$ , (B)  $\alpha$  for  $y_b = 0.025, Re = 1$ , (C)  $Re$  for  $y_b = 0.025, \alpha = 1$ . .... 55

**Figure 5-10:** Variations of the error  $Er$  associated with using the first mode of the Fourier expansion representing each groove shape as a function of (A)  $y_b$  for  $Re = 1, \alpha = 1$ , (B)  $\alpha$  for  $y_b = 0.025, Re = 1$ , and (C)  $Re$  for  $y_b = 0.025, \alpha = 1$ . .... 56

**Figure 6-1:** Schematic diagram of the flow system. .... 58

**Figure 6-2:** Evolution of the flow fields as a function of  $\Omega$  for  $y_b = 0.05, \alpha = 1, Ra_p = 1000, Re = 1$ . Figures (A-H) display results for  $\Omega = 0, \pi/4, \pi/2, 3\pi/4, \pi, 5\pi/4, 3\pi/2, 7\pi/4$ , respectively. Black solid lines identify streamlines associated with the buoyancy-driven rolls while black dashed lines identify streamlines associated with the net flow in the horizontal direction. Grey solid and dashed lines identify the positive and negative isotherms. The lower plate temperature distribution is shown below each figure. Enlargements of boxes marked using dotted lines in Figures (F-H) are shown in Figure 6-3. .... 60

**Figure 6-3:** Enlargements of the flow fields near the upper plate for (A)  $\Omega = 5\pi/4$ , (B)  $\Omega = 3\pi/2$ , and (C)  $\Omega = 7\pi/4$ . The remaining flow conditions are given in Figure 6-2. .... 61

**Figure 6-4:** Evolution of the flow field as a function of  $\Omega$  for  $y_b = 0.05, \alpha = 1, Ra_p = 1000, Re = 1$ . Figures (A-C) display results for  $\Omega = 0, \pi/2, 3\pi/2$ , respectively. Solid lines identify

streamlines, and dashed and dashed-dotted lines identify the positive and negative isobars. Arrows at the lower plate illustrate pressure forces..... 63

**Figure 6-5:** Distribution of (A) the  $x$ -component  $\sigma_{xp,L}$ , and (B) the  $y$ -component  $\sigma_{yp,L}$  of the pressure force at the lower plate for  $y_b = 0.05$ ,  $Re = 1$ ,  $\alpha = 1$ ,  $Ra_p = 1000$ , and  $\Omega = 0, \pi/2, 3\pi/2$ . The dashed-dotted line illustrates the no heating conditions. The thick line below each figure illustrates the groove shape, and dashed and dotted lines illustrate plate temperatures for  $\Omega = \pi/2, 3\pi/2$ , respectively..... 63

**Figure 6-6:** Shear stress distributions at the upper plate ( $\tau_U$ ) for  $y_b = 0.05$ ,  $Re = 1$ ,  $\alpha = 1$ ,  $Ra_p = 1000$  and  $\Omega = 0, \pi/2, 3\pi/2$ . The thick line below the figure illustrates the shape of the groove, and dashed and dotted lines illustrate plate temperatures for  $\Omega = \pi/2, 3\pi/2$ , respectively. The mean values of shear are marked using horizontal lines..... 64

**Figure 6-7:** Variations of (A)  $\Delta F/Re$  and (B)  $\Delta Q/Re$  as functions of the phase difference  $\Omega$  for  $Ra_p = 1000$ ,  $Re = 1$ ,  $\alpha = 1$  and different groove amplitudes. Dashed lines identify results for the smooth lower plate. The light gray shaded area (zone I) identifies conditions requiring the use of braking force. The white area (zone II) identifies conditions resulting in a reduction of the driving force. The dark gray shaded area (zone III) identifies conditions requiring an increase of the driving force..... 65

**Figure 6-8:** Variations of  $\Delta F/Re$  as a function of  $\alpha$  for  $y_b = 0.01$ ,  $Ra_p = 1000$  and  $Re = 1, 5$  (solid and dashed lines, respectively). Dotted lines illustrate conditions for the smooth lower plate. The light gray shaded area (zone I) identifies conditions requiring the use of braking force. The white area (zone II) identifies conditions resulting in a reduction of the driving force. The dark gray shaded area (zone III) identifies conditions requiring an increase of the driving force. 66

**Figure 6-9:** Variations of  $\Delta Q/Re$  as a function of  $\alpha$  for  $y_b = 0.01$ ,  $Ra_p = 1000$  and  $Re = 1, 5$  (solid and dashed lines, respectively). Dotted lines illustrate conditions for the smooth lower plate..... 66

**Figure 6-10:** Variations of the flow and temperature field for  $\Omega = \pi/2$ ,  $Ra_p = 1000$ ,  $y_b = 1$ ,  $Re = 1$  for (A)  $\alpha = 1$ , (B)  $\alpha = 2$ , (C)  $\alpha = 5$ , (D)  $\alpha = 8$ . Thin dashed and solid lines illustrate the positive and negative isotherms, respectively..... 67

**Figure 6-11:** Variations of  $\Delta F$  as a function of  $Re$  for  $y_b = 0.01$ ,  $Ra_p = 1000$  and  $\alpha = 2, 3$  (solid and dashed lines, respectively). Dotted lines illustrate results for the smooth lower plate. The light gray shaded area (zone I) identifies conditions requiring the use of braking force. The white area (zone II) identifies conditions resulting in a reduction of the driving force. The dark gray shaded area (zone III) identifies conditions requiring an increase of the driving force. 68

**Figure 6-12:** Variations of  $\Delta Q$  as a function of  $Re$  for  $y_b = 0.01$ ,  $Ra_p = 1000$  and  $\alpha = 2, 3$  (solid and dashed lines, respectively). Dotted lines illustrate results for the smooth lower plate. ... 68

**Figure 6-13:** Variations of the flow and temperature fields for  $\Omega = \pi/2$ ,  $Ra_p = 1000$ ,  $y_b = 1$ ,  $\alpha = 2$  for (A)  $Re = 1$ , (B)  $Re = 5$ , (C)  $Re = 10$ , (D)  $Re = 50$ . Thin dashed and solid lines illustrate the positive and negative isotherms. .... 69

**Figure 6-14:** Variations of  $\Delta F/Re$  as a function of  $y_b$  for  $Ra_p = 1000$ ,  $\alpha = 2$ ,  $Re = 1, 5$  (solid and dashed lines, respectively). Dotted lines illustrate the solution for the smooth plate. The light gray shaded area (zone I) identifies conditions requiring the use of braking force. The white area (zone II) identifies conditions resulting in a reduction of the driving force. The dark gray shaded area (zone III) identifies conditions requiring an increase of the driving force. .... 70

**Figure 6-15:** Variations of  $\Delta Q/Re$  as a function of  $y_b$  for  $Ra_p = 1000$ ,  $\alpha = 2$  and  $Re = 1, 5$  (solid and dashed lines, respectively). Dotted lines illustrate solutions for the smooth lower plate. 70

**Figure 6-16:** Variations of the flow and pressure fields for  $\Omega = \pi/2$ ,  $Ra_p = 1000$ ,  $\alpha = 1$ ,  $Re = 1$  for (A)  $y_b = 0.001$ , (B)  $y_b = 0.025$ , and (C)  $y_b = 0.05$ . Thin dashed and solid lines illustrate the positive and negative isobars. .... 71

**Figure 6-17:** Variations of the  $x$ -component of the induced pressure force for the flow fields shown in Figure 6-16(A-C)..... 71

**Figure 6-18:** Variations of  $\Delta F/Re$  as a function of  $Ra_p$  for  $y_b = 0.01$ ,  $\alpha = 2$  and  $Re = 1, 5$  (solid and dashed lines, respectively). Dotted lines illustrate results for the smooth lower plate. Figure (A) displays results in the log-log scale while Fig. (B) uses the semi-log scale. The light gray shaded area (zone I) identifies conditions requiring the use of braking force. The white area (zone II) identifies conditions resulting in a reduction of the driving force. The dark gray shaded area (zone III) identifies conditions requiring an increase of the driving force. .... 72

**Figure 6-19:** Variations of  $\Delta Q/Re$  as a function of  $Ra_p$  for  $y_b = 0.01$ ,  $\alpha = 1$  and  $Re = 1, 5$  (solid and dashed lines, respectively). Dotted lines identify results for the smooth lower plate. Grey lines identify negative values. Figure (A) displays results in the log-log scale while Fig. (B) uses the semi-log scale. .... 73

**Figure 6-20:** Variations of the flow and temperature fields for  $\Omega = \pi/2$ ,  $y_b = 1000$ ,  $\alpha = 1$ ,  $Re = 1$  for (A)  $Ra_p = 100$ , (B)  $Ra_p = 500$ , (C)  $Ra_p = 1000$ , (D)  $Ra_p = 2000$ . Thin dashed and solid lines identify the positive and negative isotherms. .... 73

**Figure 6-21:** Variations of  $\Delta F/Re$  for  $Ra_p = 1000$ ,  $y_b = 0.01$  as a function of (A)  $Ra_{uni}$  for  $\alpha = 1$  and (B)  $\alpha$  for  $Re = 1$ . In (A), solid and dashed lines correspond to  $Re = 1, 5$ , respectively. In (B), dashed, solid and dashed-dotted lines correspond to  $Ra_{uni} = -150, 0, 150$ , respectively. Dotted lines identify results for the smooth lower plate. The light gray shaded area (zone I) identifies conditions requiring the use of braking force. The white area (zone II) identifies conditions resulting in a reduction of the driving force. The dark gray shaded area (zone III) identifies conditions requiring an increase of the driving force. .... 74

**Figure 6-22:** Variations of  $\Delta Q/Re$  for  $Ra_p = 1000$ ,  $y_b = 0.01$  as a function of (A)  $Ra_{uni}$  for  $\alpha = 1$  and (B)  $\alpha$  for  $Re = 1$ . In (A), solid and dashed lines correspond to  $Re = 1, 5$ , respectively. In (B), dashed, solid and dashed-dotted lines correspond to  $Ra_{uni} = -150, 0, 150$ , respectively. Dotted lines identify results for the smooth lower plate. .... 75

**Figure 6-23:** Variations of  $\Delta F/Re$  as a function of  $Pr$  for  $y_b = 0.01$ ,  $Ra_p = 1000$ ,  $\alpha = 2$  at  $Re = 1, 5$  (solid and dashed lines, respectively). Figure (A) displays results in the log-log scale while Fig. (B) uses the semi-log scale. In (A), dashed-dotted lines identify negative values. Dotted lines are used to identify results for the smooth lower plate at  $Re = 1$ . The light gray shaded area (zone I) identifies conditions requiring the use of braking force. The white area (zone II) identifies conditions resulting in a reduction of the driving force. The dark gray shaded area (zone III) identifies conditions requiring an increase of the driving force. .... 76

**Figure 6-24:** Variations of  $\Delta Q/Re$  as a function of  $Pr$  for  $y_b = 0.01$ ,  $Ra_p = 1000$ ,  $\alpha = 2$  at  $Re = 1, 5$  (solid and dashed lines, respectively). Fig. (A) displays results in the log-log scale while Fig. (B) uses the semi-log scale. In (A), dashed-dotted lines identify negative values. Dotted lines are used to identify results for the smooth lower plate at  $Re = 1$ . .... 76

**Figure 6-25:** Variations of (A)  $\Delta F/Re$ , and (B)  $\Delta Q/Re$  as function of  $\alpha$  for  $y_b = 0.01$ ,  $Ra_p = 1000$ ,  $Re = 1$  and  $Pr = 0.71, 1, 5$  (solid, dashed-dotted and dashed lines, respectively). Dotted lines identify conditions for the smooth lower plate. The light gray shaded area (zone I) identifies conditions requiring use of braking force. The white area (zone II) identifies conditions resulting in a reduction of the driving force. The dark gray shaded area (zone III) identifies conditions requiring an increase of the driving force. .... 77

**Figure 6-26:** Variations of  $Nu_{av}$  as a function of (A)  $\Omega$  and (B)  $\alpha$ . In (A),  $Ra_p = 1000$ ,  $\alpha = 1$ ,  $Re = 1$ . In (B),  $Ra_p = 1000$ ,  $y_b = 0.01$ ,  $Re = 1, 5$  (solid and dashed lines, respectively). Dotted lines illustrate conditions for the smooth lower plate..... 78

**Figure 6-27:** Variations of  $Nu_{av}$  as a function of (A)  $Re$ , (B)  $Ra_p$ , (C)  $y_b$ . In (A),  $Ra_p = 1000$ ,  $\alpha = 2$  (solid lines) and  $\alpha = 3$  (dashed lines),  $y_b = 0.01$ . In (B),  $y_b = 0.01$ ,  $\alpha = 2$ ,  $Re = 1$  (solid lines) and  $Re = 5$  (dashed lines). In (C),  $Ra_p = 1000$ ,  $\alpha = 2$ ,  $Re = 1$  (solid lines) and  $Re = 5$  (dashed lines). Thin dotted lines identify asymptotes. .... 78

**Figure 6-28:** Variations of  $Nu_{av}$  as a function of (A)  $Ra_{uni}$ , and (B)  $\alpha$ . In (A),  $y_b = 0.01$ ,  $Ra_p = 1000$ ,  $\alpha = 2$ ,  $Re = 1$  (solid lines) and  $Re = 5$  (dashed lines). In (B),  $y_b = 0.01$ ,  $Ra_p = 1000$ ,  $Re = 1$ ,  $Ra_{uni} = -150$  (dashed lines),  $Ra_{uni} = 0$  (solid lines), and  $Ra_{uni} = 150$  (dashed-dotted lines). Dotted lines illustrate results for the smooth lower plate. .... 79

**Figure 6-29:** Variations of  $Nu_{av}$  as a function of (A)  $Pr$ , and (B)  $\alpha$ . In (A),  $y_b = 0.01$ ,  $Ra_p = 1000$ ,  $\alpha = 2$ ,  $Re = 1$  (solid lines) and  $Re = 5$  (dashed lines). In (B),  $y_b = 0.01$ ,  $Ra_p = 1000$ ,  $Re = 1$ ,  $Pr = 0.71$  (solid lines),  $Pr = 1$  (dashed-dotted lines), and  $Pr = 5$  (dashed lines). Dotted lines illustrate results for the smooth lower plate. .... 80

## **List of Appendices**

Appendix A: Recurrence formulae and Chebyshev inner products.....	94
Appendix B: Evaluation of viscous and pressure forces at the lower plate.....	96

# List of Abbreviations and Nomenclature

## Abbreviations

RB	Rayleigh – Bénard
IBC	Immersed Boundary Conditions
RF	Relaxation Factor

## Nomenclature

### Chapter 1

$Ra$	Rayleigh number $\left( = \frac{g\Gamma h^3 \Delta T}{\kappa \nu} \right)$
$Ra_{cr}$	Critical Rayleigh number for the onset of the Rayleigh – Bénard instability
$Re$	Reynolds number $\left( = \frac{\rho U h}{\mu} \right)$

### Chapter 2

*	Superscript denoting dimensional quantities
0	Subscript denoting reference case
$c$	Specific heat
$F$	Driving force
$g$	Gravitational acceleration
$h$	Half of the average channel height



$k$	Thermal conductivity
$L$	Subscript denoting lower plate
<i>mean</i>	Subscript denoting mean value
$Nu$	Nusselt number $\left( = \frac{hL}{k} \right)$
$p$	Subscript denoting periodic value
$p$	Pressure
$Pr$	Prandtl number $\left( = \frac{\nu}{\kappa} \right)$
$Q$	Flow rate
$T$	Temperature
$U$	Subscript denoting upper plate
$(u, v)$	Velocity component in the $(x, y)$ direction
<i>uni</i>	Subscript denoting uniform value
$(x, y)$	Physical coordinate system
$y_b$	Amplitude of the groove at the lower plate
$y_U, y_L$	Shapes of the upper and lower plates in the physical coordinate system
$\alpha$	Wavenumber
$\Gamma$	Thermal expansion coefficient
$\theta$	Relative temperature
$\kappa$	Thermal diffusivity

$\lambda$	Wavelength
$\mu$	Dynamic viscosity
$\nu$	Kinematic viscosity
$\rho$	Density
$\tau$	Shear stress
$\Omega$	Phase difference

### Chapter 3

*	Superscript denoting complex conjugates
$\langle n \rangle$	Superscript denoting Fourier mode
$A$	Mean pressure gradient
$A_L^{(n)}$	Coefficients of Fourier expansions describing the geometry
D	Derivation with respect to transverse direction
$\widehat{D}L_k^{(m)}$	Coefficients of the Fourier expansions for the first derivative of the Chebyshev polynomials evaluated at the lower plate
$\widehat{G\varphi}_k$	Chebyshev coefficients in the expansion representing $\varphi^{(n)}$
$\widehat{Gu}_k^{(n)}, \widehat{Guv}_k^{(n)}, \widehat{Gvv}_k^{(n)}, \widehat{G\theta}_k^{(n)}, \widehat{Gv\theta}_k^{(n)}$	Coefficients of the Chebyshev expansions of the modal functions in the Fourier expansions

	representing velocity and temperature products
$\widehat{G\phi}_k$	Chebyshev coefficients in the expansion representing $\phi^{(n)}$
$i$	Imaginary part
$l$	Iteration number
$N_M$	Number of Fourier modes used for discretization in the $x$ – direction
$N_S$	Number of Fourier modes used to describe the Chebyshev polynomials and their derivatives evaluated at the upper and lower plates
$N_T$	Number of Chebyshev polynomials used for discretization of the modal function in the $\hat{y}$ -direction
$N_{VV}, N_{V\theta}$	Nonlinear terms
$N_x$	Number of grid points along the $x$ - direction in $(x, \hat{y})$ plane
$T_k$	$k$ -th Chebyshev polynomial of the first kind
$\widehat{uu}, \widehat{uv}, \widehat{vv}, \widehat{u\theta}, \widehat{v\theta}$	Velocity and temperature products in the physical space
$\widehat{uu}^{(n)}, \widehat{uv}^{(n)}, \widehat{vv}^{(n)}, \widehat{u\theta}^{(n)}, \widehat{v\theta}^{(n)}$	Modal functions of the velocity and temperature products $\widehat{uu}, \widehat{uv}, \widehat{vv}, \widehat{u\theta}, \widehat{v\theta}$
$\widehat{WL}_k^{(m)}$	Coefficient of Fourier expansion for the Chebyshev polynomials evaluated at the lower plate

$(x, \hat{y})$	Coordinate system in the computational domain
$\Gamma$	Constant associated with the transformation for the IBC method
$\phi^{(n)}$	Modal functions in the Fourier expansion representing the temperature
$\varphi^{(n)}$	Modal functions in the Fourier expansion representing the stream function
$\psi$	Stream function
$\omega$	Weight function

## Chapter 1

### 1 Introduction

In simple shear-driven flows, the relative movement between two parallel plates drives the fluid flow. These flows are characterized by the absence of a streamwise pressure gradient. An external force is required to maintain the relative plate movement. There is an interest in the reduction of this external force as this would lead to the reduction of the energy expenditure associated with operations of such systems. This reduction of the driving force is analogous to the drag reduction in other systems. Common techniques of drag reduction include injection of dilute polymers (Bonn, *et al.*, 2005), introduction of plate oscillations (Hurst, *et al.*, 2014), use of suction/blowing (Segawa, *et al.*, 2007; Virk, 1975), use of various actuators (Mahfoze & Laizet, 2017), use of heating patterns (Hossain & Floryan, 2016), and changing the plate topography (Mohammadi & Floryan, 2013b), to name a few. Some of these approaches can be characterized as focused on the laminar flow control so that transitions to secondary states are avoided. Others, like the one which is followed in this thesis, are focused on the creation of spatial flow modulations which would lead to the reduction of shear and, thus, reduction of the frictional resistance.

#### 1.1 Objective

The main objective of this thesis is to understand the system responses in the case of shear-driven flows when one of the bounding plates is exposed to spatial heating and surface irregularities. Changes of the flow-driving force in response to such irregularities are to be identified through a systematic analysis of each of these effects. A proper understanding of these effects will enhance the existing knowledge of the flow control techniques and contribute to the improvement of the flow system performance.

## 1.2 Motivation

Shear-driven flows have been of interest since the works of Couette in the early nineteenth century. Since then, this class of flows has been widely used in industry. Applications include processes like coating (Weinstein & Ruschak, 2004) (see Figure 1-1A), fluid movement in bearings and between shafts (see Figure 1-1B), fluid sealing systems, lubrication problems, towing of free-floating bodies in shallow basins, etc. Further applications can be identified in Micro-Electro-Mechanical-Systems (Ho & Tai, 1998) and in chemical processes (Desmet & Baron, 2000).

The boundary and temperature irregularities frequently occur in nature, e.g. air circulation in the atmospheric boundary layer and heat island effect, mixing in oceans, shark skins which allow them to move with a particular ease, compact heat exchangers, microfluidic and nanofluidic devices, cell analyzers, and many others.

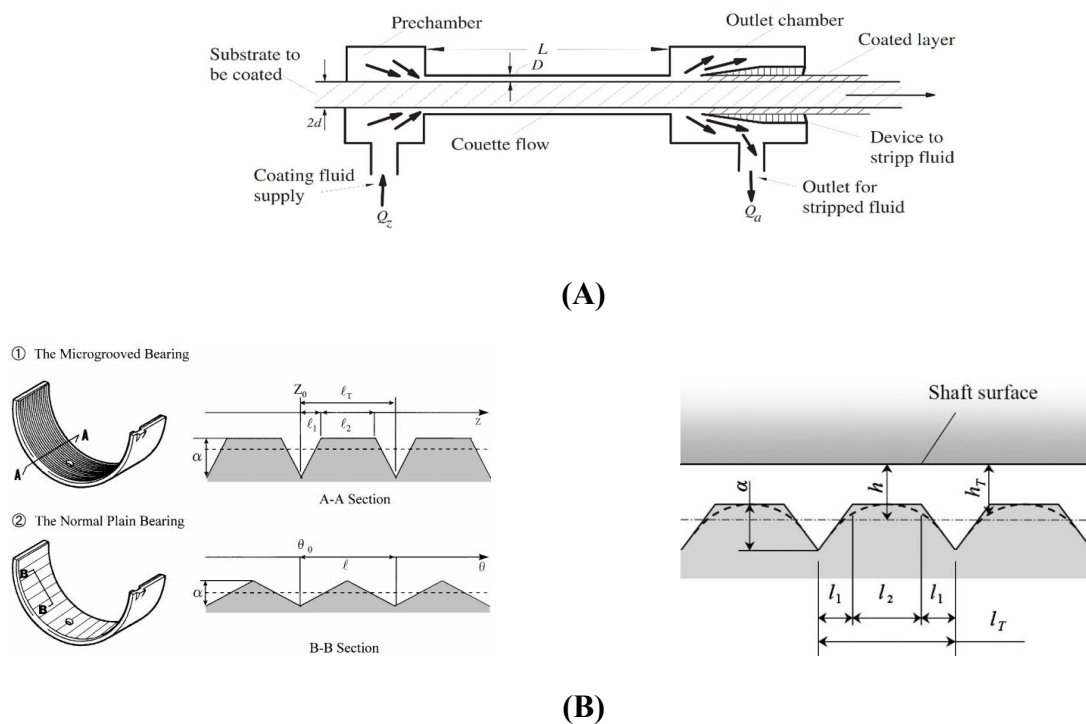


**Figure 1-1:** Applications of shear-driven flow in (A) Coating processes (Figure from (Durst, 2008)), (B) fluid movement in bearings (Figure from (Ashihara & Hashimoto, 2010)).

Most of the existing studies dealing with surface and temperature irregularities are focused on the pressure-driven flows. Therefore, there exists a void in knowledge regarding flow responses due to surface irregularities and heating patterns in shear-driven flows. Given their frequent use in industries, the development of techniques to control the costs required to maintain such flows provides the main motivation for this study.

### 1.3 Related literature survey

There exists a considerable number of analyses dealing with the effects of surface irregularities, but they are mostly focused on the pressure-driven flows. Likewise, the existing literature dealing with the effects of heating is mostly focused on the convective heat transfer. Therefore, the discussion of the literature is divided into several categories, with each of them focused on a specific issue of interest in this analysis.

#### 1.3.1 Effects of surface irregularities

##### 1.3.1.1 Pressure-driven flows

The effect of geometric irregularity (surface roughness) in pressure-driven flows is a classical yet not fully understood concept in fluid mechanics. The history of studying the effects of surface roughness dates back to the works of Darcy (1857) and Hagen (1854), who concluded that roughness always increases the overall flow resistance. Moody (1944) and Nikuradse (1933), with the limited instrumentation available at that time, carried out extensive experiments and proposed the concept of friction factor for drag quantification. They also concluded that the drag in laminar flow is independent of surface roughness or, at least, roughness effects were too small to be determined using the existing measuring techniques. These correlations suggest that surface roughness has a significant effect on the turbulent flow and always increases the turbulent drag.

The prevailing conclusion that surface roughness always increases the flow resistance was first challenged by Walsh (1980, 1983), who showed that certain surface topographies can

reduce the drag below what is found for smooth plates. These special surface shapes were referred to as riblets, i.e. short wavelength streamwise grooves. Effects of riblets on drag reduction were further studied experimentally by Walsh & Lindemann (1984), Bruse, *et al.* (1993), Bechert, *et al.* (1997), and numerically by Choi, *et al.* (1991), Chu & Karniadakis (1993), Chu, *et al.* (1992), Goldstein & Tuan (1998), Goldstein, *et al.* (1995), and in all of these cases it was concluded that riblets were capable of reducing turbulent drag but no clear conclusion was reached about the laminar drag.

Pressure losses for laminar flows over geometric irregularities gained interest due to the occurrence of such flows in micro and nano-channels, and due to deviation from the classical theories based on the works of Gamrat *et al.* (2008), Papautsky *et al.* (1999), Sharp & Adrian (2004), and Sobhan & Garimella (2001). Mohammadi & Floryan (2013b) investigated pressure loss in grooved channels for laminar flows and found potential to obtain drag reduction by the proper shaping of grooves. Mohammadi (2013), Mohammadi & Floryan (2013a), Moradi (2014), and Moradi & Floryan (2013) investigated longitudinal grooves and quantified their drag reducing abilities.

Mohammadi & Floryan (2012) categorized the mechanisms responsible for the generation of drag into three types, namely associated with the pressure form drag, the pressure interaction drag, and the shear drag. The shear drag is associated with surface-groove-induced changes in the wall shear, as well as with an increase of the wetted area. The pressure form drag is associated with the mean pressure gradient driving the flow and the pressure interaction drag is generated through an interaction between the groove-modulated part of the pressure field and the surface geometry. The importance of pressure effects increases rapidly with the groove amplitude. Information about the types of drag and their dependence on the groove shape offers potential for identification of surface topographies that may result in a lower drag.

Use of the superhydrophobic effect is also useful in reducing drag. In this case, the surface topography traps gas bubbles in micro-pores, replacing the shear stress between liquid and solid with a shear stress between liquid and gas (Rothstein, 2010). Existence of the laminar drag reduction using micro-pores has been verified by Joseph, *et al.* (2006), Ou, *et al.*



(2004), Ou & Rothstein (2005) and Truesdell, *et al.* (2006). The effectiveness of this method was optimized by correctly shaping the surface pores (Samaha, *et al.*, 2011) and by changing the hydrophobicity using changes in the surface chemistry (Quere, 2008; Reyssat, *et al.*, 2008; Zhou, *et al.*, 2011). The stability characteristics in such flows are not yet fully understood.

### 1.3.1.2 Shear-driven flows

The plane-Couette flow represents the simplest shear-driven flow. It occurs between two parallel plates in relative motion. It is characterized by the lack of a streamwise pressure gradient as the flow is driven by plate movement only. The flow has linear velocity distribution and constant shear throughout the flow field. It is also linearly stable (Romanov, 1972). The transition to secondary states has been studied in detail by Deguchi & Nagata (2011) who identified various routes to secondary finite-amplitude states as well as to turbulence.

The experiments on transition between the laminar and turbulent states and the role of roughness in Couette flow are described in Aydin & Leutheusser (1991). The form of the flow is predicted analytically for long wavelength grooves in Malevich, *et al.* (2008). The potential slip at the rough surface is discussed in Niavrani & Priezjev (2009), and Priezjev & Troian (2006). While it is known that Couette flow is linearly stable (Romanov, 1972), it becomes unstable in the presence of grooves resulting in the formation of streamwise vortices (Floryan, 2002). Similar secondary flows may appear due to the introduction of wall transpiration (Floryan, 2003). Shear instability modes are generated in the annular Couette flow (Moradi & Floryan, 2013). Various simplified models have been used to study effects of varying groove geometry (Sahlin, *et al.*, 2005; Valdés, *et al.*, 2012; Wang, *et al.*, 2014). All of these studies and a concluding remark in Mohammadi & Floryan (2014) suggest that introducing surface roughness always increases the flow resistance in shear-driven flows.

### 1.3.2 Effects of heating irregularities

A recently introduced technique for drag reduction uses spatial heating patterns (Hossain & Floryan, 2016) that create a buoyancy field which leads to the formation of a system of separation bubbles. Fluid trapped inside these bubbles rotates due to the action of horizontal density gradients and as a result, a propulsive force is created which contributes to fluid pumping. In addition, these bubbles isolate the stream from direct contact with the plate and thus reduce the frictional drag. This phenomenon is referred to as the super-thermo-hydrophobic effect (Floryan, 2012). This effect is enhanced by combining distributed and uniform heating of the lower plate (Floryan & Floryan, 2015). Similar results can also be achieved by heating the upper plate (Hossain & Floryan, 2014). One drawback of this technique lies in the fact that the flow has to be fairly slow as stronger flows wash away separation bubbles (Hossain, 2011; Hossain, *et al.*, 2012; Hossain & Floryan, 2015). This limitation leads to the search for ways of enhancing this effect so that it can be applied at higher Reynolds numbers. Yamamoto, *et al.* (2013) demonstrated simultaneous drag reduction and heat transfer enhancement using suction/blowing waves travelling in the downstream direction. Their results provide motivation for exploring these methods in conjunction with the heating non-uniformities. However, when both plates were heated, drag reduction strongly depended on the phase difference between the lower and upper heating. The drag reduction could increase by up to three times over that found in the case of one plate heating if the proper phase difference was used. The range of Reynolds numbers with effective drag reduction was doubled at the same time (Hossain & Floryan, 2016).

Heating non-uniformities represent a wider class of problems which have been studied on a case by case basis and not necessarily in the context of drag reduction. The non-uniformities create horizontal and vertical temperature gradients which result in the horizontal density variations that create motions referred to as horizontal convection. Maxworthy (1997) reviewed the numerical and experimental analyses focused on convection in regions with either open or partially-open lateral boundaries. Siggers, *et al.* (2004) showed numerically that the horizontal convection can be unsteady and turbulent, capable of maintaining overturning circulation within a layer heated and cooled

differentially at its surface with a general temperature distribution imposed at the top of the layer and a variety of thermal boundary conditions at the base of the layer. Hughes & Griffiths (2008) used horizontal convection as an idealized model of the ocean overturning circulation with the non-uniform heating profiles imposed at a horizontal boundary and demonstrated that convection depends on the geometry of the flow system and on the externally imposed thermal conditions.

The analyses of fundamental aspects of convection have been focused on simple reference cases as many variables affect the system response. Consider the simplest case of a horizontal slot subject to a spatially homogeneous heating applied at the lower plate, also known as the Rayleigh-Bénard (RB) convection (Bénard, 1900; Rayleigh, 1916). This convection results from the transition from a conductive state when the critical conditions are exceeded and it changes the character of the heat flow in qualitative terms (Ahlers, *et al.*, 2009; Bodenschatz, *et al.*, 2000; Chilla & Schumacher, 2012; Lohse & Xia, 2010). These critical conditions are expressed in terms of the critical Rayleigh number  $Ra_{cr}$  with secondary flow occurring for  $Ra > Ra_{cr}$ . A large enough heating intensity leads to turbulent RB convection (Ahlers *et al.*, 2009; Lohse & Xia, 2010). Convection onset conditions are affected by the heating non-uniformities (Freund, *et al.*, 2011) as well as geometric non-uniformities (McCoy, *et al.*, 2008; Seiden, *et al.*, 2008; Weiss, *et al.*, 2012). Results dealing with the effects of geometry modulation on the RB convection are very limited but demonstrate that the non-uniformities do play a role. Two-dimensional convection rolls have been observed for subcritical conditions ( $Ra \ll Ra_{cr}$ ) in the case of the lower plate being augmented with thin stripes. The amplitude of these rolls grew with  $Ra$  until they were destabilized with mechanisms which depended on the ratio of the wavenumber of the imposed modulation and the critical wavenumber of the RB convection producing a variety of three-dimensional patterns.

There exist several studies focused on the applied aspects of convection and involving specialized geometries. Bergeles (2001) showed that for single phase flows in tubes, up to a 400% increase in the nominal heat transfer coefficient can be achieved by adjusting surface topography. Siddique, *et al.* (2011) reviewed different heat transfer enhancing techniques which included the use of extended surfaces including fins and micro-fins,

porous media, suspensions of large particles, suspensions of small particle (nanofluids), phase-change devices, flexible seals, vortex generators, protrusions, composite materials with ultra-high thermal conductivity, etc. Ligrani, *et al.* (2003) suggested that all these techniques can either create secondary flows and/or can increase the turbulence level resulting in an increase of fluid mixing. Dewan, *et al.* (2004) reviewed the passive heat transfer augmentation techniques based on the use of twisted tapes and wire coils. There exists a lack of fundamental and systematic research on the effects of surface roughness/grooves on natural and mixed convection, and on the onset of secondary states in buoyancy-driven motions. This becomes more eminent in micro-channels where the roughness size cannot be reduced to a negligible level using the currently available manufacturing techniques. Sobhan & Garimella (2001) reviewed different studies on the flow and heat transfer in micro-channels with surface roughness and concluded that there is a need for additional systematic studies to examine the effects of each of the concerned parameters separately. Xia *et al.* (2011) studied the fluid flow and heat transfer mechanisms in micro-channels and concluded that change in surface area and complexities in the boundary layer were primarily responsible for change in heat transfer characteristics with a change in the pressure drop.

Recently, Toppaladoddi *et al.* (2015) studied geometric optimization for heat transportation. Goluskin & Doering (2016) studied the effects of geometric parameters on turbulent convection. A systematic study by Abtahi (2017), Abtahi & Floryan (2017), analyzed natural convection in a horizontal slot formed by two grooved plates for subcritical Rayleigh numbers. It was found that the grooves create a horizontal temperature gradient that leads to the formation of the vertical and horizontal pressure gradients which drive the motion for any Rayleigh number. Groove wavelengths dictated the size of the convection rolls for most cases except for short wavelength grooves where the motion was found to be confined to a boundary layer near the grooved plate. The intensity of convection was found to be more intense when grooves were placed on both plates rather than in either of the plates, and the largest intensity was found when grooves of the upper and lower plates were in the same phase (i.e. they formed a wavy slot) and weakest when they were out of phase (i.e. they formed a converging-diverging slot). They also concluded that the shear forces acted in a manner consistent with the groove build up whereas the effect of

pressure forces depended on the groove geometry, location and the heating conditions. The changes in the heat flow were quite complex as they resulted from a combination of conductive changes associated with grooves and convective changes associated with the heating and geometric irregularities.

Abtahi & Floryan (2017*a, b*) analyzed natural convection in a horizontal fluid layer exposed to heating and geometric irregularities. They considered periodic distribution for both heating and geometric irregularities and quantified their relative position using phase difference. They concluded that the interaction of the heating and groove patterns was able to create a net horizontal flow in the absence of any mean pressure gradient. This flow could be directed in any direction depending on the phase difference between the heating and groove patterns.

## 1.4 Outline of the present work

This thesis is organized as follows. Chapter 1 describes the objectives and motivations for the present work and provides a literature review on the related topics. Chapter 2 introduces the model problem which provides the means for analysis of the effects of geometric and heating irregularities. Chapter 3 describes the numerical method used. Chapter 4 describes the effects of spatially periodic heating in the case of smooth plates. Chapter 5 discusses the effects of geometric irregularities when the system is isothermal. Chapter 6 discusses the system response when both the geometric as well as temperature irregularities are present simultaneously. Chapter 7 summarizes the main conclusions and provides suggestions for future work.

## Chapter 2

### 2 Model Problem

This chapter describes the model problem which captures the physical phenomenon of interest in the analysis, i.e. reduction of forces required to support the relative movement of parallel plates. Spatially distributed heating is the method of choice for force reduction. This heating is applied to the stationary plate, which can be grooved, while the moving plate is kept isothermal and smooth. The model problem is two-dimensional as the force reducing method is two-dimensional. It is assumed that the working fluid is Newtonian, and its properties are well described using Boussinesq approximation. Section 2.1 depicts the general geometry to be considered, Section 2.2 describes the external heating pattern to be applied, Section 2.3 provides a concise summary of the governing equations to be used, Sections 2.4 and 2.5 discuss the relevant boundary conditions and the flow constraint. A reference isothermal case is explained in Section 2.6. Evaluation of forces, flow rate and induced heat transfer are discussed in Sections 2.7-2.9.

#### 2.1 Geometry

Consider two horizontal plates moving relative to each other with the gap between them filled with a fluid. The upper plate is smooth while the lower one is assumed to be sinusoidally grooved resulting in the gap geometry of form –

$$y_L^*(x^*) = -h^* + y_b^* \cos(\alpha^* x^*), \quad (2.1a)$$

$$y_U^*(x^*) = h^*. \quad (2.1b)$$

where the subscripts  $L$  and  $U$  refer to the lower and upper plates respectively,  $y_b^*$  is the amplitude of the groove,  $\alpha^*$  is its wavenumber and stars identify dimensional quantities. The gap extends to  $\pm\infty$  in the  $x^*$ -direction, its mean opening is  $2h^*$ , and its periodicity is characterized by the wavelength  $\lambda^* = 2\pi/\alpha^*$ .

Considering the half of the mean gap height  $h^*$  as the length scale, the dimensionless form of the gap geometry becomes

$$y_L(x) = -1 + y_b \cos(\alpha x), \quad (2.2a)$$

$$y_U(x) = 1. \quad (2.2b)$$

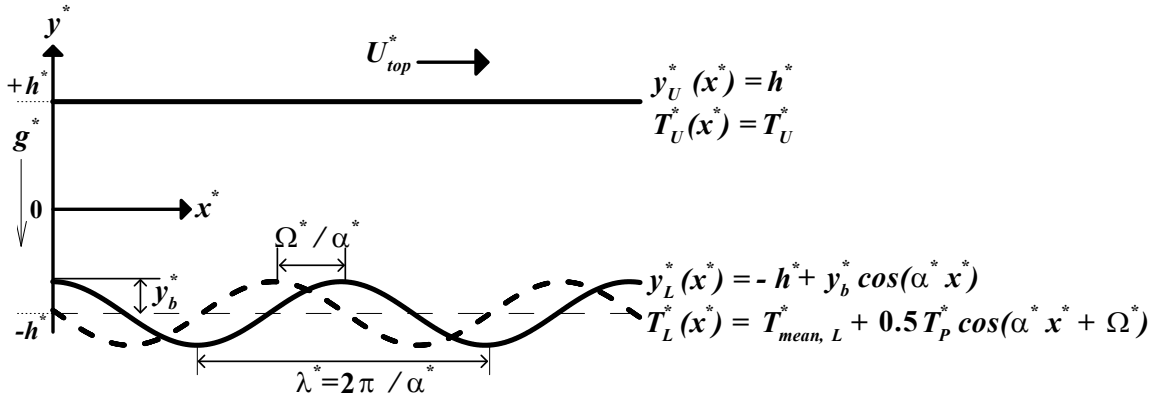


**Figure 2-1:** Schematic diagram of the flow system.

## 2.2 Heating pattern

Introduce an external heating resulting in sinusoidal temperature variations along the lower plate and a constant temperature of the upper plate, i.e.

$$T_L^*(x^*) = T_{mean,L}^* + 0.5 T_p^* \cos(\alpha^* x^* + \Omega^*), \quad (2.3a)$$

$$T_U^*(x^*) = T_U^*, \quad (2.3b)$$

where the subscripts “mean” and “p” refer to the mean and periodic parts, respectively,  $T_p^*$  is the peak-to-peak amplitude of the periodic component, and  $\Omega^*$  is the phase shifts between the heating and groove patterns. Use of the upper plate temperature for reference (all material properties are to be evaluated at this temperature) and introduction of the relative temperature  $\theta^* = T^* - T_U^*$  lead to plates’ temperatures of the form

$$\theta_L^*(x) = \theta_{uni}^* + 0.5 \theta_p^* \cos(\alpha^* x^* + \Omega^*), \quad (2.4a)$$

$$\theta_U^*(x) = 0. \quad (2.4b)$$

where  $\theta_{uni}^* = T_{mean,L}^* - T_U^*$ , and  $\theta_p^* = T_p^*$ .

Considering  $\kappa^* \nu^* / (g^* \Gamma^* h^{*3})$  as the temperature scale results in the following dimensionless expression for the temperatures of the plates

$$\theta_L(x) = Ra_{uni} + 0.5 Ra_p \cos(\alpha x + \Omega), \quad (2.5a)$$

$$\theta_U(x) = 0 \quad (2.5b)$$

where  $Ra_{uni} = g^* \Gamma^* h^{*3} T_{uni}^* / (\kappa^* \nu^*)$  is the uniform Rayleigh number measuring the intensity of the uniform (mean) part of the applied heating and  $Ra_p = g^* \Gamma^* h^{*3} T_p^* / (\kappa^* \nu^*)$  is the periodic Rayleigh number measuring the intensity of the periodic part of the applied heating.

## 2.3 Governing equations

Assume that the upper plate is pulled in the positive  $x^*$ -direction with a constant velocity  $U_{top}^*$  while the lower plate is stationary. The fluid is assumed to have thermal conductivity  $k^*$ , specific heat  $c^*$ , thermal diffusivity  $\kappa^* = k^* / \rho^* c^*$ , kinematic viscosity  $\nu^*$ , dynamic viscosity  $\mu^*$ , thermal expansion coefficient  $\Gamma^*$  and variations of its density  $\rho^*$  follow the Boussinesq approximation. The gravitational acceleration  $g^*$  is acting in the negative  $y^*$ -direction.

Considering the velocity scale to be  $U_v^* = \nu^* / h^*$  and the pressure scale to be  $\rho^* U_v^{*2}$ , the dimensionless field equations take the following form:

$$u \frac{\partial u}{\partial x} + v \frac{\partial v}{\partial y} = 0, \quad (2.6a)$$

$$u \frac{\partial u}{\partial x} + v \frac{\partial u}{\partial y} = -\frac{\partial p}{\partial x} + \nabla^2 u, \quad (2.6b)$$



$$u \frac{\partial v}{\partial x} + v \frac{\partial v}{\partial y} = -\frac{\partial p}{\partial y} + \nabla^2 v + Pr^{-1} \theta, \quad (2.6c)$$

$$u \frac{\partial \theta}{\partial x} + v \frac{\partial \theta}{\partial y} = Pr^{-1} \nabla^2 \theta \quad (2.6d)$$

where  $(u, v)$  are the velocity components in the  $(x, y)$  directions, respectively,  $p$  stands for the pressure,  $\theta$  denotes the temperature and  $Pr = \nu^*/\kappa^*$  is the Prandtl number.

## 2.4 Boundary conditions

The system (2.6) is subject to the following boundary conditions

(i) The no-slip conditions:

$$u(y_L(x)) = 0, \quad (2.7a)$$

$$u(1) = Re \quad (2.7b)$$

where  $Re$  is the Reynolds number defined as  $Re = U_{top}^*/U_v^* = U_{top}^* h^*/\nu^*$ .

(ii) The no-penetration conditions:

$$v(y_L(x)) = 0, \quad (2.7c)$$

$$v(1) = 0. \quad (2.7d)$$

(iii) The thermal conditions:

$$\theta(y_L(x)) = \theta_L(x), \quad (2.7e)$$

$$\theta(1) = 0. \quad (2.7f)$$

## 2.5 Flow constraint

No mean horizontal pressure gradient is permitted in the flow system, hence one must impose constraint of the form

$$\left. \frac{\partial p}{\partial x} \right|_{mean} = 0. \quad (2.8)$$

## 2.6 Reference isothermal case

When the above system is isothermal, and both plate surfaces are smooth, the fluid movement in the gap is solely caused by the motion of the upper plate, and is given as

$$\mathbf{v}_0(x, y) = [u_0(y), 0] = \left[ \frac{1}{2}(1 + y), 0 \right], \quad (2.9a)$$

$$p_0(x, y) = C. \quad (2.9b)$$

The fluid flow rate in the gap is

$$Q_0 = 1, \quad (2.9c)$$

the shear stress acting on the upper plate is

$$\tau_0 = -0.5. \quad (2.9d)$$

and the force (per unit length and unit width) required to pull the upper plate is given as

$$F_0 = 0.5. \quad (2.9e)$$

In the above, the velocity vector  $\mathbf{v}_0$  has been scaled with  $U_{top}^*$  as the velocity scale,  $Q_0$  stands for the flow rate scaled with the same velocity scale,  $\tau_0$  stands for the shear acting on the upper plate scaled with  $U_{top}^* \mu^* / h^*$ ,  $F_0$  denotes the force per unit length and width required to drive the upper plate scaled with  $U_{top}^* \mu^* / h^*$ .

## 2.7 Driving force

Certain force must be applied to the upper plate to maintain its movement, and the magnitude of this force is determined by shear forces acting on its surface.

The presence of the grooves and the heating results in changes in the shear stress acting on the upper plate,  $\Delta\tau^* = \tau^* - \tau_0^*$ , which, when scaled with  $U_v^*\mu^*/h^*$ , has the form

$$\Delta\tau = -\left.\frac{du}{dy}\right|_{y=1} + \frac{1}{2}Re. \quad (2.10)$$

The change in the driving force,  $\Delta F^* = F_0^* - F^*$ , scaled with  $\rho^*U_v^{*2}$ , can be expressed as

$$\Delta F = F_0 - F = Re \left( \frac{1}{2} - Re^{-1}\lambda^{-1} \int_0^\lambda \left.\frac{du}{dy}\right|_{y=1} dx \right). \quad (2.11)$$

## 2.8 Flow rate

The change in the amount of fluid pulled by the plate,  $\Delta Q^* = Q^* - Q_0^*$ , scaled with  $U_v^*$ , can be expressed as

$$\Delta Q = Re \left[ Re^{-1} \left( \int_{-1}^1 u(x, y) dy \right) \Big|_{mean} - 1 \right]. \quad (2.12)$$

## 2.9 Heat transfer

The external heating required to produce the desired temperature along the lower plate leads to a heat flow between the plates which can be viewed as an energy cost associated with the use of the heating for altering the driving force. This heat flow is expressed in terms on the mean Nusselt number defined as

$$Nu_{av} = \lambda^{-1} \int_0^\lambda \left.\frac{\partial\theta}{\partial y}\right|_{y=1} dx. \quad (2.13)$$

## Chapter 3

### 3 Solution procedure

This chapter focuses on describing the procedure used for the determination of a solution for the problem presented in Chapter 2. It describes the discretization procedure for the field equations and boundary conditions, and the efficient solution process for solving these equations. The solution method presented in this chapter is based on the method described by Abtahi, *et al.* (2016) and Husain & Floryan (2013).

#### 3.1 Stream function formulation

The field equations presented in Section 2.3 are to be expressed in terms of the stream function  $\psi$  defined as

$$u = \frac{\partial \psi}{\partial y}, \quad v = -\frac{\partial \psi}{\partial x}. \quad (3.1)$$

The above definition of stream function automatically satisfies the continuity equation (2.6a) and facilitates elimination of the pressure terms from the momentum equations (2.6b-c). The field equations take the following final form

$$\nabla^4 \psi - Pr^{-1} \frac{\partial \theta}{\partial x} = N_{VV}, \quad (3.2a)$$

$$\nabla^2 \theta = Pr N_{V\theta} \quad (3.2b)$$

where the nonlinear terms  $N_{VV}$  and  $N_{V\theta}$  are defined as

$$N_{VV} = \frac{\partial}{\partial y} \left( \frac{\partial}{\partial x} \widehat{u} \widehat{u} + \frac{\partial}{\partial y} \widehat{u} \widehat{v} \right) - \frac{\partial}{\partial x} \left( \frac{\partial}{\partial x} \widehat{u} \widehat{v} + \frac{\partial}{\partial y} \widehat{v} \widehat{v} \right), \quad (3.3a)$$

$$N_{V\theta} = \frac{\partial}{\partial x} \widehat{u} \widehat{\theta} + \frac{\partial}{\partial y} \widehat{v} \widehat{\theta}. \quad (3.3b)$$

The symbol  $\widehat{u} \widehat{u}$  refers to a product of two functions.

The boundary conditions (2.7a-f) expressed in terms of the stream function assume the following forms

$$\frac{\partial \psi}{\partial y}(y_L(x)) = 0, \quad (3.4a)$$

$$\frac{\partial \psi}{\partial y}(y_U(x)) = Re, \quad (3.4b)$$

$$\frac{\partial \psi}{\partial x}(y_L(x)) = 0, \quad (3.4c)$$

$$\frac{\partial \psi}{\partial x}(y_U(x)) = 0, \quad (3.4d)$$

$$\theta(y_L(x)) = \theta_L(x), \quad (3.4e)$$

$$\theta(y_U(x)) = \theta_U(x). \quad (3.4f)$$

### 3.2 Treatment of the irregular geometry

The geometric irregularity of the flow domain is taken care of by using the Immersed Boundary Conditions (IBC) (Mittal & Iaccarino, 2005; Peskin, 2002; Szumbarski & Floryan, 1999) concept where a fixed rectangular computational domain is used that is sufficiently large to contain the flow domain in its interior. The computational domain consists of one period in the  $x$ -direction and  $(-1 - y_b, 1)$  in the  $y$ -direction, where  $y_b$  is the location of the lower extremity of the lower plate (see Section 2.1). Since Chebyshev expansions shall be used for discretizing of the transverse direction, one needs to use their standard definition, i.e. the  $y$ -extent of the computational domain needs to be mapped into  $(-1, 1)$ . Mapping having the form of

$$\hat{y} = 2 \left[ \frac{y-1}{y_b+2} \right] + 1, \quad (3.5)$$

has been used in this work.

### 3.3 Field equations in the computational plane

The field equations (3.2a-b) expressed using the  $(x, \hat{y})$ -coordinates take the form

$$\frac{\partial^4 \psi}{\partial x^4} + 2\Gamma^2 \frac{\partial^4 \psi}{\partial x^2 \partial \hat{y}^2} + \Gamma^4 \frac{\partial^4 \psi}{\partial \hat{y}^4} - Pr^{-1} \frac{\partial \theta}{\partial x} = N_{VV}, \quad (3.6a)$$

$$\frac{\partial^2 \theta}{\partial x^2} + \Gamma^2 \frac{\partial^2 \theta}{\partial \hat{y}^2} = Pr N_{V\theta} \quad (3.6b)$$

where  $\Gamma = \frac{d\hat{y}}{dy} = \frac{2}{y_b+2}$  and the nonlinear terms become

$$N_{VV} = \Gamma \frac{\partial}{\partial \hat{y}} \left( \frac{\partial}{\partial x} \widehat{u\hat{u}} + \Gamma \frac{\partial}{\partial \hat{y}} \widehat{u\hat{v}} \right) - \frac{\partial}{\partial x} \left( \frac{\partial}{\partial x} \widehat{u\hat{v}} + \Gamma \frac{\partial}{\partial \hat{y}} \widehat{v\hat{v}} \right), \quad (3.7a)$$

$$N_{V\theta} = \frac{\partial}{\partial x} \widehat{u\hat{\theta}} + \Gamma \frac{\partial}{\partial \hat{y}} \widehat{v\hat{\theta}}. \quad (3.7b)$$

The boundary conditions are changed to the following forms

$$\frac{\partial \psi}{\partial \hat{y}}(\hat{y}_L(x)) = 0, \quad \frac{\partial \psi}{\partial \hat{y}}(\hat{y}_U(x)) = Re. \quad (3.8a, b)$$

$$\frac{\partial \psi}{\partial x}(\hat{y}_L(x)) = 0, \quad \frac{\partial \psi}{\partial x}(\hat{y}_U(x)) = 0. \quad (3.8c, d)$$

$$\theta(\hat{y}_L(x)) = \theta_L(x), \quad \theta(\hat{y}_U(x)) = \theta_U(x) \quad (3.8e, f)$$

where

$$\hat{y}_L(x) = 1 + \Gamma(y_b \cos(\alpha x) - 1). \quad (3.9)$$

### 3.4 Discretization of the field equations

The  $x$ -dependences of the stream function  $\psi$  as well as temperature  $\theta$  are captured by expressing them as Fourier expansions based on the wavenumber  $\alpha$ , i.e.

$$\psi(x, \hat{y}) = \sum_{n=-\infty}^{+\infty} \varphi^{(n)}(\hat{y}) e^{in\alpha x} \approx \sum_{n=-N_M}^{N_M} \varphi^{(n)}(\hat{y}) e^{in\alpha x}, \quad (3.10a)$$

$$\theta(x, \hat{y}) = \sum_{n=-\infty}^{+\infty} \phi^{(n)}(\hat{y}) e^{inax} \approx \sum_{n=-N_M}^{N_M} \phi^{(n)}(\hat{y}) e^{inax}. \quad (3.10b)$$

The nonlinear terms are also expressed as Fourier expansions of the form

$$\begin{aligned} [\widehat{uu}, \widehat{uv}, \widehat{vv}, \widehat{u\theta}, \widehat{v\theta}](x, \hat{y}) &= \sum_{n=-\infty}^{+\infty} [\widehat{uu}^{(n)}, \widehat{uv}^{(n)}, \widehat{vv}^{(n)}, \widehat{u\theta}^{(n)}, \widehat{v\theta}^{(n)}](\hat{y}) e^{inax} \approx \\ &\sum_{n=-N_M}^{N_M} [\widehat{uu}^{(n)}, \widehat{uv}^{(n)}, \widehat{vv}^{(n)}, \widehat{u\theta}^{(n)}, \widehat{v\theta}^{(n)}](\hat{y}) e^{inax}. \end{aligned} \quad (3.10c)$$

where  $\phi^{(n)} = \phi^{(-n)*}$ ,  $\phi^{(n)} = \phi^{(-n)*}$ ,  $\widehat{uu}^{(n)} = \widehat{uu}^{(-n)*}$ ,  $\widehat{uv}^{(n)} = \widehat{uv}^{(-n)*}$ ,  $\widehat{vv}^{(n)} = \widehat{vv}^{(-n)*}$ ,  $\widehat{u\theta}^{(n)} = \widehat{u\theta}^{(-n)*}$ ,  $\widehat{v\theta}^{(n)} = \widehat{v\theta}^{(-n)*}$  represent the reality conditions with \* denoting the complex conjugates.

Substituting (3.10) in (3.6) and separating the Fourier modes lead to the modal equations of the form

$$D_n^2 \phi^{(n)} - in\alpha Pr^{-1} \phi^{(n)} = N_{VV}^{(n)}, \quad (3.11a)$$

$$D_n \phi^{(n)} = Pr N_{V\theta}^{(n)} \quad (3.11b)$$

for  $-N_m < n < N_m$ , where  $D = d/d\hat{y}$ ,  $D_n = \Gamma^2 D^2 - n^2 \alpha^2$ ,  $D_n^2 = \Gamma^4 D^4 - 2n^2 \alpha^2 \Gamma^2 D^2 + n^4 \alpha^4$ ,  $N_{VV}^{(n)} = in\alpha \Gamma D \widehat{uu}^{(n)} + (\Gamma^2 D^2 + n^2 \alpha^2) \widehat{uv}^{(n)} - in\alpha \Gamma D \widehat{vv}^{(n)}$ ,  $N_{V\theta}^{(n)} = in\alpha \widehat{u\theta}^{(n)} + \Gamma D \widehat{v\theta}^{(n)}$ .

The modal functions are then expressed in terms of Chebyshev expansions of the form

$$\phi^{(n)}(\hat{y}) = \sum_{k=0}^{k=\infty} \widehat{G\phi}_k^{(n)} T_k(\hat{y}) \approx \sum_{k=0}^{k=N_T-1} \widehat{G\phi}_k^{(n)} T_k(\hat{y}), \quad (3.12a)$$

$$\phi^{(n)}(\hat{y}) = \sum_{k=0}^{k=\infty} \widehat{G\phi}_k^{(n)} T_k(\hat{y}) \approx \sum_{k=0}^{k=N_T-1} \widehat{G\phi}_k^{(n)} T_k(\hat{y}), \quad (3.12b)$$

$$\begin{aligned} [\widehat{uu}^{(n)}, \widehat{uv}^{(n)}, \widehat{vv}^{(n)}, \widehat{u\theta}^{(n)}, \widehat{v\theta}^{(n)}](\hat{y}) &= \\ \sum_{k=0}^{k=\infty} [\widehat{Guu}_k^{(n)}, \widehat{Guv}_k^{(n)}, \widehat{Gvv}_k^{(n)}, \widehat{Gu\theta}_k^{(n)}, \widehat{Gv\theta}_k^{(n)}] T_k(\hat{y}) &\approx \\ \sum_{k=0}^{k=N_T-1} [\widehat{Guu}_k^{(n)}, \widehat{Guv}_k^{(n)}, \widehat{Gvv}_k^{(n)}, \widehat{Gu\theta}_k^{(n)}, \widehat{Gv\theta}_k^{(n)}] T_k(\hat{y}) &\end{aligned} \quad (3.12c)$$

where  $T_k$  are the Chebyshev polynomials of the first kind of order  $k$  and  $\widehat{Gxx}_k^{(n)}$  denotes the unknown expansion coefficients.

Substitution of (3.12) into (3.11) leads to

$$\sum_{k=0}^{N_T-1} \left[ (\Gamma^4 D^4 T_k(\hat{y}) - 2n^2 \alpha^2 \Gamma^2 D^2 T_k(\hat{y}) + n^4 \alpha^4 T_k(\hat{y})) \widehat{G\phi}_k^{(n)} - \right. \\ \left. i n \alpha P r^{-1} T_k(\hat{y}) \widehat{G\theta}_k^{(n)} \right] - N_{VV}^{(n,k)} = Res_1(\hat{y}), \quad (3.13a)$$

$$\sum_{k=0}^{N_T-1} \left[ (\Gamma^2 D^2 T_k(\hat{y}) - n^2 \alpha^2 T_k(\hat{y})) \widehat{G\theta}_k^{(n)} \right] - Pr N_{V\theta}^{(n,k)} = Res_2(\hat{y}). \quad (3.13b)$$

where the modal functions for the nonlinear terms have been represented as Chebyshev expansions of the form

$$N_{VV}^{(n,k)} = \sum_{k=0}^{N_T-1} \left[ i n \alpha \Gamma D T_k(\hat{y}) \widehat{Guv}_k^{(n)} + (\Gamma^2 D^2 T_k(\hat{y}) + n^2 \alpha^2 T_k(\hat{y})) \widehat{Guv}_k^{(n)} - \right. \\ \left. i n \alpha \Gamma D T_k(\hat{y}) \widehat{Gv}_k^{(n)} \right], \quad (3.14a)$$

$$N_{V\theta}^{(n,k)} = \sum_{k=0}^{N_T-1} \left[ i n \alpha T_k(\hat{y}) \widehat{Gu\theta}_k^{(n)} + \Gamma D T_k(\hat{y}) \widehat{Gv\theta}_k^{(n)} \right]. \quad (3.14b)$$

In (3.13),  $Res_1$  and  $Res_2$  denote residua. The nonlinear terms are considered to be known during the iterative solution. The equations for the unknown expansion coefficients are constructed using the Galerkin projection method which involves the setting of projections of  $Res_1$  and  $Res_2$  onto the base functions of the Chebyshev expansions to zero. This leads to the  $N_T$  number of equations for each of the Fourier modes. The projections are evaluated using the inner product defined as

$$\langle Res(\hat{y}), T_k(\hat{y}) \rangle = \int_{-1}^1 Res(\hat{y}) T_k(\hat{y}) \omega(\hat{y}) d\hat{y} \quad (3.15)$$

where the weight function has the form of  $\omega(\hat{y}) = (1 - \hat{y}^2)^{-1/2}$ .

The projection equations have the form



$$\begin{aligned} \sum_{k=0}^{k=N_T-1} \left[ (\Gamma^4 \langle T_j, D^4 T_k \rangle - 2n^2 \alpha^2 \Gamma^2 \langle T_j, D^2 T_k \rangle + n^4 \alpha^4 \langle T_j, T_k \rangle) \widehat{G\phi}_k^{(n)} - \right. \\ \left. in\alpha Pr^{-1} \langle T_j, T_k \rangle \widehat{G\phi}_k^{(n)} \right] = \sum_{k=0}^{k=N_T-1} \left[ in\alpha \Gamma \langle T_j, DT_k \rangle \widehat{G\mathbf{u}}_k^{(n)} + (\Gamma^2 \langle T_j, T_k \rangle + \right. \\ \left. n^2 \alpha^2 \langle T_j, T_k \rangle) \widehat{G\mathbf{u}}_k^{(n)} - in\alpha \Gamma \langle T_j, DT_k \rangle \widehat{G\mathbf{v}}_k^{(n)} \right], \quad 0 \leq j \leq N_T - 5 \end{aligned} \quad (3.16a)$$

$$\begin{aligned} \sum_{k=0}^{k=N_T-1} \left[ (\Gamma^2 \langle T_j, D^2 T_k \rangle - n^2 \alpha^2 \langle T_j, T_k \rangle) \widehat{G\mathbf{v}}_k^{(n)} \right] = \Pr \sum_{k=0}^{k=N_T-1} \left[ in\alpha \langle T_j, T_k \rangle \widehat{G\mathbf{u}}_k^{(n)} + \right. \\ \left. \Gamma \langle T_j, DT_k \rangle \widehat{G\mathbf{v}}_k^{(n)} \right]. \quad 0 \leq j \leq N_T - 3 \end{aligned} \quad (3.16b)$$

where only the leading  $N_T - 4$  equations resulting from the momentum equations and  $N_T - 2$  of the equations resulting from the energy equations are retained in order to provide space for the boundary conditions (Tau method). Details of the evaluation of the inner products are discussed in Appendix A.

### 3.5 Discretization of the boundary conditions

It is now necessary to implement the flow and thermal boundary conditions along the flow domain boundaries which are located inside the computational domain. Substituting (3.10a-b) in (3.8) provides the boundary conditions of the form

$$\sum_{n=-N_M}^{n=+N_M} \frac{\partial \varphi^{(n)}(\hat{y}_L(x))}{\partial \hat{y}} e^{in\alpha x} = 0, \quad (3.17a)$$

$$\sum_{n=-N_M}^{n=+N_M} \frac{\partial \varphi^{(n)}(\hat{y}_U(x))}{\partial \hat{y}} e^{in\alpha x} = Re, \quad (3.17b)$$

$$\sum_{n=-N_M}^{n=+N_M} n \varphi^{(n)}(\hat{y}_L(x)) e^{in\alpha x} = 0, \quad (3.17c)$$

$$\sum_{n=-N_M}^{n=+N_M} n \varphi^{(n)}(\hat{y}_U(x)) e^{in\alpha x} = 0, \quad (3.17d)$$

$$\sum_{n=-N_M}^{n=+N_M} \varphi^{(n)}(\hat{y}_L(x)) e^{in\alpha x} = \theta_L(x), \quad (3.17e)$$

$$\sum_{n=-N_M}^{n=+N_M} \varphi^{(n)}(\hat{y}_U(x)) e^{in\alpha x} = \theta_U(x). \quad (3.17f)$$

It should be noted that (3.17c-d) do not provide conditions for  $n = 0$ .

Substitution of the Chebyshev expansions (3.12) for the modal functions into (3.17) leads to

$$\sum_{n=-N_M}^{n=+N_M} \sum_{k=0}^{k=N_T-1} \widehat{G\varphi}_k^{(n)} DT_k(\hat{y}_L(x)) e^{inax} = 0, \quad (3.18a)$$

$$\sum_{n=-N_M}^{n=+N_M} \sum_{k=0}^{k=N_T-1} \widehat{G\varphi}_k^{(n)} DT_k(1) = Re, \quad (3.18b)$$

$$\sum_{n=-N_M}^{n=+N_M} \sum_{k=0}^{k=N_T-1} n \widehat{G\varphi}_k^{(n)} T_k(\hat{y}_L(x)) e^{inax} = 0, \quad (3.18c)$$

$$\sum_{n=-N_M}^{n=+N_M} \sum_{k=0}^{k=N_T-1} n \widehat{G\varphi}_k^{(n)} T_k(1) = 0, \quad (3.18d)$$

$$\sum_{n=-N_M}^{n=+N_M} \sum_{k=0}^{k=N_T-1} \widehat{G\varphi}_k^{(n)} T_k(\hat{y}_L(x)) e^{inax} = \theta_L(x). \quad (3.18e)$$

$$\sum_{n=-N_M}^{n=+N_M} \sum_{k=0}^{k=N_T-1} \widehat{G\varphi}_k^{(n)} T_k(1) = \theta_U(x). \quad (3.18f)$$

The  $x$ -dependency of the lower plate geometry is tackled by expressing  $\hat{y}_L(x)$  given by (3.9) in terms of Fourier expansion as

$$\hat{y}_L(x) = \sum_{n=-N_A}^{n=+N_A} A_L^{(n)} e^{inax} \quad (3.19)$$

where  $N_A$  denotes the number of modes used to describe plate geometry and  $A_L^{(n)}$  are the known expansion coefficients. The above form represents a generalization of (3.9) which contains only one Fourier mode while (3.19) is able to represent arbitrary plate geometry. Equations (3.18) require that values of the Chebyshev polynomials and their derivatives be evaluated along the boundary represented by the periodic function of  $x$  and thus can be expressed as Fourier expansions of the form

$$T_k(\hat{y}_L(x)) = \sum_{m=-N_s}^{m=+N_s} \widehat{W}L_k^{(m)} e^{imax}, \quad (3.20a)$$

$$DT_k(\hat{y}_L(x)) = \sum_{m=-N_s}^{m=+N_s} \widehat{D}L_k^{(m)} e^{imax} \quad (3.20b)$$

where  $\widehat{W}L_k^{(m)}$  and  $\widehat{D}L_k^{(m)}$  are the expansion coefficients of the Chebyshev polynomials and their derivatives evaluated along the lower plate. These expansions involve  $N_S = (N_T - 1) * N_A$  terms, as the highest order polynomials are of the order  $N_T - 1$ . Evaluation of those terms relies on recurrence relations that lead to the following expressions (details can be found in the Appendix)

$$\widehat{W}L_{k+1}^{(m)} = 2 \sum_{n=-N_A}^{n=+N_A} A_L^{(n)} \widehat{W}L_k^{(m-n)} - \widehat{W}L_{k-1}^{(m)}, \quad (3.21a)$$

$$\widehat{D}L_{k+1}^{(m)} = 2 \sum_{n=-N_A}^{n=+N_A} A_L^{(n)} \widehat{D}L_k^{(m-n)} - \widehat{D}L_{k-1}^{(m)} + 2\widehat{W}L_k^{(m)}. \quad (3.21b)$$

The evaluation process begins with  $k = 0$  and results in

$$\widehat{W}L_0^{(0)} = 1, \quad \widehat{W}L_0^{(m)} = 0 \text{ for } |m| \geq 0, \quad \widehat{W}L_0^{(m)} = A_L^{(m)} \text{ for } |m| \geq 0, \quad (3.22a-c)$$

$$\widehat{D}L_0^{(m)} = 0 \text{ for } |m| \geq 0, \quad \widehat{D}L_1^{(0)} = 1, \quad (3.22d, e)$$

$$\widehat{D}L_1^{(m)} = 0 \text{ for } |m| \geq 1, \quad \widehat{D}L_1^{(m)} = 4A_L^{(m)}, \text{ for } |m| \geq 0. \quad (3.22f, g)$$

Substituting (3.20) into (3.18) and separating Fourier modes leads to boundary relations of the form

$$\sum_{m=-N_M}^{m=+N_M} \sum_{k=0}^{k=N_T-1} \widehat{G}\phi_k^{(m)} \widehat{D}L_k^{(n-m)} = 0, \quad (3.24a)$$

$$\sum_{m=-N_M}^{m=+N_M} \sum_{k=0}^{k=N_T-1} \widehat{G}\phi_k^{(m)} \widehat{D}U_k^{(n-m)} = Re, \quad (3.24b)$$

$$\sum_{m=-N_M}^{m=+N_M} \sum_{k=0}^{k=N_T-1} n \widehat{G}\phi_k^{(m)} \widehat{W}L_k^{(n-m)} = 0, \quad (3.24c)$$

$$\sum_{m=-N_M}^{m=+N_M} \sum_{k=0}^{k=N_T-1} n \widehat{G}\phi_k^{(m)} \widehat{W}U_k^{(n-m)} = 0, \quad (3.24d)$$

$$\sum_{m=-N_M}^{m=+N_M} \sum_{k=0}^{k=N_T-1} \widehat{G}\phi_k^{(m)} \widehat{W}L_k^{(n-m)} = \theta_L^{(n)}, \quad (3.24e)$$

$$\sum_{m=-N_M}^{m=+N_M} \sum_{k=0}^{k=N_T-1} \widehat{G}\phi_k^{(m)} \widehat{W}U_k^{(n-m)} = \theta_U^{(n)} \quad (3.24f)$$

which represent the boundary conditions along the grooved plate.

### 3.6 Discretization of the pressure gradient constraint

The discretized field equations (3.16) and boundary conditions (3.24) described in the previous sections need one additional closing constraint. This constraint needs to express the fact that the mean pressure gradient must be zero (see Eq. 2.8).

In order to discretize this constraint, one needs to evaluate the pressure gradient from the  $x$ -momentum equation (2.6b) expressed in terms of the stream function  $\psi$  as

$$\frac{\partial p}{\partial x} = \Gamma \frac{\partial^3 \psi}{\partial x^2 \partial \hat{y}} + \Gamma^3 \frac{\partial^3 \psi}{\partial \hat{y}^3} - \frac{\partial}{\partial x} \widehat{u} \widehat{u} - \Gamma \frac{\partial}{\partial \hat{y}} \widehat{u} \widehat{v}. \quad (3.25)$$

The pressure field is represented as a Fourier expansion of the form

$$p(x, \hat{y}) = Ax + \sum_{n=-\infty}^{+\infty} p^{(n)}(\hat{y}) e^{in\alpha x} \approx Ax + \sum_{n=-N_M}^{+N_M} p^{(n)}(\hat{y}) e^{in\alpha x} \quad (3.26)$$

where  $A$  is the mean pressure gradient. Substituting (3.10) and (3.26) into (3.25) and separating the Fourier modes lead to equations for the pressure modal functions of the forms

$$A + in\alpha p^{(n)} = (\Gamma^3 D^3 - n^2 \alpha^2 \Gamma D) \varphi^{(n)} - in\alpha \widehat{u} \widehat{u}^{(n)} - \Gamma D \widehat{u} \widehat{v}^{(n)}. \quad (3.27)$$

The mean pressure gradient is determined from the modal equation for mode  $n = 0$  which has the following form

$$A = \Gamma^3 D^3 \varphi^{(0)} - \Gamma D \widehat{u} \widehat{v}^{(0)}. \quad (3.28)$$

Substitution of the Chebyshev expansion (3.12) into the modal functions present in (3.28) leads to

$$A = \sum_{k=0}^{N_T-1} \left[ \Gamma^3 \widehat{G} \varphi_k^{(0)} D^3 T_k(\hat{y}) - \Gamma \widehat{G} \widehat{u} \widehat{v}_k^{(0)} D T_k(\hat{y}) \right]. \quad (3.29)$$

Finally, the flow constraint translates to

$$A = \sum_{k=0}^{N_T-1} \left[ \Gamma^3 \widehat{G} \varphi_k^{(0)} D^3 T_k(\hat{y}) - \Gamma \widehat{G} \widehat{u} \widehat{v}_k^{(0)} D T_k(\hat{y}) \right] = 0. \quad (3.30)$$

### 3.7 Numerical solution

An iterative scheme is used to determine the solution to the problem discussed in the previous section. The solution process yields new approximations of  $\widehat{G\varphi}_k^{(n)}$  and  $\widehat{G\varnothing}_k^{(n)}$  expressed as  $[\widehat{G\varphi}_k^{(n)}]^{(l+1)}$  and  $[\widehat{G\varnothing}_k^{(n)}]^{(l+1)}$  after each iteration where the subscript  $l$  denotes the iteration number. The nonlinear terms on the right-hand side of (3.16) are taken from the previous iteration (they are ignored during the first iteration) which results in the first order fixed point method. This process can be expressed as

$$[\widehat{G\varphi}_k^{(n)}]^{(l+1)} = [\widehat{G\varphi}_k^{(n)}]^{(l)} + RF_\varphi \left\{ [\widehat{G\varphi}_k^{(n)}]^{(comp)} - [\widehat{G\varphi}_k^{(n)}]^{(l)} \right\}, \quad (3.31a)$$

$$[\widehat{G\varnothing}_k^{(n)}]^{(l+1)} = [\widehat{G\varnothing}_k^{(n)}]^{(l)} + RF_\varnothing \left\{ [\widehat{G\varnothing}_k^{(n)}]^{(comp)} - [\widehat{G\varnothing}_k^{(n)}]^{(l)} \right\}, \quad (3.31b)$$

where the superscript *comp* is the solution computed at the new iteration, and the process is controlled using under-relaxation parameters  $RF_\varphi$  and  $RF_\varnothing$ . Iterations are continued until a convergence criterion of the form

$$\frac{\left\| [\widehat{G\varphi}_k^{(n)}]^{(l+1)} - [\widehat{G\varphi}_k^{(n)}]^{(l)} \right\|_2}{\left\| [\widehat{G\varphi}_k^{(n)}]^{(l+1)} \right\|_2} < CONV, \quad (3.32a)$$

$$\frac{\left\| [\widehat{G\varnothing}_k^{(n)}]^{(l+1)} - [\widehat{G\varnothing}_k^{(n)}]^{(l)} \right\|_2}{\left\| [\widehat{G\varnothing}_k^{(n)}]^{(l+1)} \right\|_2} < CONV \quad (3.32b)$$

is satisfied.  $CONV=10^{-8}$  is used for all results presented in this study. In the above, the  $L_2$  norm of a vector  $V$  with size  $n$  is defined as  $\|V\|_2 = \sqrt{(\sum_{i=1}^n |V_i|^2)}$ .

As the nonlinear terms need to be updated after each iteration, it is more efficient to evaluate the required products by transferring data to the physical space, carrying out the

multiplications in the physical space, and then transferring the results back to the Fourier space. The velocity components and the temperature are thus expressed as

$$u(x, \hat{y}) = \Gamma \sum_{n=-N_M}^{n=N_M} \sum_{k=0}^{k=N_T-1} \widehat{G\varphi}_k^{(n)} DT_k(\hat{y}) e^{in\alpha x}, \quad (3.33a)$$

$$v(x, \hat{y}) = -i\alpha \sum_{n=-N_M}^{n=N_M} \sum_{k=0}^{k=N_T-1} n \widehat{G\varphi}_k^{(n)} T_k(\hat{y}_U(\hat{y})) e^{in\alpha x}, \quad (3.33b)$$

$$\theta(x, \hat{y}) = \sum_{n=-N_M}^{n=N_M} \sum_{k=0}^{k=N_T-1} \widehat{G\varphi}_k^{(n)} T_k(\hat{y}) e^{in\alpha x}, \quad (3.33c)$$

and are evaluated on a suitable grid in the  $(x, \hat{y})$  plane having  $2N_x + 2$  equidistant points in the  $x$ -direction. Here  $N_x = \frac{3}{2}N_M$  in order to remove the aliasing error.

## Chapter 4

### 4 Flow between heated smooth parallel plates in relative motion

This chapter presents discussion of the dynamics of the flow system when both plates are smooth, and the lower plate is exposed to periodic heating. The sketch of the flow system is shown in Figure 4-1. The geometry of the lower plate is described by taking the groove amplitude  $y_b^* = 0$  in Eq. (2.1a). The computational domain in the  $y^*$ -direction extends from  $-h^*$  to  $+h^*$  (it is  $[-1, 1]$  in the dimensionless form). This makes the solution process slightly easier compared with the general case involving the irregular geometry of the lower plate.

An external force is required for maintaining a steady motion in the upper plate. To reduce the magnitude of this force, the lower plate is exposed to a spatially periodic heating. Flow dynamics for the case of a purely periodic heating is discussed in Section 4.1. Such heating corresponds to a situation where the mean temperatures of both plates are equal. Section 4.2 describes the effect of the unequal mean temperatures of the plates while the lower plate is still exposed to a periodic heating. Unless otherwise stated, the results are presented for fluids with the Prandtl number  $Pr = 0.71$  which approximates the properties of air. Effects associated with the use of other fluids (by changing  $Pr$ ) are discussed in Section 4.3. Heat transfer characteristics are elucidated in Section 4.4. System dynamics for the flipped system, i.e. heated upper plate and moving lower plate are discussed in Section 4.5. Finally, a brief summary is presented in Section 4.6.

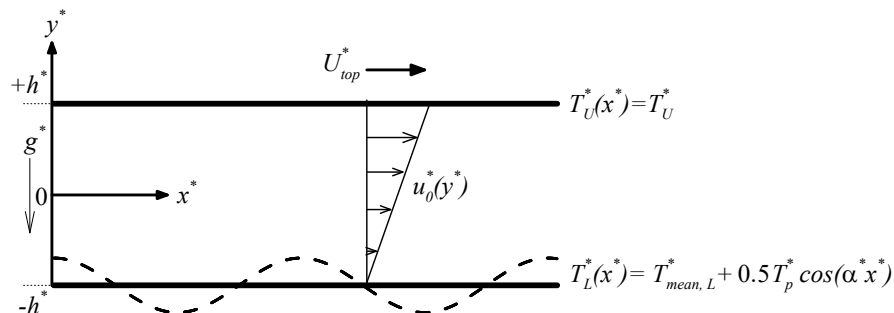


**Figure 4-1:** Schematic diagram of the flow system

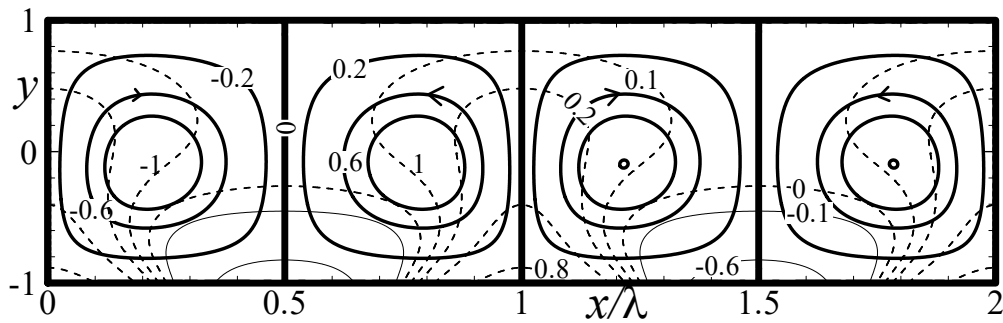
## 4.1 Purely periodic heating at the lower plate

A purely spatially periodic heating corresponds to  $Ra_{uni} = 0$  (see Section 2.2 for definition). When the upper plate is stationary ( $Re = 0$ ), this purely periodic heating results in the formation of convective counter-rotating rolls with the fluid moving upwards above the hot spots and downwards above the cold spots, as illustrated in Figure 4-2A, and its temperature rising above the mean in most of the fluid volume. Slow movement of the upper plate ( $Re = 1$ ) results in a competition between the plate-driven and the buoyancy-driven motions. The flow topology is simple in the zones with the clockwise-rotating rolls as the roll movement is kinematically consistent with the plate movement, resulting in the formation of a single stream of fluid moving in the positive  $x$ -direction located in the immediate vicinity of the moving plate. A complex flow topology forms in the zones with the counterclockwise-rotating rolls as the fluid stream separates into two branches, one flowing above the rolls and one flowing beneath them. The upper branch is dominated by the plate effect, and the lower branch is dominated by the roll effect (see Figure 4-2B). Most of the fluid remains trapped in the rolls, i.e. either in the clockwise rolls attached to the lower plate or in the counter-clockwise rolls bounded by the two branches of the stream moving to the right. The complexity of this topology near the upper plate is illustrated in Figure 4-3. A further increase of the plate velocity ( $Re = 5$ ) results in the dominance of the plate-driven movement with most of the fluid moving to the right, the elimination of the counterclockwise rolls and the reduction of the size of the clockwise rolls (see Figure 4-2C) but with the buoyancy effects still providing a significant contribution to the overall flow dynamics. A further increase of  $Re$  results in the eventual elimination of the rolls (see topology for  $Re = 50$  in Figure 4-2D). The sequence of plots displayed in Figure 4-2 illustrates the process of formation of both the flow and thermal boundary layers near the lower plate as  $Re$  increases.

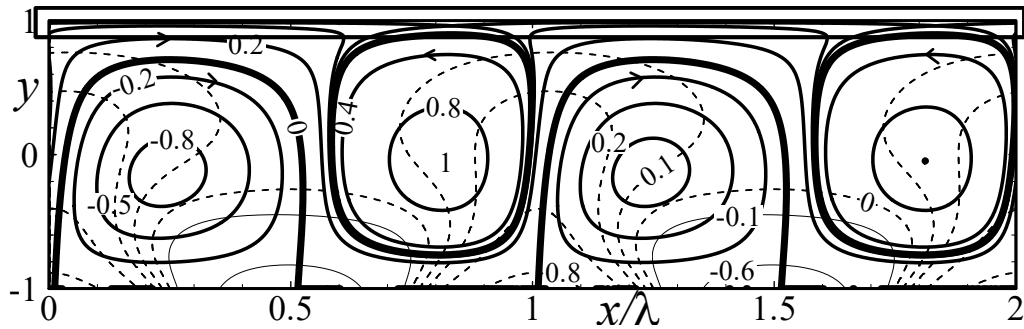
Variations of the local maxima of the stream function associated with the upper plate movement and with both types of rolls as functions of  $Re$  (Figure 4-4) demonstrate that the dominance of the upper plate begins for  $Re > 4$  and, for such conditions, the movement of the clockwise rolls results from both the buoyancy effects as well as the plate-induced pull.



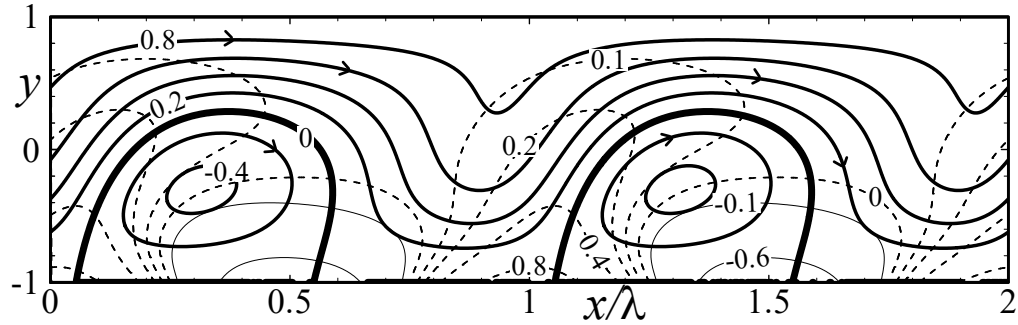
In an isothermal system, the force  $F_0$  given by Eq. (2.9e) is required to maintain the motion of the plate. For non-isothermal systems, the driving force  $F$  needs to be determined through the solution of (2.6) - (2.8). The shear stress acting on the plate varies periodically in  $x$  with its amplitude significantly exceeding the isothermal stress (see Figure 4-5). Its mean value decreases below the isothermal stress and may even change direction. In the latter case, the convection-generated stresses are large enough so that the external force must change direction and act as a brake to maintain the prescribed plate velocity. The positive difference  $\Delta F = F_0 - F$  (see Eq.2.11) identifies conditions leading to the reduction of the driving force and  $\Delta F/Re > 0.5$  identifies conditions when the driving force must change direction, i.e. its role changes from driving the motion of the plate to opposing its motion.



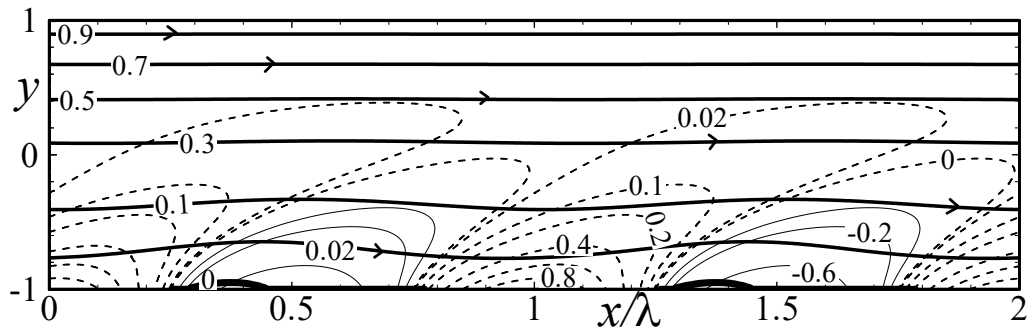
(A)



(B)



(C)



(D)

**Figure 4-2:** The flow and temperature fields for  $Ra_p = 1000$ ,  $Pr = 0.71$ ,  $Ra_{uni} = 0$ ,  $\alpha = 2$  and (A)  $Re = 0$ , (B)  $Re = 1$ , (C)  $Re = 5$ , (D)  $Re = 50$ . Solid and dashed lines identify streamlines and isotherms, respectively. Thick streamlines mark borders of bubbles trapping the fluid. Enlargement of the box shown in Figure 4-2B is displayed in Figure 4-3. Flow conditions used in these plots are marked in Figure 4-10 using squares.

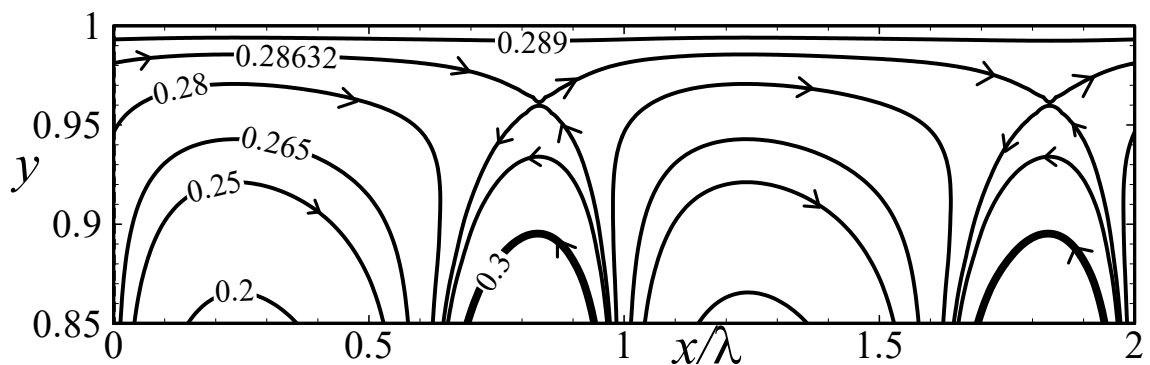


**Figure 4-3:** Enlargement of the box shown in Figure 4-2B. The streamline emanating from the in-flow stagnation points corresponds to  $\psi = 0.286322$ .

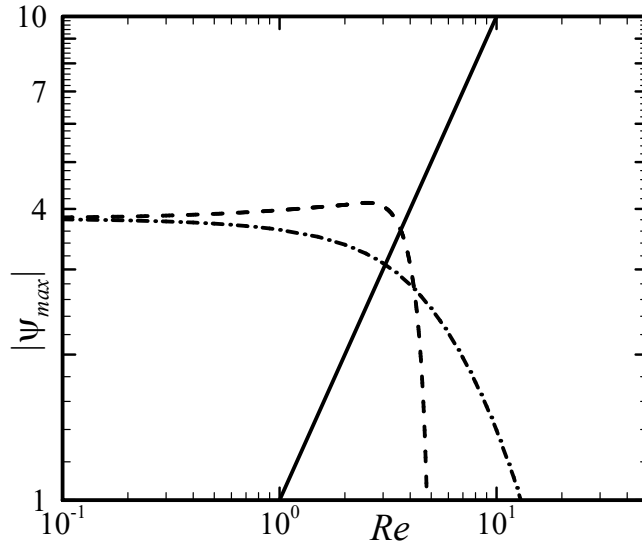


**Figure 4-4:** Variations of the local  $|\psi_{max}|$  associated with the upper plate (solid line), the clockwise rolls (dashed line), and the counterclockwise rolls (dashed-dotted line) as functions of  $Re$  for  $\alpha = 2$ ,  $Ra_p = 1000$ ,  $Pr = 0.71$ ,  $Ra_{uni} = 0$ .

The results presented in Figure 4-6 demonstrate that all heating wavenumbers lead to a decrease of the driving force with the magnitude of this reduction being a strong function of  $\alpha$ . The largest reduction occurs for  $\alpha \approx 1 - 2$  with its magnitude decreasing proportionally to  $\alpha^4$  if an excessively small  $\alpha$  is used. The flow and temperature fields (not shown) are qualitatively similar to those displayed in Figure 4-2. The use of an excessively large  $\alpha$  also results in a reduction of  $\Delta F$  but at a much higher rate, i.e. proportionally to  $\alpha^{-7}$ . Plots of the temperature fields displayed in Figure 4-7 demonstrate that a sufficient increase in  $\alpha$  leads to the formation of a boundary layer close to the lower plate containing convective effects and a conductive layer with a very simple flow topology above it. The qualitatively different dependence on  $Pr$  for small and large  $\alpha$  shows a relatively stronger role of conduction for large  $\alpha$ 's and a relatively stronger role of convection for small  $\alpha$ 's.

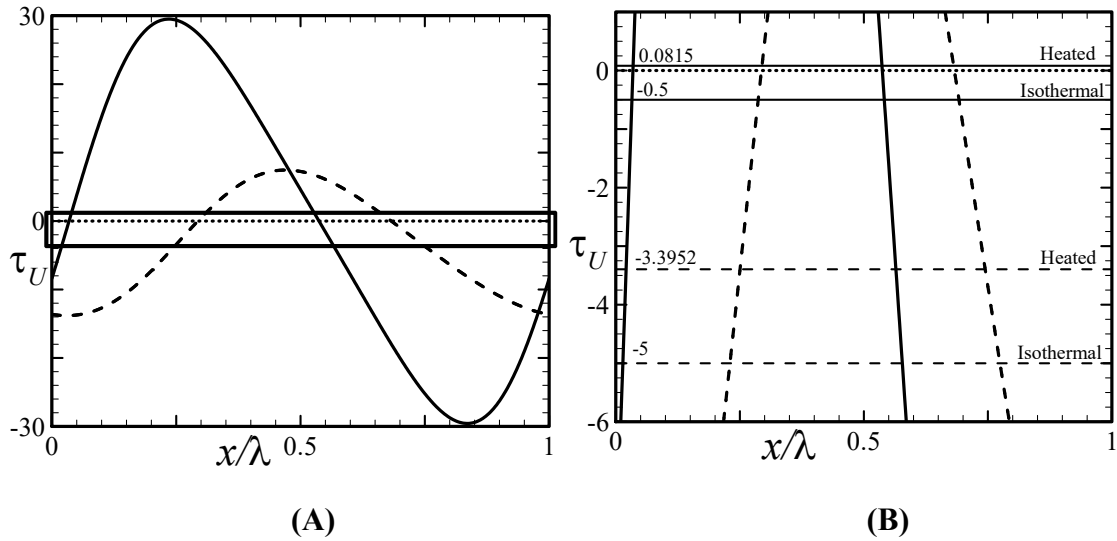


**Figure 4-5:** Distribution of the shear stress  $\tau_U$  acting on the upper plate for  $\alpha = 2$ ,  $Ra_p = 1000$ ,  $Pr = 0.71$ ,  $Ra_{uni} = 0$  at  $Re = 1$  (solid line) and  $Re = 10$  (dashed line). Enlargement of the box shown in Figure 4-5A is displayed in Figure 4-5B including shear mean values.

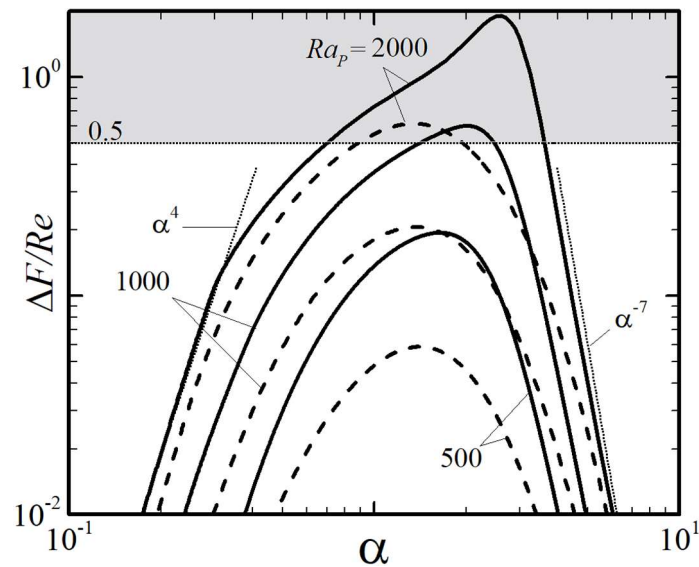
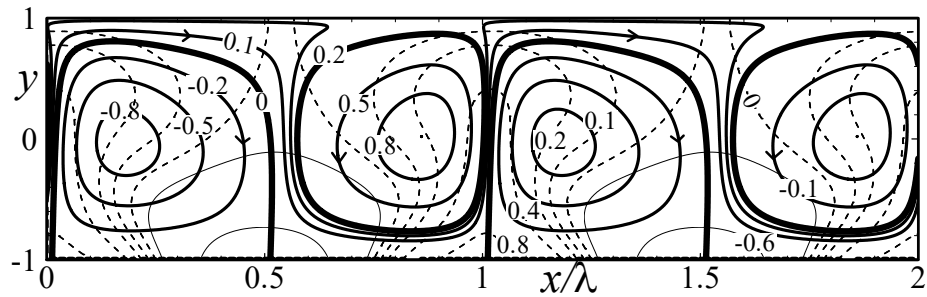
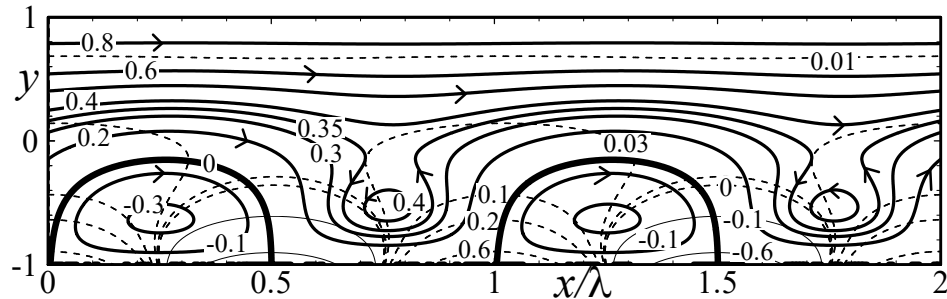


**Figure 4-6:** Variations of  $\Delta F/Re$  as a function of  $\alpha$  for  $Pr = 0.71$ ,  $Ra_{uni} = 0$ ,  $Re = 1$  (solid lines) and  $Re = 10$  (dashed lines). Thin dotted lines identify asymptotes. The shaded area identifies conditions where the driving force must change direction and becomes a braking force.

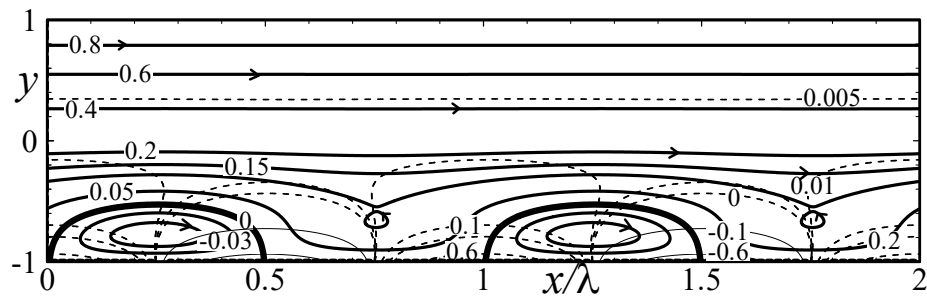
Heating affects the flow rate driven by the motion of the plate. The flow rate generally increases with  $Ra_p$ , as illustrated in Figure 4-8, as the buoyancy force assists the motion of the plate. The maximum increase occurs for the same  $\alpha$ 's as those which produce the largest force reduction. There are special cases, however, where a combination of a sufficiently large  $Ra_p$  with a proper range of small  $\alpha$ 's results in a decrease in the flow rate. This is caused by the formation of various in-flow separation bubbles which block the motion of the fluid in the positive  $x$ -direction as illustrated in Figure 4-9.



(A)



(B)



(C)

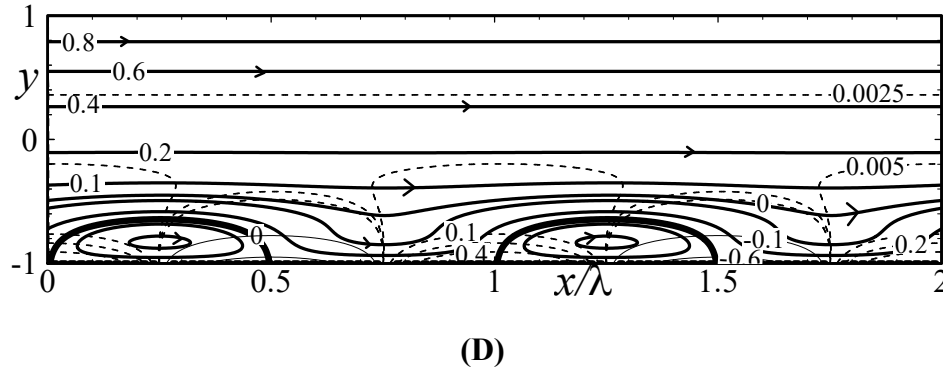


**Figure 4-7:** The flow and temperature fields for  $Ra_p = 1000$ ,  $Pr = 0.71$ ,  $Ra_{uni} = 0$ ,  $Re = 1$  and  $\alpha = 1$  (A),  $\alpha = 5$  (B),  $\alpha = 8$  (C),  $\alpha = 10$  (D). Thick solid lines identify streamlines, thin solid lines identify negative isotherms while thin dashed lines identify positive isotherms. Thick streamlines mark borders of various bubbles trapping the fluid.

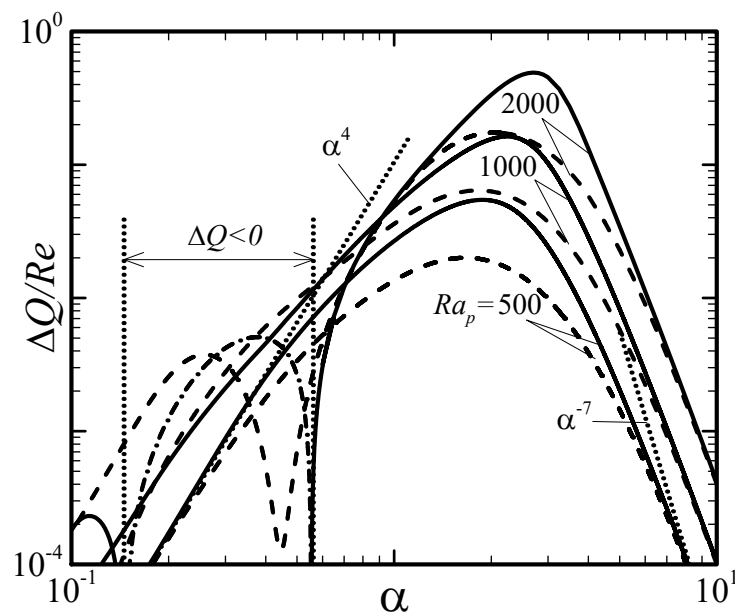
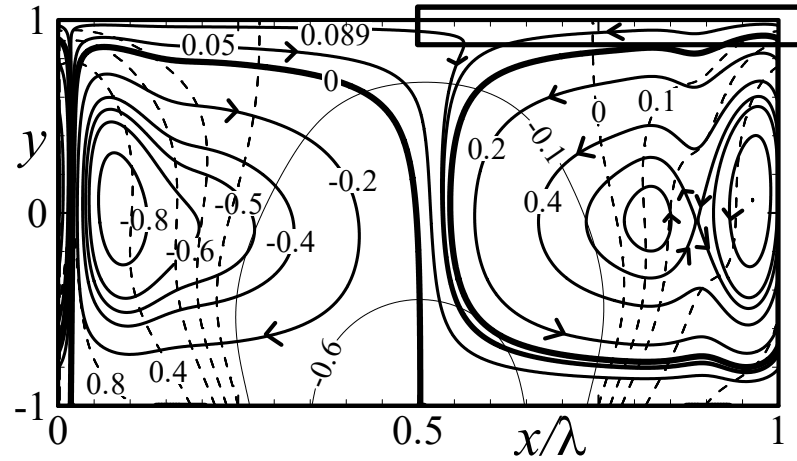
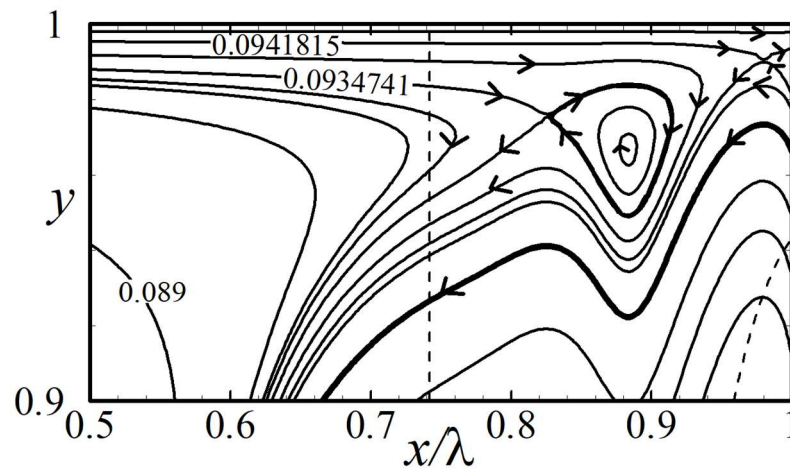


**Figure 4-8:** Variations of change of the flow rate driven by movement of the upper plate  $\Delta Q/Re$  as a function of  $\alpha$  for  $Pr = 0.71$ ,  $Ra_{uni} = 0$ ,  $Re = 1$  (solid lines) and  $Re = 10$  (dashed lines). Thin dotted lines identify asymptotes. Dashed-dotted line identifies the negative values of  $\Delta Q$  for  $Ra_p = 2000$ ,  $Re = 1$ .



(A)

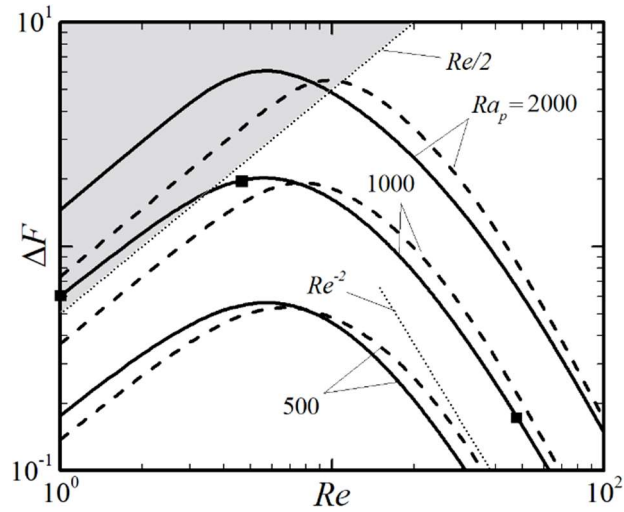


(B)

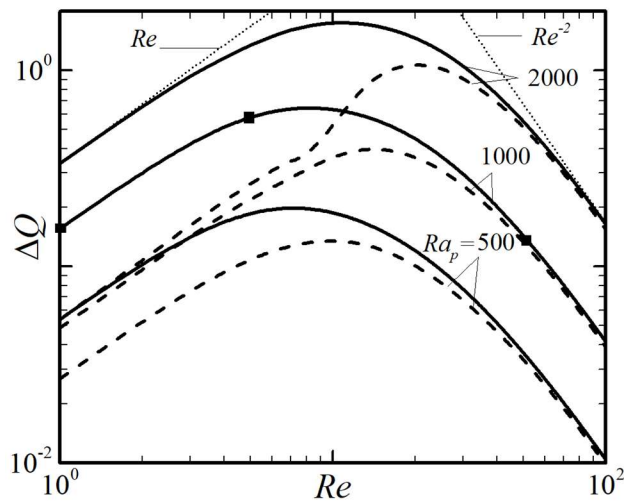
**Figure 4-9:** The flow and temperature fields for  $Ra_p = 2000$ ,  $Pr = 0.71$ ,  $Ra_{uni} = 0$ ,  $Re = 1$ ,  $\alpha = 0.25$ . Enlargement of the box in Figure 4-9A is displayed in Figure 4-9B. Thick solid lines identify streamlines, thin solid lines identify negative isotherms while thin dashed lines identify positive isotherms. Thick streamlines mark borders of various bubbles trapping the fluid.

The force-reducing effect is a strong function of  $Re$  (see Figure 4-10A). The magnitude of  $\Delta F$  increases proportionally to  $Re$  for small  $Re$ 's, reaches a maximum at  $Re \sim 5-6$  and then decreases at a rate proportional to  $Re^{-2}$ . The flow topologies displayed in Figure 4-2 show that the elimination of  $\Delta F$  is associated with the reduction of convection bubbles and confinement of convection effects to a thin boundary layer near the lower plate. Variations

of the flow rate follow a similar pattern (see Figure 4-10B), i.e.  $\Delta Q$  increases at first proportionally to  $Re$ , reaches a maximum at  $Re \sim 5-6$  and then decreases at a rate proportional to  $Re^{-2}$ .



(A)



(B)

**Figure 4-10:** Variations of (A)  $\Delta F$  and (B)  $\Delta Q$  as functions of  $Re$  for  $Pr = 0.71$ ,  $Ra_{uni} = 0$ ,  $\alpha = 2$  (solid lines) and  $\alpha = 1$  (dashed lines). Thin dotted lines identify asymptotes. Plots of flow and temperature field for conditions identified using squares are displayed in Figure 4-2. See text for other details. The shaded area in Figure 4-10A identifies conditions where the driving force must change direction and becomes a braking force.



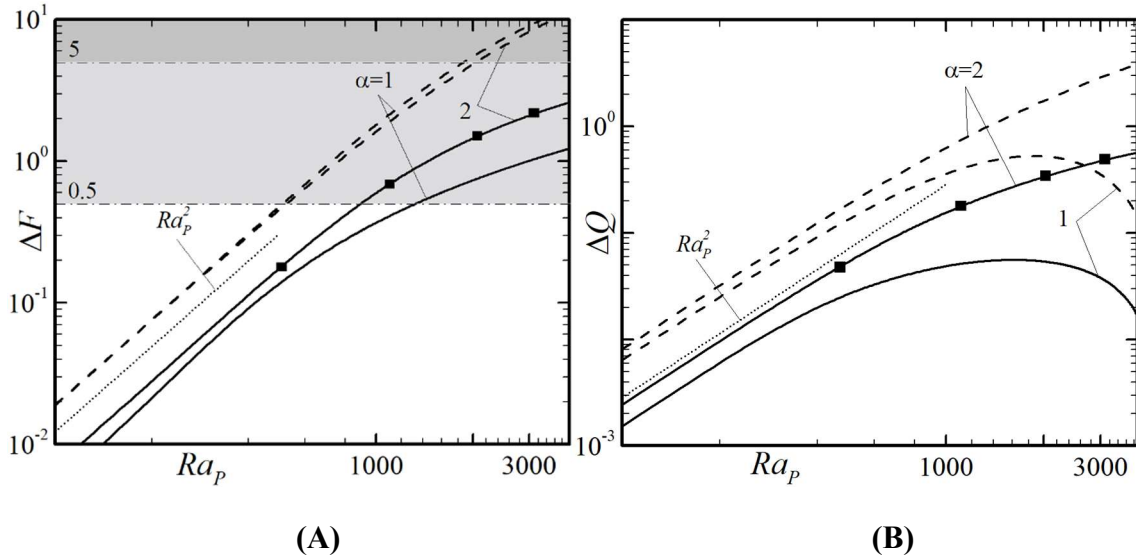
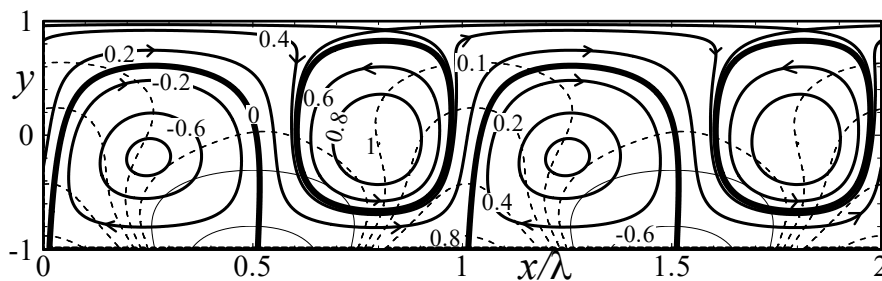


**Figure 4-11:** Variations of (A)  $\Delta F$  and (B)  $\Delta Q$  as functions of  $Ra_p$  for  $Pr = 0.71$ ,  $Ra_{umi} = 0$ ,  $Re = 1$  (solid lines) and  $Re = 10$  (dashed lines). Plots of flow and temperature fields for conditions identified using squares are displayed in Figure 4-12. See text for other details. The shaded area identifies conditions where the driving force must change direction and becomes a braking force when  $Re = 1$  and the double shaded area identifies such conditions for  $Re = 10$ .

Change in driving force  $\Delta F$  is a stronger function of  $Ra_p$  than of  $Re$  as it increases proportionally to  $Ra_p^2$  (see Figure 4-11A). A saturation develops for large enough  $Ra_p$  slowing down this growth. The saturation starts at a smaller  $Ra_p$  when  $Re$  is smaller. Flow topologies displayed in Figure 4-12 show expansion of the rolls and reduction of the size of the stream tube with an increase in  $Ra_p$ . The amount of fluid driven by the plate increases with  $Ra_p$  but the development of complex flow topologies (not shown) reduces this flow for a range of small  $\alpha$ 's (see Figure 4-11B).



(A)

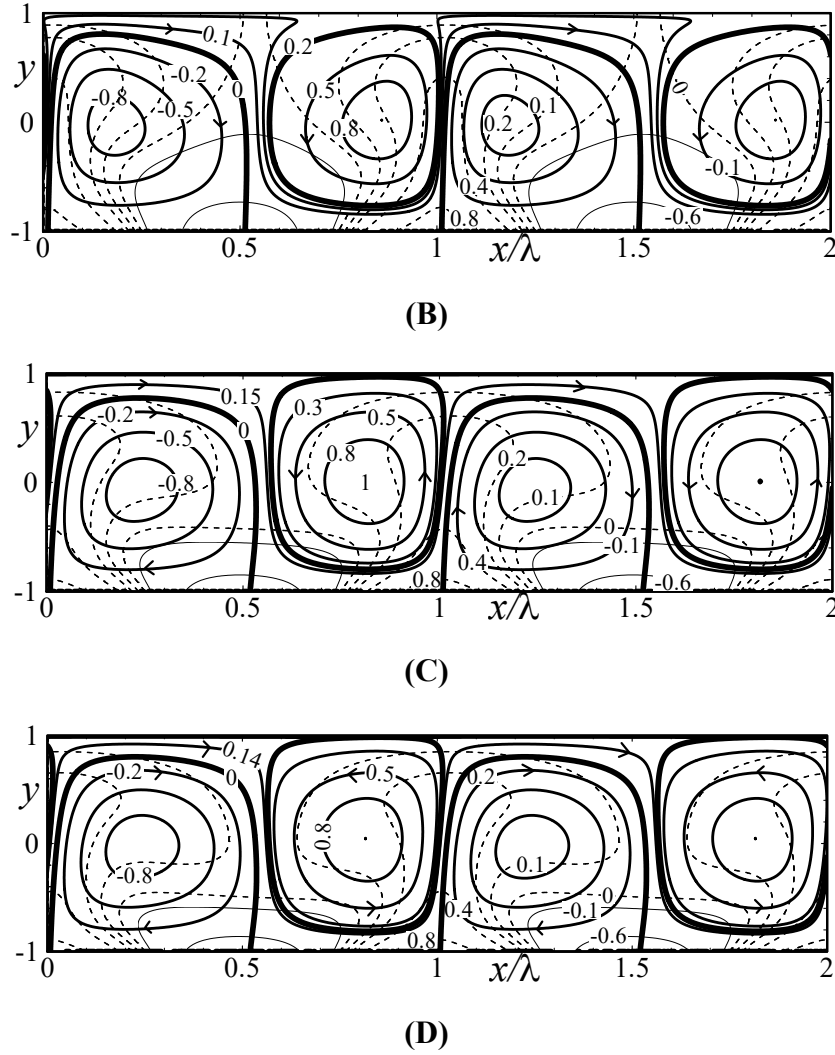


**Figure 4-12:** The flow and temperature fields for  $Re = 1$ ,  $Pr = 0.71$ ,  $Ra_{uni} = 0$ ,  $\alpha = 2$  at (A)  $Ra_p = 500$ , (B)  $Ra_p = 1000$ , (C)  $Ra_p = 2000$  and (D)  $Ra_p = 3000$ . Thick solid lines identify streamlines, thin solid lines identify negative isotherms while thin dashed lines identify positive isotherms. Thick streamlines mark borders of various bubbles trapping the fluid. Flow conditions used in these plots are marked in Figure 4-11 using squares.

Analyzing (2.11) shows that the external force required to drive the upper plate decreases to zero when  $\Delta F = Re/2$ . Such conditions can be easily achieved and correspond to the grey shading in Figure 4-6. When  $\Delta F > Re/2$ , the heating-induced effects are strong enough so that the external force must change direction and act as a brake to prevent the plate from accelerating. This shows that the system becomes meta-stable when exposed to

a periodic heating. Consider a stationary upper plate without any external forces acting on it and apply heating to the lower plate. The convection-induced forces increase with  $Ra_p$  (see Figure 4-11A) but the system remains at rest due to its periodicity and  $x$ -symmetry. The addition of any disturbance which breaks the symmetry will not generate plate motion if the heating is too weak as an external force is required to support such motion. For strong enough heating, disturbances will generate plate motion as the buoyancy forces can overcome friction. As the plate accelerates ( $Re$  increases), the buoyancy forces decrease (see Figure 4-10A) until a state of equilibrium is reached where the increasing friction balances the decreasing driving force. The upper plate may move in either horizontal direction depending on the form of the initial disturbance. This mechanism can be used to move a free-floating body by simply heating one of the plates.

## 4.2 Plates with unequal mean temperatures

As it is unlikely that the mean temperatures of both plates can be kept identical in practical applications, it is of interest to determine how their difference may affect the system response. This difference is expressed in the analysis as the uniform Rayleigh number  $Ra_{uni}$  whose positive (negative) values correspond to the lower plate being hotter (cooler). The results displayed in Figure 4-13 demonstrate that the uniform heating increases  $\Delta F$  while cooling decreases it, and the change is approximately linear with  $Ra_{uni}$ . The type of variations as a function of  $\alpha$  remains nearly identical for larger  $Re$ 's (see  $Re = 10$  in Figure 4-13) for all  $Ra_{uni}$ 's considered with an upward shift resulting from the increase of  $Ra_{uni}$ , and with the most effective  $\alpha$  nearly unchanged. A shift from  $Ra_{uni} = -150$  to  $Ra_{uni} = 150$  increases  $\Delta F$  by a factor of  $\sim 20$  when  $Re = 10$ , but this is insufficient to change the direction of the driving force. In the case of smaller  $Re$ 's ( $Re = 1$  in Figure 4-13), the most effective  $\alpha$  shifts from  $\alpha = 1.6$  to  $\alpha = 2.5$ ,  $\Delta F$  approximately quadruples when  $Ra_{uni}$  changes in the same range, and this is sufficient to change the direction of the driving force. Variations of the flow rate  $\Delta Q$  follow the same pattern as variations of  $\Delta F$  and have similar magnitudes regardless of  $Re$  (see Figure 4-14).

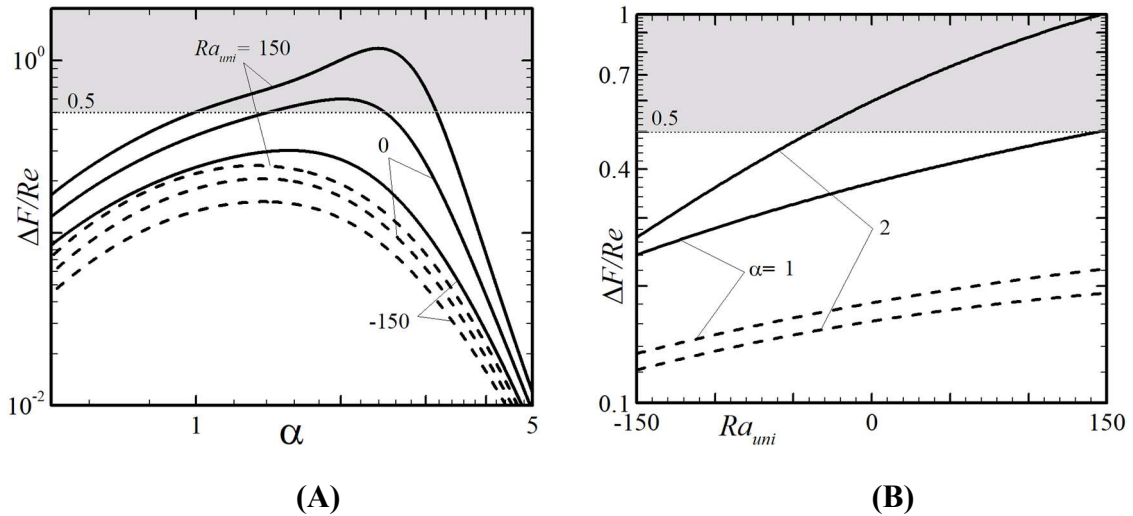


**Figure 4-13:** Variations of  $\Delta F/Re$  as a function of (A)  $\alpha$  and (B)  $Ra_{uni}$  for  $Re = 1$  (solid lines) and  $Re = 10$  (dashed lines), and  $Ra_p = 1000$ ,  $Pr = 0.71$ . The shaded area identifies conditions where the driving force changes direction and becomes a braking force.

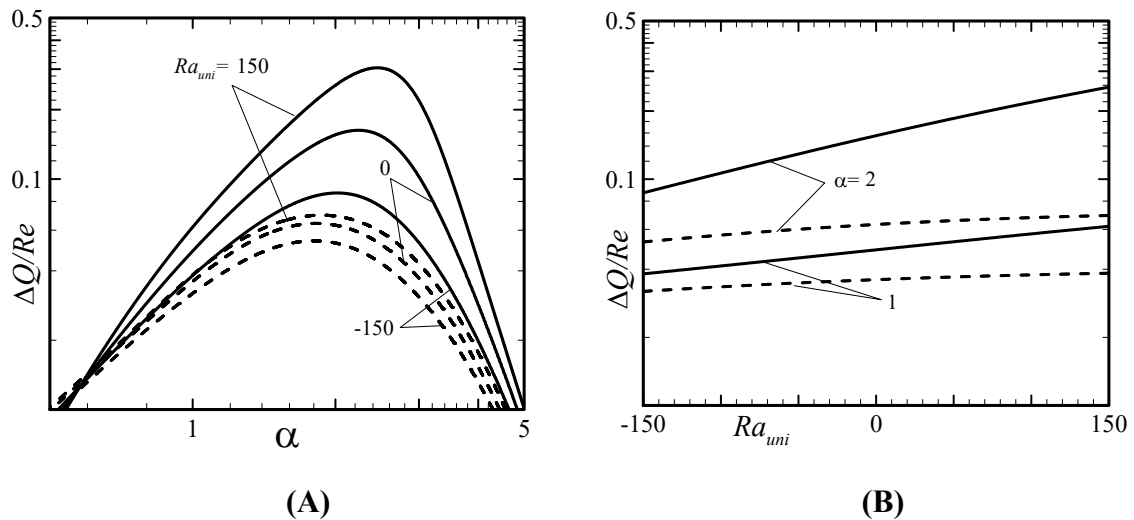


**Figure 4-14:** Variations of  $\Delta Q/Re$  as a function of (A)  $\alpha$  and (B)  $Ra_{uni}$  for  $Re = 1$  (solid lines) and  $Re = 10$  (dashed lines), and  $Ra_p = 1000$ ,  $Pr = 0.71$ .

### 4.3 Effects of the Prandtl number

The Prandtl number describes transport properties with conductive effects expected to play a larger role in the small- $Pr$  fluids. The spatial temperature variations will be stronger and

less affected by convection in such fluids, leading to larger changes of  $\Delta F$ . The results displayed in Figure 4-15A demonstrate a nearly three-orders of the magnitude increase of  $\Delta F$  resulting from replacing fluids with  $Pr = 10$  with fluids with  $Pr = 0.1$ , changing  $\Delta F$  from being insufficient to change the direction of the driving force at large  $Pr$ 's to being more than sufficient at small  $Pr$ 's. The increase of the flow rate follows the same pattern as documented in Figure 4-15B. The character of the changes in  $\Delta F$  and  $\Delta Q$  as functions of  $\alpha$  remains qualitatively similar for all  $Pr$ 's with the relevant curves just shifted upwards for smaller  $Pr$ 's as illustrated in Figure 4-16.

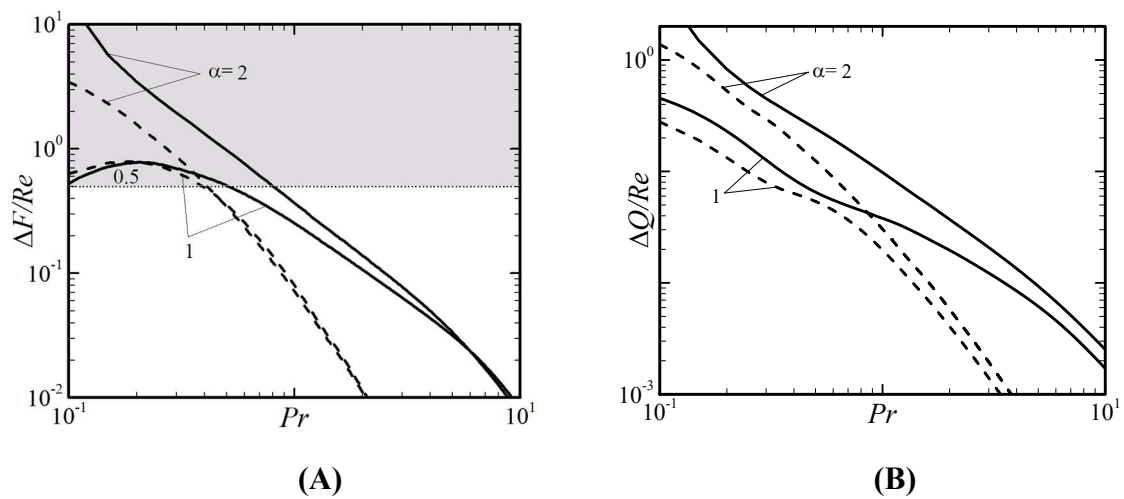


**Figure 4-15:** Variations of (A)  $\Delta F/Re$  and (B)  $\Delta Q/Re$  as functions of  $Pr$  at  $Re = 1$  (solid lines) and  $Re = 10$  (dashed lines) for  $Ra_p = 1000$ ,  $Ra_{uni} = 0$ .

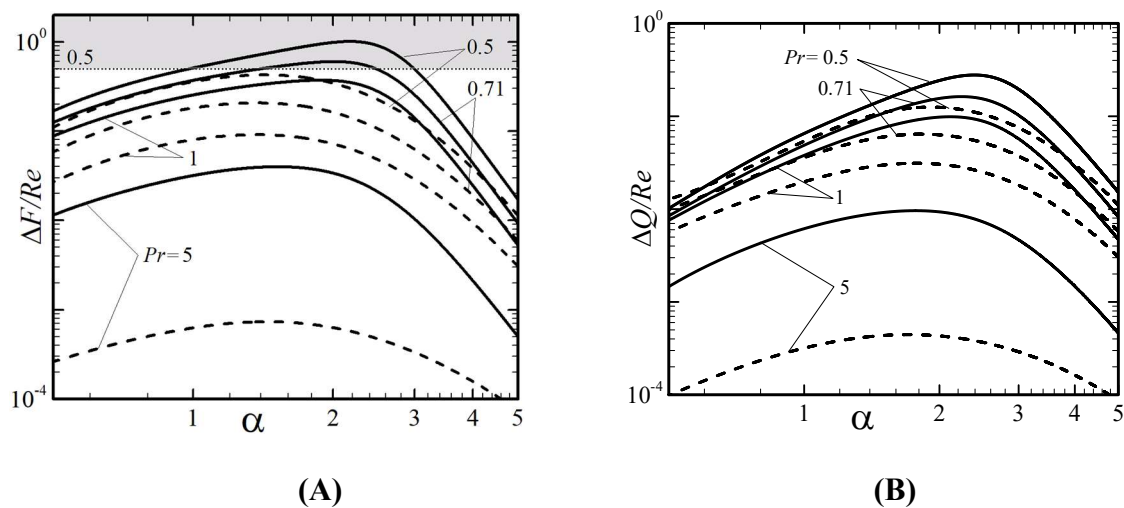
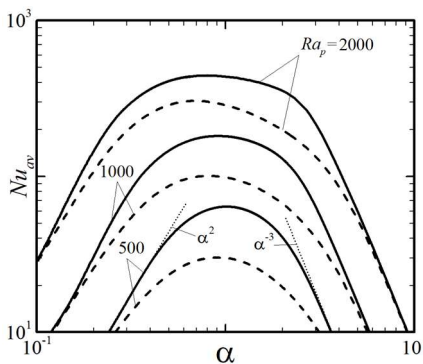


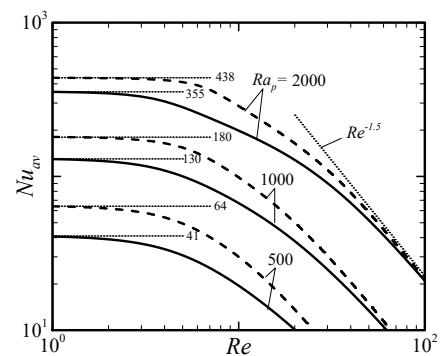
**Figure 4-16:** Variations of (A)  $\Delta F/Re$  and (B)  $\Delta Q/Re$  as functions of  $\alpha$  at  $Re = 1$  (solid lines) and  $Re = 10$  (dashed lines) for  $Ra_p = 1000$ ,  $Ra_{uni} = 0$ .

## 4.4 Heat transfer effects

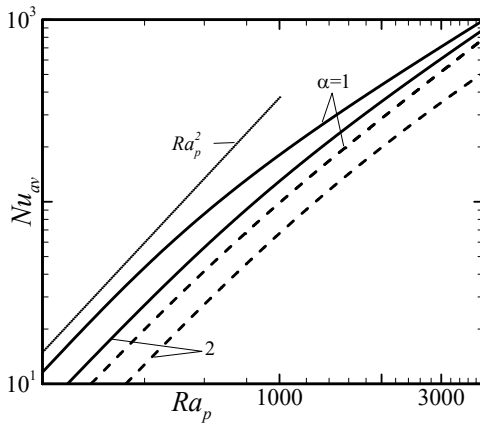
The temperature differences between and along the plates lead to the formation of vertical and horizontal heat fluxes. The former one is of interest as the heat flow between the plates can be viewed as a potential energy cost associated with the use of heating to reduce the driving force. This heat flux can be created only by convection in the case of a purely periodic heating. Variations of the corresponding mean Nusselt number  $Nu_{av}$  displayed in Figure 4-17A demonstrate that  $Nu_{av}$  is a strong function of  $\alpha$  and reaches a maximum at  $\alpha \approx 0.8 - 1$ , which is smaller than the  $\alpha$  required to maximize  $\Delta F$ . The use of an excessively small  $\alpha$  reduces  $Nu_{av}$  at a rate proportional to  $\alpha^2$ , which is much slower than the reduction of  $\Delta F$ . The use of an excessively large  $\alpha$  reduces  $Nu_{av}$  at a rate proportional to  $\alpha^{-3}$ , which is also much slower than the reduction of  $\Delta F$ . The maximal  $Nu_{av}$  occurs at  $Re = 0$  with an increase in  $Re$  reducing  $Nu_{av}$  (see Figure 4-17B) through the elimination of convective effects (see Figure 4-10). An increase in  $Ra_p$  results in an increase in  $Nu_{av}$  proportional to  $Ra_p^2$ , which is the same as the rate of increase of  $\Delta F$ , with a very slight reduction of this growth due to saturation effects in the upper range of  $Ra_p$ 's considered in this study (Figure 4-17C). The addition of a uniform heating component leads to a change in the heat flow due to both changes in the intensity of convection as well as the addition of a conductive flux.  $Nu_{av}$  increases when the lower plate is heated and decreases when it is cooled, varying in a qualitatively similar manner as a function of  $\alpha$  for all  $Re$ 's of interest with the relevant curves shifted upwards as  $Ra_{uni}$  increases (see Figure 4-18A). The increase is nearly linear in the range of  $Ra_{uni}$  of interest with the rate of change being a strong function of  $\alpha$  (see Figure 4-18B).



(A)

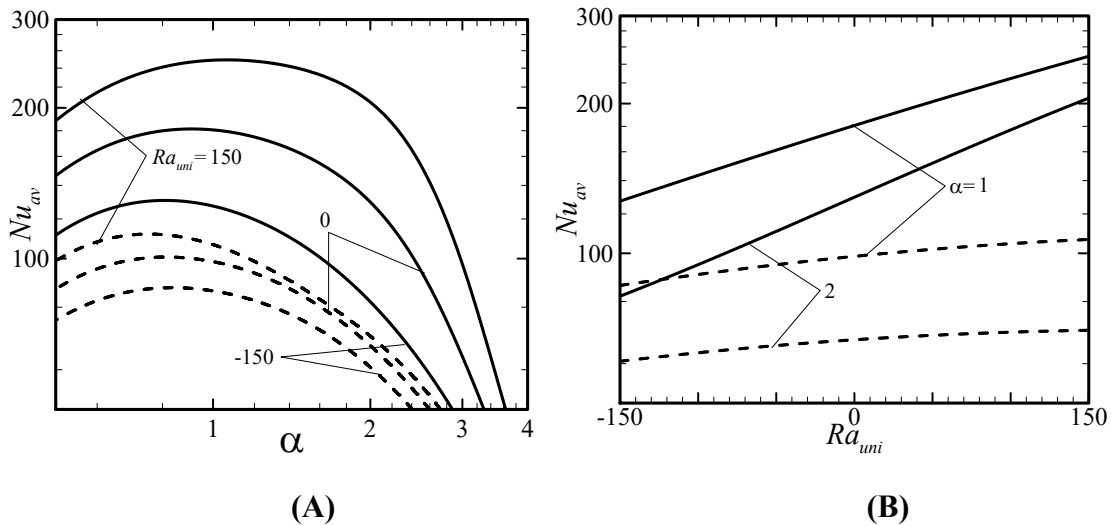


(B)



(C)

**Figure 4-17:** Variations of  $Nu_{av}$  in (A) as a function of  $\alpha$  for  $Re = 1$  (solid lines) and  $Re = 10$  (dashed lines), in (B) as a function of  $Re$  for  $\alpha = 1$  (dashed lines) and  $\alpha = 2$  (solid lines), and in (C) as a function of  $Ra_p$  for  $Re = 1$  (solid lines) and  $Re = 10$  (dashed lines), for  $Pr = 0.71$ ,  $Ra_{uni} = 0$ . Thin dotted lines identify asymptotes.



(A)

(B)

**Figure 4-18:** Variations of  $Nu_{av}$  as a function of (A)  $\alpha$  and (B)  $Ra_{uni}$  for  $Re = 1$  (solid lines) and  $Re = 10$  (dashed lines) for  $Ra_p = 1000$ ,  $Pr = 0.71$ .

Changes in the heat flow due to a change of the type of fluid being used are illustrated in Figure 4-19 for purely periodic heating. When  $Re$  is small and buoyancy-driven effects dominate, an increase in  $Pr$  reduces  $Nu_{av}$  in a qualitatively similar manner for all  $\alpha$ 's (see

results for  $Re = 1$  in Figure 4-19A) with an asymptote developing for small  $Pr$  (see Figure 4-19B). An increase in  $Re$  weakens convective effects and results in a significant reduction of  $Nu_{av}$  associated with an increase in  $Pr$  (see results in Figure 4-19 for  $Re = 10$ ). This reduction depends on  $\alpha$  and a decrease in  $Pr$  may either increase or decrease the heat flux depending on the  $\alpha$  being used.

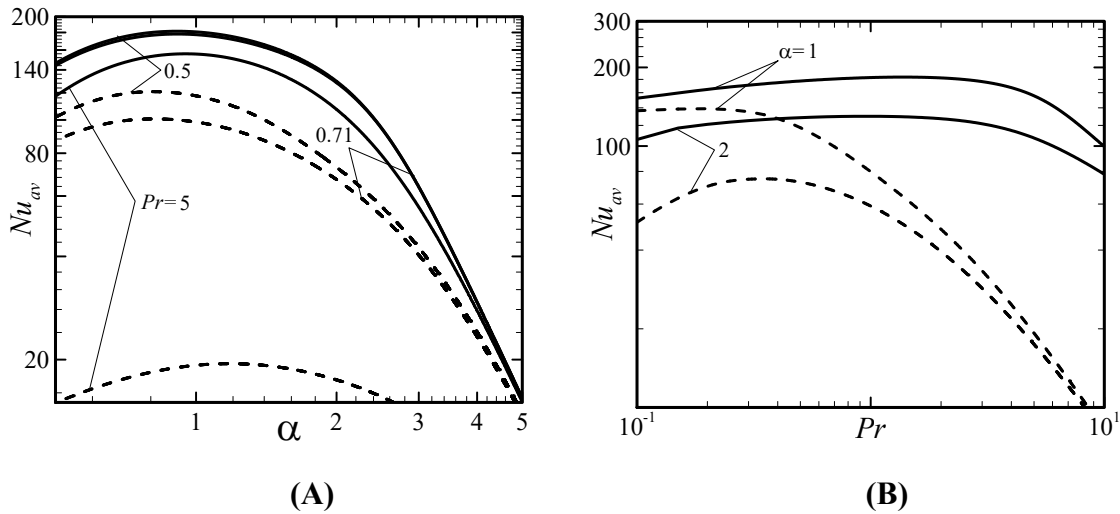


**Figure 4-19:** Variations of  $Nu_{av}$  in (A) as a function of  $\alpha$  and in (B) as a function of  $Pr$  for  $Re = 1$  (solid lines) and  $Re = 10$  (dashed lines) for  $Ra_p = 1000$ ,  $Ra_{uni} = 0$ .

## 4.5 Heating of the upper plate

Similar effects can be achieved by heating the upper stationary plate and imposing motion of the lower plate. The similarity between both systems can be demonstrated by reversing the direction of gravity, i.e.  $Ra_p \rightarrow -Ra_p$ , and changing the sign of the temperature, i.e.  $\theta \rightarrow -\theta$  (Hossain & Floryan, 2014). The latter condition implies a change of the sign of the temperature imposed at the upper plate and results in a shift of the temperature field by a half-cycle in the  $x$ -direction. The up/down “symmetry” between the lower and upper heating is illustrated in Figure 4-20 and this leads to the conclusion that the externally-imposed driving force is the same regardless of which plate is heated.



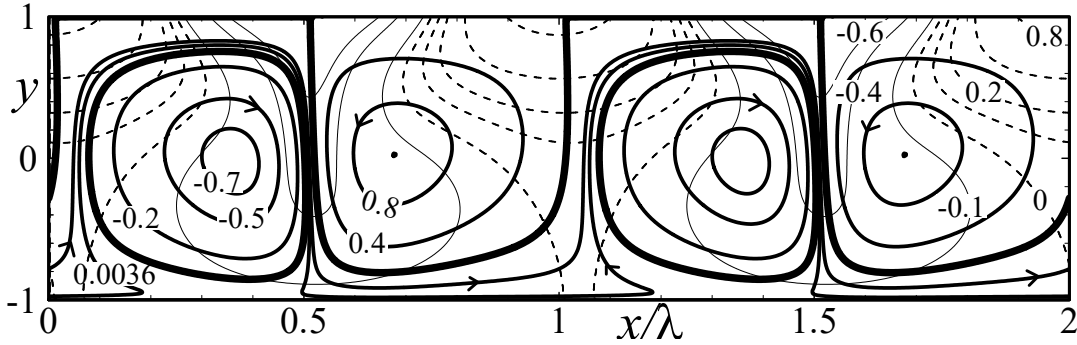


**Figure 4-20:** The flow and temperature fields for the same conditions as in Figure 4-7A but with the upper plate heated and the lower plate moving. Thick solid lines identify streamlines, thin solid lines identify negative isotherms while thin dashed lines identify positive isotherms. Thick streamlines mark borders of bubbles trapping the fluid.

## 4.6 Summary

In this chapter, the two-dimensional flow response due to the presence of a spatially periodic heating applied at lower plate with the upper plate moving has been discussed. An external force is required to generate the motion on the upper plate and the rate of this motion is expressed in terms of the Reynolds number  $Re$ . Heating that results in the lower plate temperature varying sinusoidally in the horizontal direction, with its amplitude expressed in terms of a periodic Rayleigh number  $Ra_p$  and the spatial distribution described by the wavenumber  $\alpha$ , has been considered. The analysis has been limited to  $Ra_p < 3000$  to avoid the formation of secondary flows. The difference between the mean temperatures of the plates is expressed in terms of the uniform Rayleigh number  $Ra_{uni}$  with positive values corresponding to a warmer lower plate. The fluid motion results from a competition between the buoyancy-driven effects and the plate-driven movement. The former has the form of counter-rotating rolls whose distribution is dictated by the heating pattern. The latter adds a rectilinear motion which leads to the reduction and eventual elimination of the rolls when  $Re$  is large enough.

It has been shown that periodic heating always reduces the driving force, regardless of whether the heating is applied to the lower or upper plate, but the magnitude of this reduction is a strong function of the heating wavenumber. The largest reduction is achieved

for  $\alpha = 1-2$  with a rapid decrease of this effect when either too small or too large  $\alpha$ 's are used. An increase in  $Ra_{uni}$  and decrease in the Prandtl number  $Pr$  magnify this effect. An increase in  $Re$  eliminates the rolls and reduces this effect, leading to its practical elimination for  $Re > 30-50$  depending on the heating intensity. The use of proper heating intensity and distribution results in the complete elimination of the driving force as the plate movement can be supported by the buoyancy effects only. Conditions where an external braking force needs to be used to prevent the plate from accelerating have also been identified.

## Chapter 5

### 5 Flow between grooved isothermal plates in relative motion

This chapter presents discussion of the system response when the lower plate is isothermal and grooved, and its mean temperature is the same as the temperature of the upper plate. The sketch of the flow system is shown in Figure 5-1. The knowledge of the effects of grooves on the pressure-gradient-driven flows is more advanced, including identification of the form of the drag-reducing grooves, their shape optimization for maximization of drag reduction, and the development of reduced geometry models for extraction of hydrodynamics information regardless of the groove geometry (Mohammadi & Floryan, 2012, 2013a, 2013b). The objective of this chapter is to use concepts developed in the context of pressure-gradient-driven flows and apply them in the systematic analysis of flows between two moving surfaces with the focus on the determination of driving forces required to maintain such movement and demonstration of how these forces are affected by the grooves. The analysis is limited to small Reynolds numbers corresponding to conditions found in lubrication problems and small groove amplitudes. Section 5.1 gives a brief description of the flow geometry. Section 5.2 discusses evaluation of the driving force. Section 5.3 discusses the effects of sinusoidal grooves. Section 5.4 generalizes results to grooves of arbitrary shapes and Section 5.5 provides a short summary of the main conclusions.

#### 5.1 Flow geometry

Replace the lower smooth plate with a grooved plate with the system geometry described as (see Figure 5-1)

$$y_L(x) = -1 + \sum_{n=-N_A}^{n=+N_A} H^{(n)} e^{inax}, \quad (5.1a)$$

$$y_U(x) = 1. \quad (5.1b)$$

where the subscripts  $L$  and  $U$  refer to the lower and upper plates, respectively,  $H^{(n)}$ 's are coefficients of the Fourier expansion describing groove shape,  $\lambda = 2\pi/\alpha$  is the wavelength of the basic groove module,  $\alpha$  is the corresponding wavenumber and  $N_A$  is the number of Fourier modes required to describe groove geometry. Relation (5.1a) must satisfy the reality condition with  $H_L^{(n)}$  being the complex conjugate of  $H_L^{(-n)}$ . It is assumed that grooves do not affect the mean distance between the plates, i.e.  $H_L^{(0)} = 0$ , and that the extremities of the grooves are located at  $-1 + y_b$  and  $-1 - y_b$  (see Figure 5-1). Change of the mean distance can be accommodated analytically (Mohammadi & Floryan, 2013b) and, therefore, analysis of its effects is of no interest in this investigation.

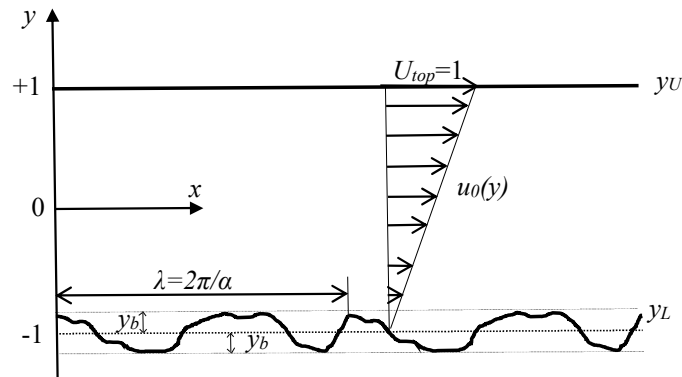


**Figure 5-1:** Schematic diagram of the flow system.

## 5.2 Driving force applied to the moving plate

The presence of the grooves changes the shear stress acting on the upper plate which can be calculated as

$$\Delta\tau = -\left.\frac{du}{dy}\right|_{y=1} + \frac{1}{2}Re. \quad (5.2)$$

The change in the driving force due to the introduction of the grooves is determined as

$$\Delta F = Re \left( Re^{-1} \lambda^{-1} \int_0^\lambda \left.\frac{\partial u}{\partial y}\right|_{y=1} dx - \frac{1}{2} \right). \quad (5.3)$$

A secondary quantity of interest is the change in the fluid volume pulled by the plate and can be calculated as

$$\Delta Q = Re \left[ 1 - Re^{-1} \left( \int_{y_L(x)}^1 u(x, y) dy \right) \Big|_{mean} \right]. \quad (5.4)$$

### 5.3 Sinusoidal grooves

We shall begin discussion by assuming that the groove geometry is described by just a single Fourier mode in (5.1), i.e.  $H^{(n)}$  are zero except  $H^{(1)} = H^{(-1)} = 0.5y_b$  (sinusoidal grooves). There are two characteristic elements of flow response, as illustrated in Figure 5-2. The first one involves streamwise spatial modulations and occurs for all groove wavenumbers. The second one occurs only for large enough  $\alpha$ 's where the groove sidewalls come close together, causing the stream lift-up and an effective narrowing of the flow cross-sectional area, with the streamwise modulations being confined to a part of the flow adjacent to the grooved plate (see Figure 5-2C). Modulations result in the flow acceleration around the groove peaks and deceleration around the groove troughs as dictated by the changes in the flow cross-sectional area. The resulting shear stress variations at the upper plate are illustrated in Figure 5-3 which displays the difference  $\Delta\tau_U$  between the actual shear stress and the shear stress for the smooth plates. The stress decreases below the reference level above the groove troughs and increases above the peaks. The changes of  $\Delta\tau_U/Re$  are fairly small compared to the reference value of  $-1/2$  and their mean values are negative, suggesting a force increase.

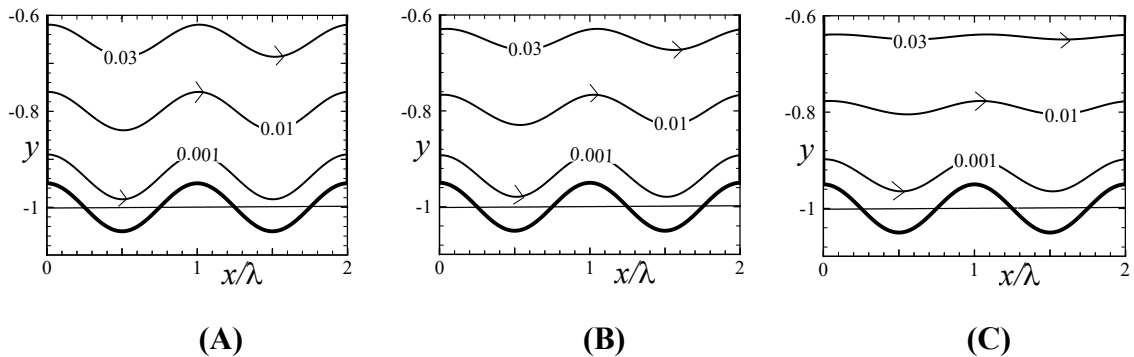


**Figure 5-2:** Examples of typical flow fields for sinusoidal grooves at the lower plate and smooth upper plate for  $Re = 100$ ,  $y_b = 0.05$ . From left to right  $\alpha = 0.1, 1, 5$ .

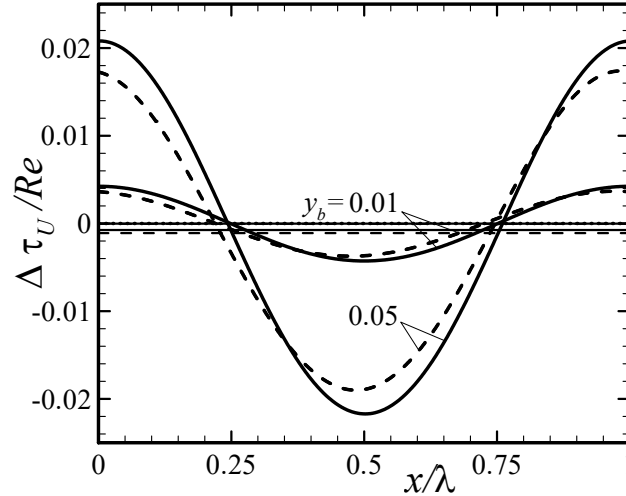


**Figure 5-3:** Variations of the difference  $\Delta\tau_U/Re$  between the shear stresses acting on the upper smooth plate with the sinusoidal grooves at the lower plate for  $\alpha = 1$ ,  $Re = 1$  (solid lines) and  $Re = 100$  (dashed lines). The mean values  $\Delta\tau_{U,mean}$  are marked using thin lines.

Analysis of different spatial distributions of grooves shows that the driving force always increases regardless of  $\alpha$  as illustrated in Figure 5-4A. The increase is rather small and nearly independent of  $\alpha$  for  $\alpha < \sim 1$  with a well-defined limit for  $\alpha \rightarrow 0$ . It is caused by spatial flow modulations such as those illustrated in Figure 5-2. The force rapidly increases as  $\alpha$  increases beyond  $\alpha \approx 1$ . This effect is associated with the stream lift-up as the short wavelength grooves reduce the effective flow cross-sectional area. The upper limit on  $\Delta F$  can be easily estimated by noting that the opening between the plates in the limit of  $\alpha \rightarrow \infty$  decreases to  $2 - y_b$  which leads to the force increase of  $\Delta F = y_b/[2(2 - y_b)]$ . The same observation applies to the reduction of the amount of fluid being pulled by the plate movement. The flow rate changes marginally with  $\alpha$  for  $\alpha < \sim 1$ , and it decreases rapidly as  $\alpha$  increases above  $\alpha \approx 1$ . The flow reduction is caused by a decrease of the effective conduit opening and its upper bound can be determined through an analysis similar to that used to determine the upper bound on the driving force resulting in  $\Delta Q = (y_b^2 + y_b - 1)/[2(1 - y_b)]$ .

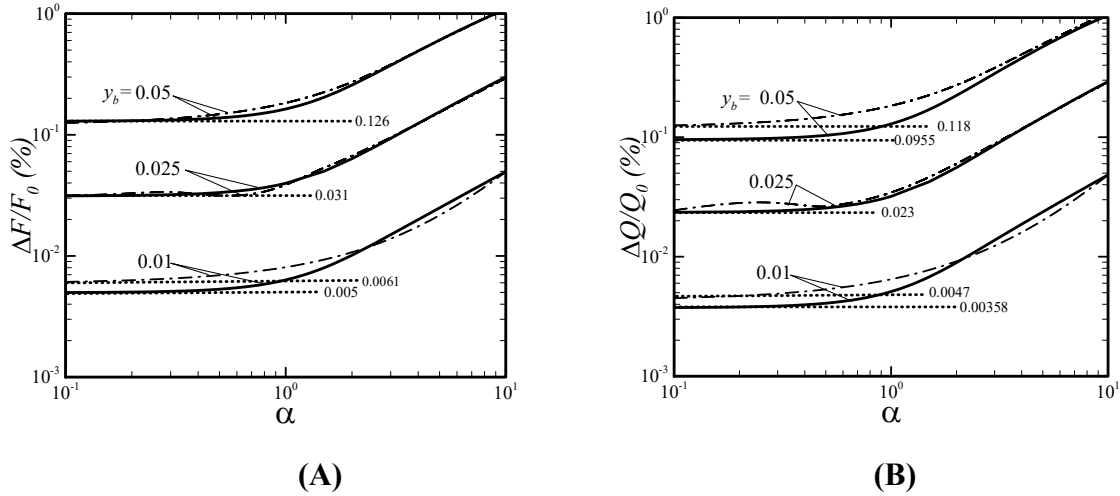


**Figure 5-4:** Variations of (A)  $\Delta F/F_0$  and (B)  $\Delta Q/Q_0$  as functions of  $\alpha$  for  $Re = 1$  (solid lines) and 100 (dashed-dotted lines). Dotted lines identify asymptotes for  $\alpha \rightarrow 0$ . The upper plate is smooth while the lower plate has sinusoidal grooves.

Results displayed in Figure 5-5A demonstrate that the increase of the driving force is proportional to  $y_b^2$ . This increase is the same for  $\alpha$ 's for which the stream lift-up does not occur, and it remains rather small in the range of  $y_b$ 's considered, i.e. it is of the order of 1% of the reference value for  $y_b=0(10^{-1})$ . The amount of fluid being pulled by the plate decreases at the same rate, as shown in Figure 5-5B, and this decrease is also rather small. The reader may note that force increase for large  $\alpha$ 's is dominated by effects associated with the effective narrowing of the plates' spacing.

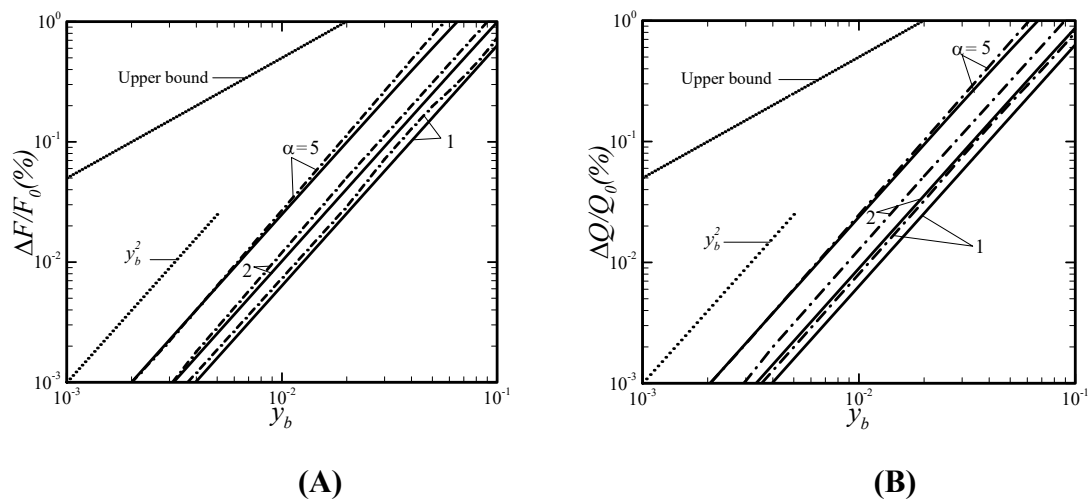


**Figure 5-5:** Variations of (A)  $\Delta F/F_0$  and (B)  $\Delta Q/Q_0$  as functions of  $y_b$  for  $Re = 1$  (solid lines) and 100 (dashed-dotted lines). Thin dotted lines identify asymptotes and the upper bounds. The upper plate is smooth while the lower plate has sinusoidal grooves.

The force reduction is proportional to  $Re$  for small  $Re$ 's as illustrated in Figure 5-6. The rate of its increase increases for  $Re > \sim 20$  due to increasing importance of nonlinear effects. Reduction of the induced flow rate follows the same pattern, as illustrated in Figure 5-6B.

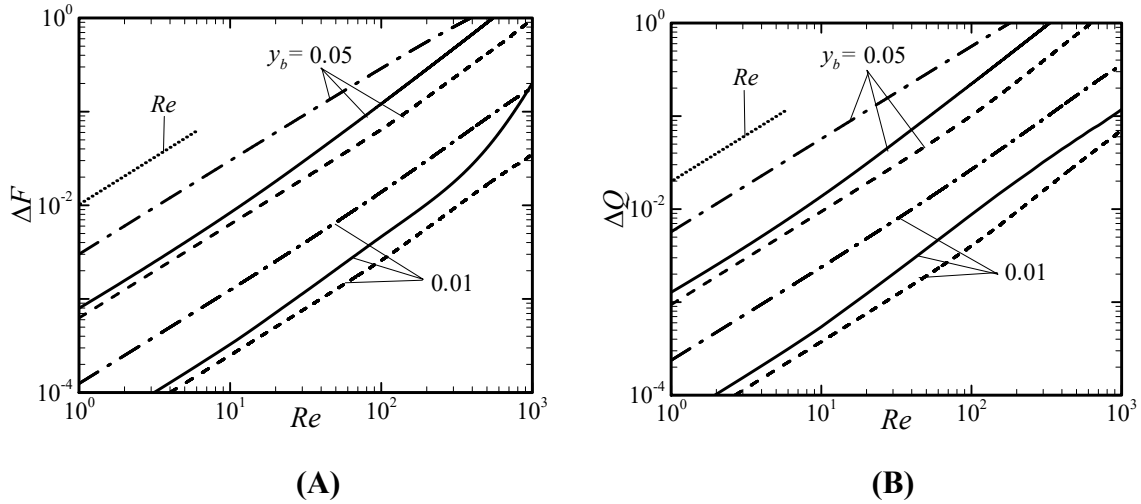


**Figure 5-6:** Variations of (A)  $\Delta F$  and (B)  $\Delta Q$  as functions of  $Re$  for  $\alpha = 0.1$  (dashed lines),  $\alpha = 1$  (solid lines), and  $\alpha = 5$  (dashed-dotted lines). The upper plate is smooth while the lower plate has sinusoidal grooves.

## 5.4 Arbitrary grooves

We shall now look at grooves of arbitrary shape. As there is an uncountable number of such grooves, the symmetric triangular, symmetric trapezoidal, rectangular, triangular tilted upstream, triangular tilted downstream, bulged-shaped and asymmetric trapezoidal grooves illustrated in Figure 5-7 and referred to as grooves B - H, respectively, were selected for analysis. To make meaningful comparisons, all grooves have the same wavelength and the same amplitude. Their performance is compared with the sinusoidal grooves referred to as grooves A.



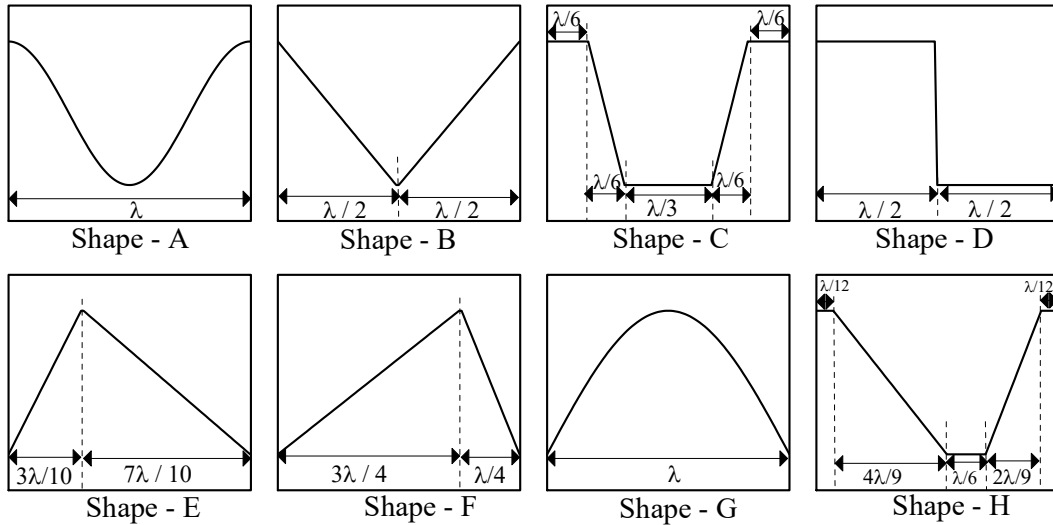


**Figure 5-7:** Geometry of grooves used in the present study.

Results presented in Figure 5-8 demonstrate that up to five Fourier modes need to be used to accurately determine forces for grooves B, C, E-H but many more modes need to be used for grooves D. The difficulties in the latter case are associated with the so-called Gibbs phenomenon (Gibbs, 1898, 1899) as Fourier representations of functions with infinite derivatives have very slow rates of convergence. The convergence can be improved, as discussed in (Gottlieb & Shu, 1997; Rim & Yun, 2013), but these procedures have not been implemented in the present study.

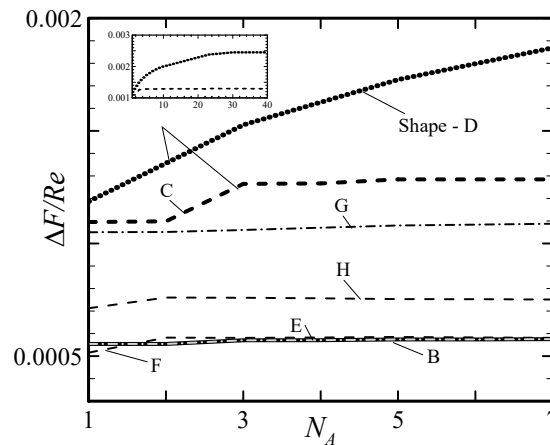
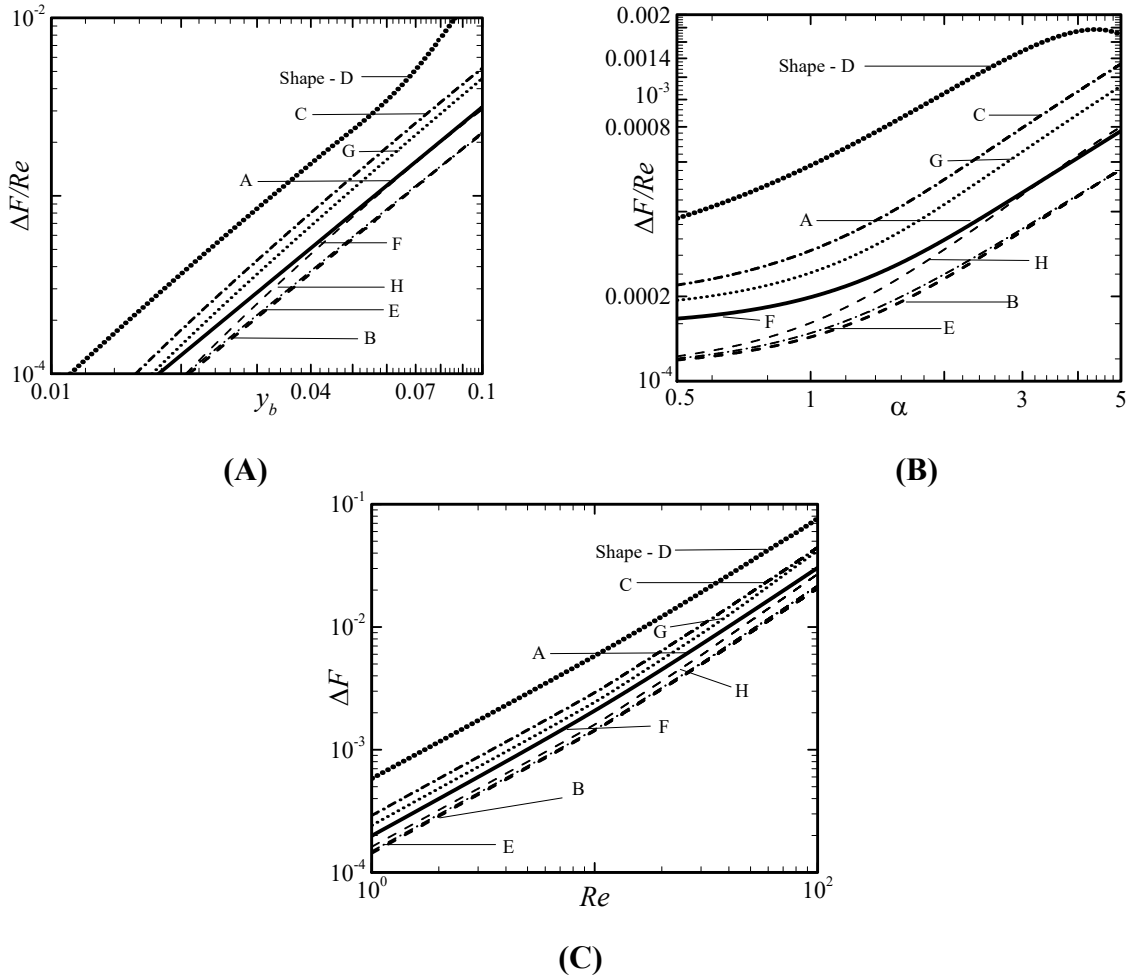


**Figure 5-8:** Variations of  $\Delta F/Re$  as a function of the number of Fourier modes used for geometry representation for  $Re = 1$ ,  $y_b = 0.05$ ,  $\alpha = 1$ .

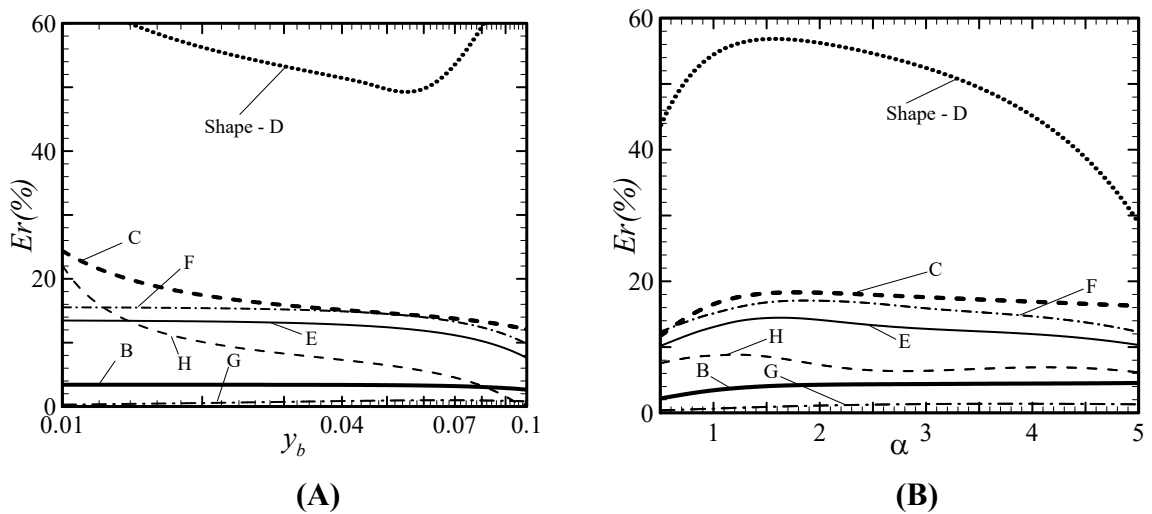
Results displayed in Figure 5-9 demonstrate that the driving force correction varies in a very similar manner as a function of  $y_b$ ,  $\alpha$  and  $Re$  for all grooves in the range of parameters of interest in this study. This leads to a conclusion that the system response is qualitatively similar regardless of the groove geometry. This similarity leads to the reduced geometry model with the groove geometry being represented by the leading Fourier mode of its Fourier expansion. The error  $Er$  of this procedure is defined as

$$Er = \frac{\Delta F_{mode1} - \Delta F_{actual}}{\Delta F_{actual}}. \quad (5.5)$$

where  $\Delta F_{actual}$  stands for the actual force change while  $\Delta F_{mode1}$  stands for the force change determined by approximating the groove shape using the first Fourier mode of its Fourier expansion. Results displayed in Figure 5-10 demonstrate that the error of this procedure is less than 20% except for shapes whose Fourier expansions are affected by the Gibbs phenomenon where the error increase up to 50% (see results for groove D). If 20% error is acceptable then data presented in Section 5.3 represents a general solution. The determination of forces created by a selected groove distribution should start with the determination of the leading mode of its Fourier representation and extracting information about the forces from the results presented in Section 5.3. The error of this procedure is likely to be acceptable for most applications. If intentional introduction of grooves is of interest, one can select shapes which are easy to manufacture, and the desired performance will be achieved by matching their leading Fourier modes with the one which is able to deliver this performance according to the results discussed in this section. While the Gibbs phenomenon limits the applicability of this procedure, it nevertheless delivers an order of magnitude determination of forces which could still be of interest in the design process, e.g. performance of rectangular grooves (shape D in Figure 5-7). One can obviously improve accuracy by incorporating more Fourier modes for geometric description but in this case each groove distribution must be studied separately, and one reverts to the case-by-case studies without the ability to generalize.



**Figure 5-9:** Variations of the force increase  $\Delta F$  for different grooves as functions of (A)  $y_b$  for  $Re = 1, \alpha = 1$ , (B)  $\alpha$  for  $y_b = 0.025, Re = 1$ , (C)  $Re$  for  $y_b = 0.025, \alpha = 1$ .



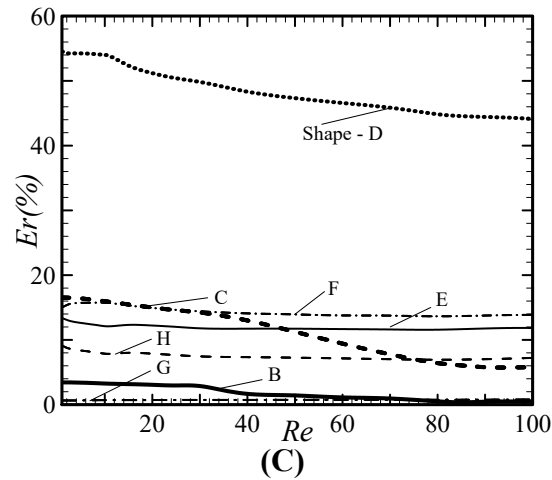


**Figure 5-10:** Variations of the error  $Er$  associated with using the first mode of the Fourier expansion representing each groove shape as a function of (A)  $y_b$  for  $Re = 1$ ,  $\alpha = 1$ , (B)  $\alpha$  for  $y_b = 0.025$ ,  $Re = 1$ , and (C)  $Re$  for  $y_b = 0.025$ ,  $\alpha = 1$ .

## 5.5 Summary

In this chapter, the effects of grooved geometry on the magnitude of force required to maintain the relative movement of parallel plates have been presented. The analysis is limited to the grooves which do not affect the mean conduit opening but are arbitrary otherwise. These grooves are placed at the stationary lower plate and their geometry is described using the appropriate Fourier expansion. The analysis considers different spatial groove distributions, is limited to groove amplitudes of less than 10% of the conduit opening and a Reynolds number of less than 1000.

It has been shown that the force required to maintain the plate movement can be predicted with an acceptable accuracy using the reduced geometry model. In this model, the groove geometry is represented by the leading mode of the Fourier expansion representing this geometry. It has been shown that the difference between forces determined using the complete geometry and the reduced model is of the order of a few percent and, thus, the error associated with the use of the simplified geometry model is acceptable in most applications. The main advantage of the reduced geometry model is the generality and simplicity of the solution as the force determination involves the extraction of the dominant mode from the Fourier expansion describing groove geometry and determination of this

force from the tabulated results for sinusoidal grooves. The reduced geometry model eliminates the need to study each groove geometry separately.

It has been shown that grooves always increase the force required to maintain the plate movement. The long wavelength grooves produce spatial flow modulations resulting in a small force increase when compared with the smooth conduits. The short wavelength grooves provide a much larger force increase due to the blockage effect resulting in the stream lift-up phenomenon. This phenomenon is driven by the groove sidewalls coming closer together and forcing the stream to move away from the grooved plate reducing the effective hydraulic conduit opening. The magnitude of the force associated with the spatial flow modulations increases proportionally to the second power of the groove amplitude and proportionally to the flow Reynolds number for conditions of interest in this analysis.

## Chapter 6

### 6 Flow between heated grooved plates in relative motion

Results presented in Chapters 4 and 5 demonstrated that periodic heating reduces the driving force while geometric irregularities increase this force. It is of interest to determine how a combination of these two effects may affect the driving force. The dynamics of a system composed of a grooved lower plate subject to a spatially periodic heating characterized by the same wave number and a smooth isothermal upper plate is discussed in this chapter. The flow system is illustrated in Figure 6-1. Geometric irregularities have the form of sinusoidal grooves which are heated in a manner giving rise to sinusoidal wall temperature distribution. The relative position of the heating pattern with respect to the geometric pattern is measured using the phase difference  $\Omega$ . The effects of variations of the phase difference are highlighted in Section 6.1. Effects of different parameters such as the heating wave number  $\alpha$ , the flow Reynolds number  $Re$ , the amplitude of the grooves  $y_b$  and the heating intensity  $Ra_p$  are discussed in Sections 6.2-6.5. Effects of the unequal mean temperatures of the plates are discussed in Section 6.6. All results presented in Sections 6.1- 6.6 are for fluids with the Prandtl number  $Pr = 0.71$ , which well approximates the properties of air. The effects of changing the type of fluid (changing  $Pr$ ) are discussed in Section 6.7. Heat transfer characteristics are discussed in Section 6.8. Finally, a concise summary of the results presented in this Chapter is given in Section 6.9.

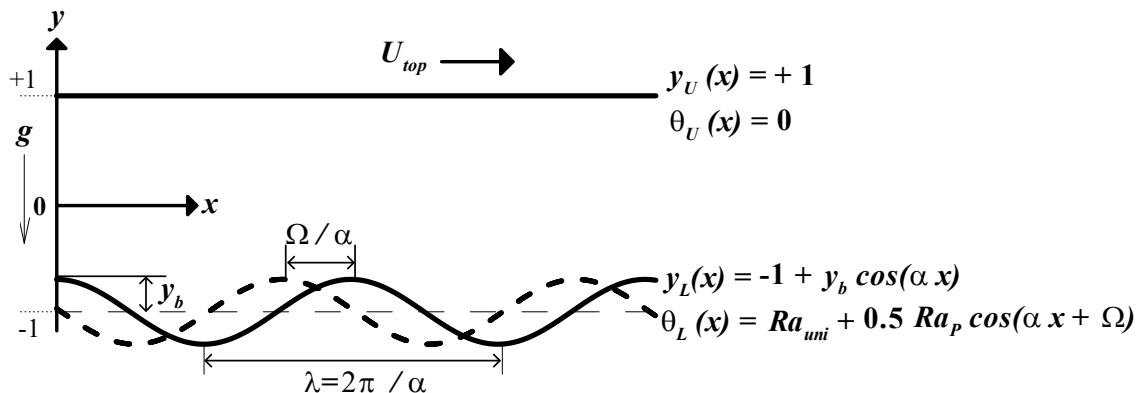


**Figure 6-1:** Schematic diagram of the flow system.

## 6.1 Effects of the phase difference

The evolution of the flow field in response to changes of  $\Omega$  is illustrated in Figure 6-2(A-H). When  $\Omega = 0$ , the heating pattern is in-phase with the geometric pattern and the temperature peaks at the lower plate overlap with the groove peaks. The resulting flow field consists of rolls rotating in the clockwise and counter-clockwise directions with the fluid moving upwards above the hot spots and downwards above the cold spots. There exists a stream tube moving upwards around the hot spots and downwards around the cold spots while carrying the fluid in the positive  $x$ -direction (see Figure 6-2A). Similar flow structures were seen in Chapter-4 when the lower plate was smooth. At  $\Omega = \pi/4$ , when the groove peaks and the hot spots do not overlap, the size of the convection rolls slightly decreases to allow for the increase of the stream tube; this permits more fluid to move in the positive  $x$ -direction and creates a jet-like effect near the upper plate (see Figure 6-2B). The strength of this jet-like effect further increases at  $\Omega = \pi/2$  as the size of the clockwise rolls decreases (see Figure 6-2C). However, at  $\Omega = 3\pi/4$ , as the temperature peaks move closer to the groove troughs, the intensity of the jet begins to decrease due to the dominance of the centrifugal effects around the troughs (see Figure 6-2D). The jet disappears when the temperature peaks overlap with the groove troughs at  $\Omega = \pi$  and the size of the convection rolls becomes the same as that observed at  $\Omega = 0$  with the direction of the rotation of the corresponding rolls reversed (see Figure 6-2E). A narrow stream tube still exists and carries fluid in the positive  $x$ -direction. When the phase difference is further increased to  $\Omega = 5\pi/4$ , the hot spots move to the other side of the troughs and the increase of the reverse rotation of convection rolls causes the jet-like-effect to reverse its direction, producing a backward motion in the stream tube (see Figure 6-2F). An enlargement of the upper part of this figure (see Figure 6-3A) demonstrates the formation of a stagnation point in the vicinity of the upper plate, the existence of a thin layer of fluid dragged forward in the immediate vicinity of the upper plate and the reversed movement of the fluid in the stream tube. The magnitude of the backward flow in the stream tube is further increased at  $\Omega = 3\pi/2$  (see Figure 6-2G). As the locations of the hot spots approach groove peaks, the intensity of the backward motion gradually decreases (see Figure 6-2H) and, at  $\Omega = 2\pi$ , the flow field returns to the form observed at  $\Omega = 0$  (Figure 6-2A).

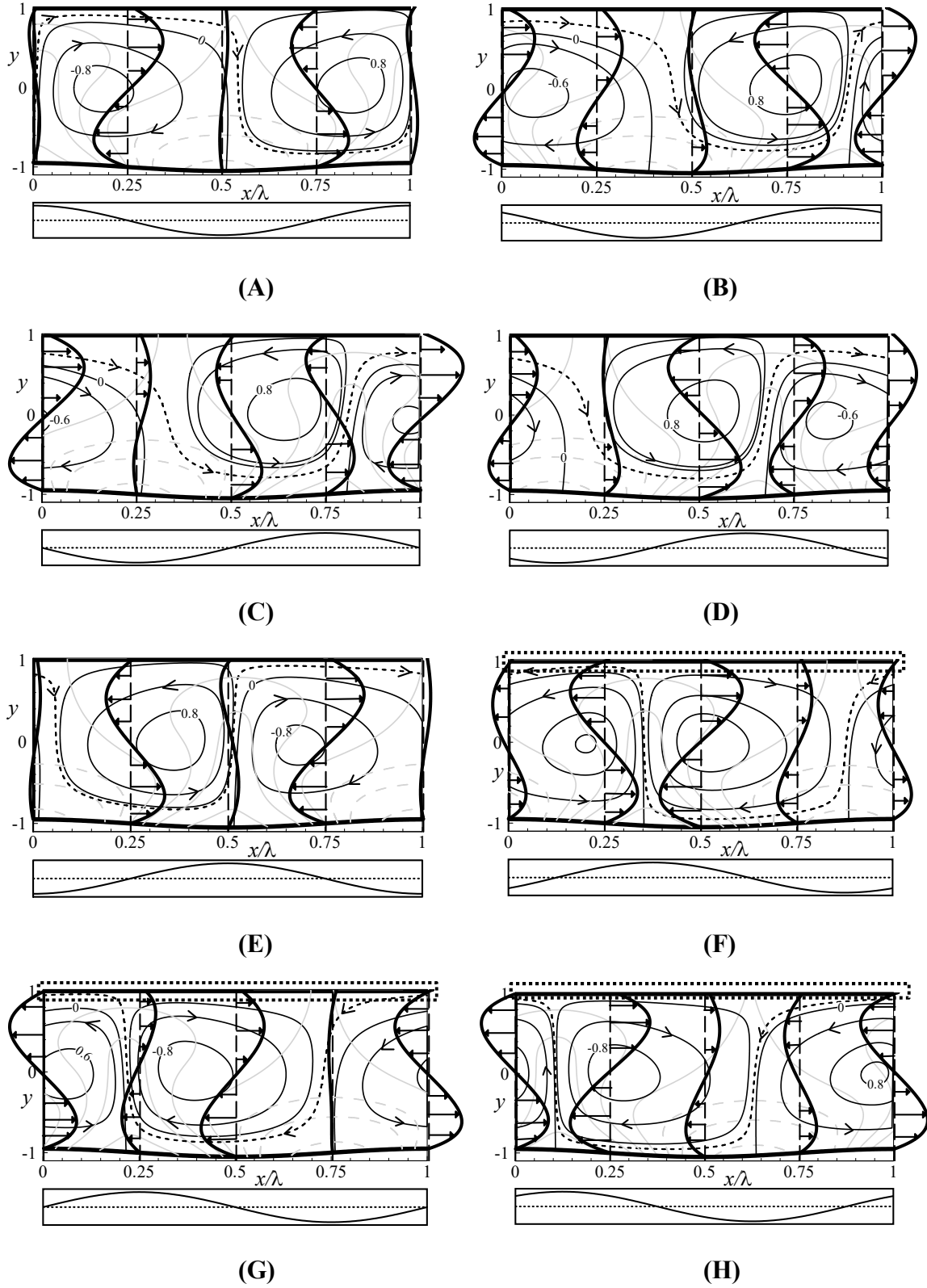


**Figure 6-2:** Evolution of the flow fields as a function of  $\Omega$  for  $y_b = 0.05$ ,  $\alpha = 1$ ,  $Ra_p = 1000$ ,  $Re = 1$ . Figures (A-H) display results for  $\Omega = 0, \pi/4, \pi/2, 3\pi/4, \pi, 5\pi/4, 3\pi/2, 7\pi/4$ ,



respectively. Black solid lines identify streamlines associated with the buoyancy-driven rolls while black dashed lines identify streamlines associated with the net flow in the horizontal direction. Grey solid and dashed lines identify the positive and negative isotherms. The lower plate temperature distribution is shown below each figure. Enlargements of boxes marked using dotted lines in Figures (F-H) are shown in Figure 6-3.

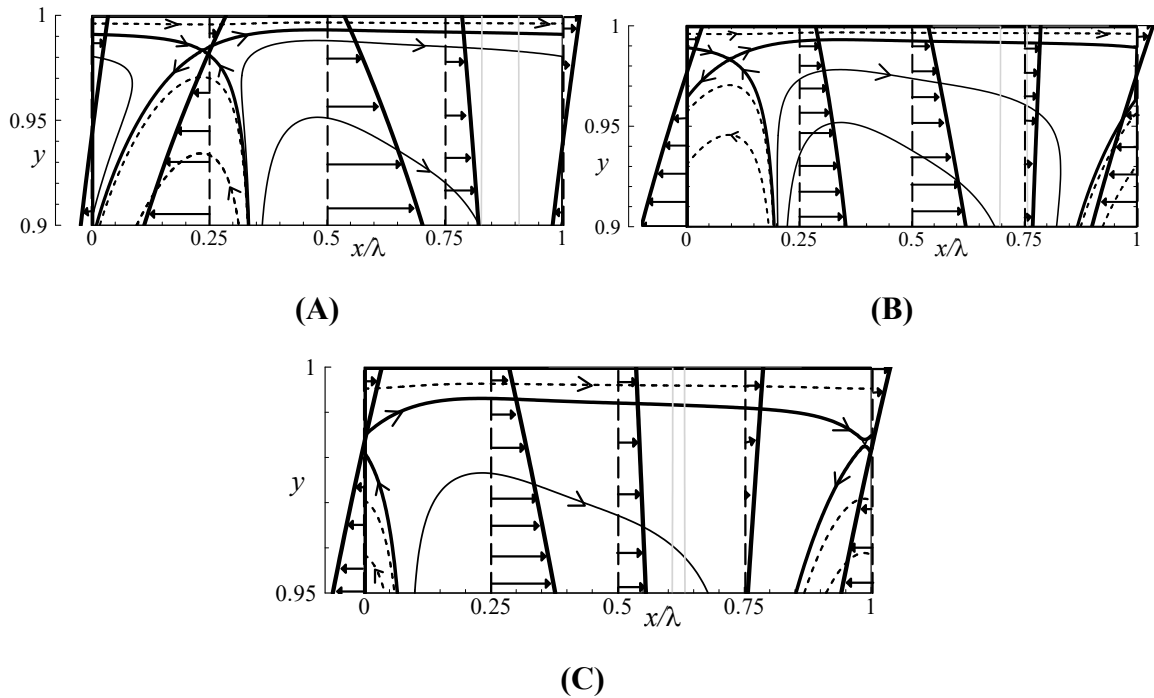
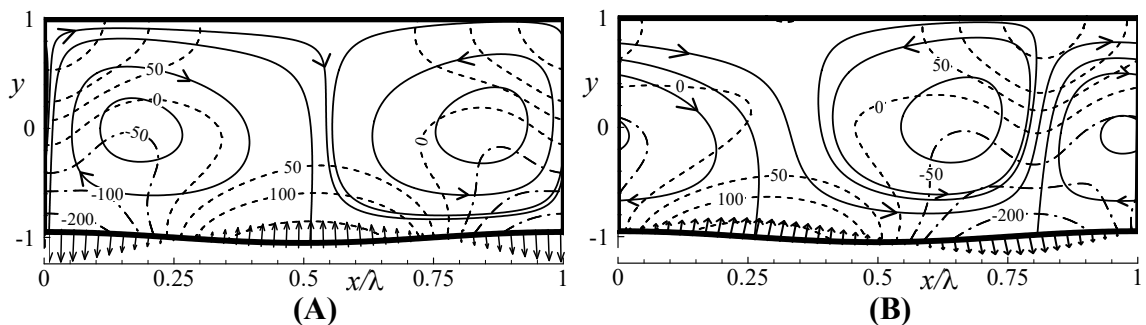


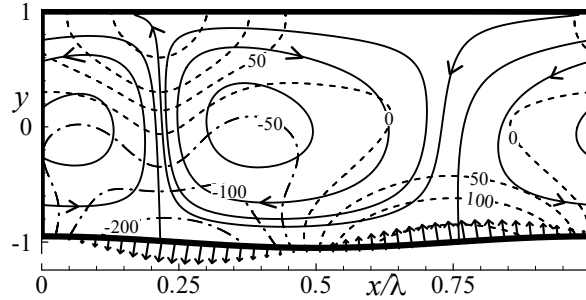
**Figure 6-3:** Enlargements of the flow fields near the upper plate for (A)  $\Omega = 5\pi/4$ , (B)  $\Omega = 3\pi/2$ , and (C)  $\Omega = 7\pi/4$ . The remaining flow conditions are given in Figure 6-2.

The reversal of the rolls' rotation for  $\pi < \Omega < 2\pi$  causes the bulk of the fluid to move in the direction opposite to the direction of the plate. A closer look at the flow field reveals the formation of a stagnation point very near to the upper plate which separates fluid being pulled by the plate from fluid flowing backwards inside the stream tube (see Figure 6-3A-C). Consequently, the fluid in the upper plate region continues to move in the forward direction while the fluid in the rest of the channel moves in the opposite direction. Because of these two opposing mechanisms, a larger force would be needed to maintain the motion of the plate in the positive  $x$ -direction.

Further investigation of mechanisms responsible for the creation of the backward flow in the stream tube for  $\Omega > \pi$  raises the question of the identification of forces responsible for this effect. As there is no external pressure gradient and only the movement of the upper plate drives the flow, there must be other forces which push the fluid. It has been found that the presence of grooves and heating leads to a change in the distribution of pressure and viscous forces (see Appendix B for their evaluation) and it is the induced pressure force, more specifically, the  $x$ -component of the induced pressure force, that forces the fluid movement in the stream tubes. This pressure force was referred to as the pressure interaction drag by Mohammadi & Floryan (2012) in the analysis of drag formation in isothermal grooved channels, and as the thermal drifting force by Abtahi & Floryan (2017b) in the analysis of convection problems. This force acts as the external propulsion that creates the movement of fluid in the stream tubes and is formed through an interaction of the grooves and the external heating.

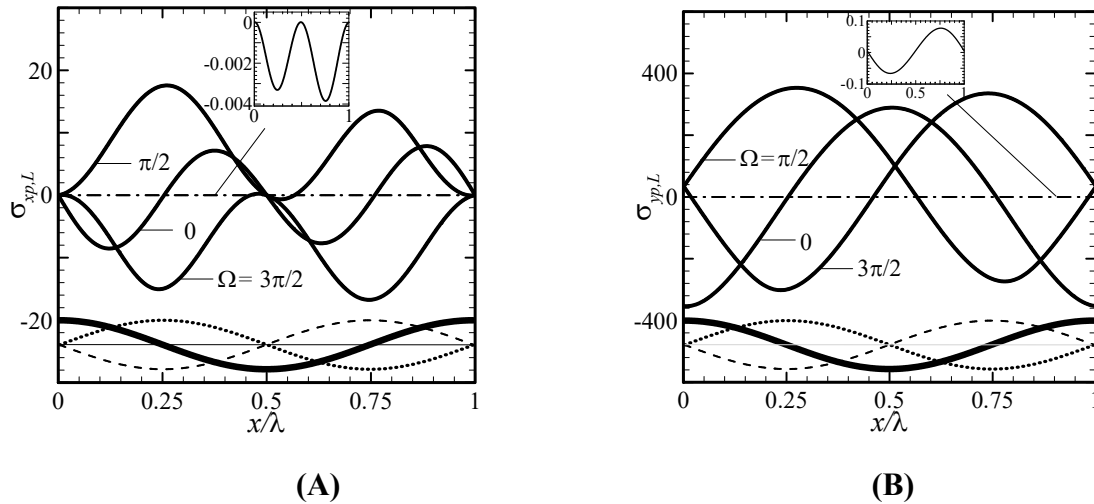
Distributions of the pressure field in the channel and the pressure force at the lower plate are displayed in Figure 6-4(A-C) for three representative  $\Omega$ 's. The interaction of the pressure field with the grooves creates pressure force which may have a non-zero  $x$ -component when integrated over one wavelength. This pressure force acts in the favorable direction for  $\Omega = \pi/2$  and in the adverse direction for  $\Omega = 3\pi/2$ ; it is this pressure force which causes the fluid in the stream tubes to move in the forward and backward directions, respectively. The variations of the  $x$ - and  $y$ -components of the pressure force can be seen in Figure 6-5. The  $y$ -component drives the convection rolls. A positive  $x$ -component assists the plate in forcing the fluid to move in the forward direction (when  $\Omega = \pi/2$ ) and a negative  $x$ -component opposes the movement created by the upper plate (when  $\Omega = 3\pi/2$ ).





(C)

**Figure 6-4:** Evolution of the flow field as a function of  $\Omega$  for  $y_b = 0.05$ ,  $\alpha = 1$ ,  $Ra_p = 1000$ ,  $Re = 1$ . Figures (A-C) display results for  $\Omega = 0, \pi/2, 3\pi/2$ , respectively. Solid lines identify streamlines, and dashed and dashed-dotted lines identify the positive and negative isobars. Arrows at the lower plate illustrate pressure forces.



(A)

(B)

**Figure 6-5:** Distribution of (A) the  $x$ -component  $\sigma_{xp,L}$ , and (B) the  $y$ -component  $\sigma_{yy,L}$  of the pressure force at the lower plate for  $y_b = 0.05$ ,  $Re = 1$ ,  $\alpha = 1$ ,  $Ra_p = 1000$ , and  $\Omega = 0, \pi/2, 3\pi/2$ . The dashed-dotted line illustrates the no heating conditions. The thick line below each figure illustrates the groove shape, and dashed and dotted lines illustrate plate temperatures for  $\Omega = \pi/2, 3\pi/2$ , respectively.

Changing the relative position of grooves with respect to the temperature pattern leads to changes of the magnitude in the horizontal pressure force and, thus, affects the net horizontal flow. As a result, change in the flow pattern changes the shear force opposing movement of the upper plate. The variation of the shear stress distribution at the upper plate is depicted in Figure 6-6. It is seen that the magnitude of the mean shear varies with

$\Omega$ , and this mean shear needs to be overcome by the external force in order to maintain the plate movement. Larger positive values of this mean shear translate into a smaller force needed to drive the upper plate (in the forward direction). Thus, one can easily infer that the driving force decreases when  $\Omega = \pi/2$  and increases when  $\Omega = 3\pi/2$ .

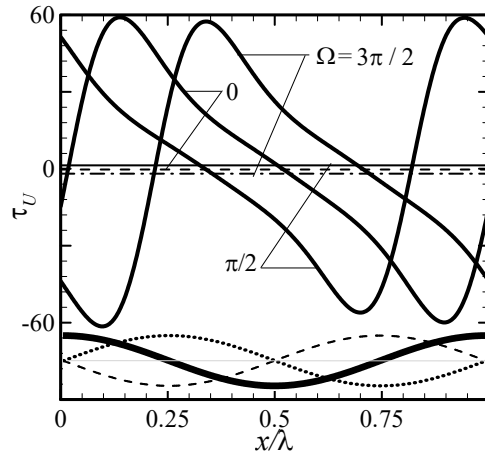


**Figure 6-6:** Shear stress distributions at the upper plate ( $\tau_U$ ) for  $y_b = 0.05$ ,  $Re = 1$ ,  $\alpha = 1$ ,  $Ra_p = 1000$  and  $\Omega = 0, \pi/2, 3\pi/2$ . The thick line below the figure illustrates the shape of the groove, and dashed and dotted lines illustrate plate temperatures for  $\Omega = \pi/2, 3\pi/2$ , respectively. The mean values of shear are marked using horizontal lines.

Variations of the driving force as a function of the phase difference  $\Omega$  are illustrated in Figure 6-7A. Positive values of  $\Delta F$  denote force reduction whereas negative values denote force increase. It can be seen that  $\Delta F$  exhibits nearly sinusoidal variations with  $\Omega$  which can be divided into three distinct zones. Zone III identifies conditions leading to an increase in the driving force which occurs at  $\Omega \in [\pi, 2\pi]$  for groove amplitudes  $y_b \sim > 0.01$ , with the maximum force increase occurring at  $\Omega \sim 3\pi/2$ . Zone II identifies conditions leading to a decrease in the driving force which can be achieved for all  $\Omega$ 's through a proper choice of the groove amplitude with the maximum force reduction occurring at  $\Omega \sim \pi/2$ . Zone I corresponds to conditions which would lead to plate acceleration. Since such acceleration is not allowed, the driving force must change direction and becomes the braking force. These conditions occur at  $\Omega \in [0, \pi]$  for  $y_b \sim > 0.005$ . One should note that at  $\Omega = 0$ , the force reduction is less than that found in the smooth heated channel. The force reduction

increases for  $\Omega \in [0, \pi/2]$  and, when combined with the grooves, the reduction is almost four times larger than that found in the case of a smooth heated plate.

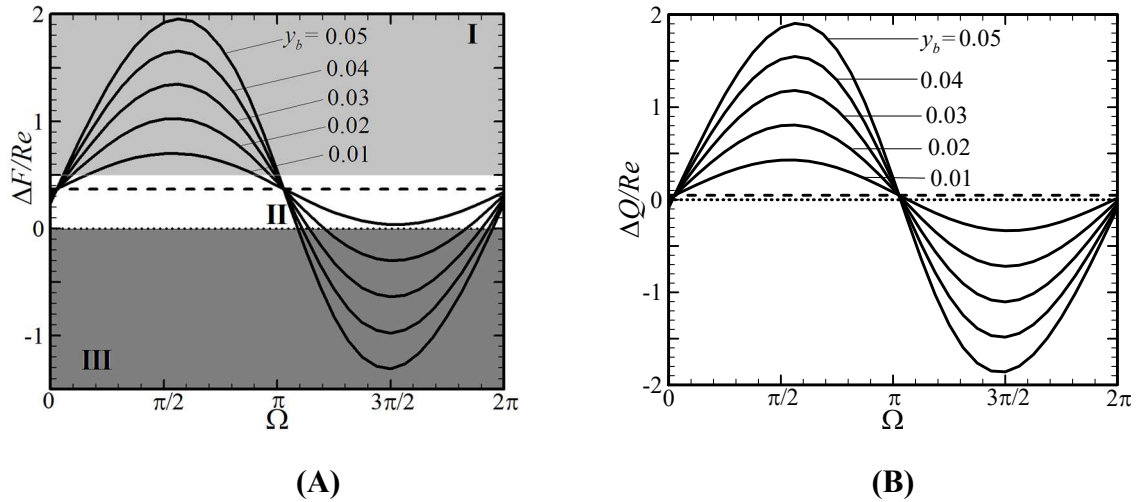


**Figure 6-7:** Variations of (A)  $\Delta F/Re$  and (B)  $\Delta Q/Re$  as functions of the phase difference  $\Omega$  for  $Ra_p = 1000$ ,  $Re = 1$ ,  $\alpha = 1$  and different groove amplitudes. Dashed lines identify results for the smooth lower plate. The light gray shaded area (zone I) identifies conditions requiring the use of braking force. The white area (zone II) identifies conditions resulting in a reduction of the driving force. The dark gray shaded area (zone III) identifies conditions requiring an increase of the driving force.

The change in the amount of fluid dragged by the upper plate,  $\Delta Q$ , follows a similar trend with the maximum of  $\Delta Q$  occurring at  $\Omega \sim \pi/2$  and a minimum occurring at  $\Omega \sim 3\pi/2$  (See Figure 6-7B).

## 6.2 Effects of the wavenumber

Results shown in Figure 6-8 demonstrate that variations of the driving force as a function of the wavenumber  $\alpha$  are qualitatively similar to those discussed in Chapter 4, except for zone III where an increase of driving force occurs due to the flow reversal for certain  $\Omega$ 's. For favorable phase differences, i.e.  $\Omega = \pi/2$ , all heating wavenumbers lead to force reduction and the magnitude of this reduction is much bigger than that found in the case of a smooth heated plate. The maximum force reduction occurs at  $\alpha \sim 1.8 - 2$ . This reduction

decreases when an excessively small  $\alpha$  is used. Also, the use of an excessively large  $\alpha$  leads to its very rapid decrease. Corresponding change in flow rate is shown in Figure 6-9. Flow topologies shown in Figure 6-10 demonstrate that an increase of  $\alpha$  leads to the formation of a thermal boundary layer near the lower plate where the convective effects concentrate with a conductive layer forming above it.

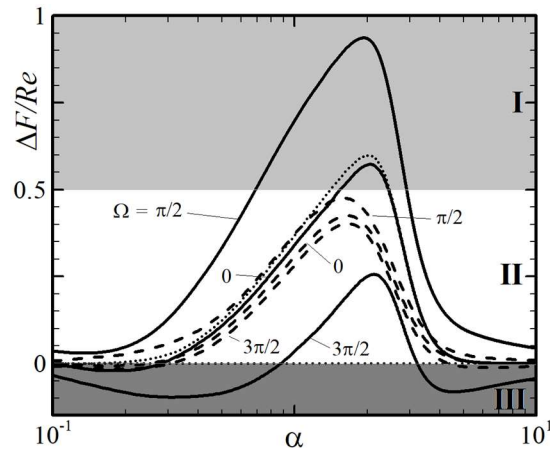


**Figure 6-8:** Variations of  $\Delta F/Re$  as a function of  $\alpha$  for  $y_b = 0.01$ ,  $Ra_p = 1000$  and  $Re = 1, 5$  (solid and dashed lines, respectively). Dotted lines illustrate conditions for the smooth lower plate. The light gray shaded area (zone I) identifies conditions requiring the use of braking force. The white area (zone II) identifies conditions resulting in a reduction of the driving force. The dark gray shaded area (zone III) identifies conditions requiring an increase of the driving force.

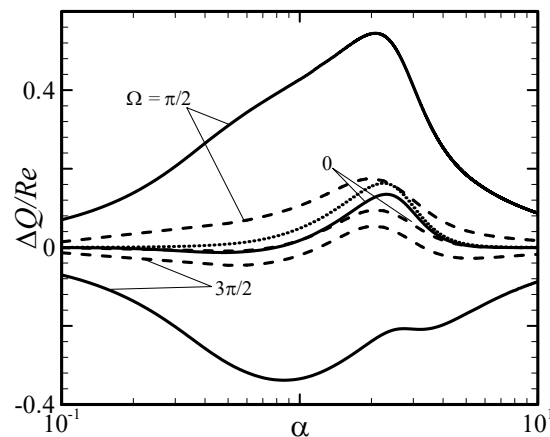


**Figure 6-9:** Variations of  $\Delta Q/Re$  as a function of  $\alpha$  for  $y_b = 0.01$ ,  $Ra_p = 1000$  and  $Re = 1, 5$  (solid and dashed lines, respectively). Dotted lines illustrate conditions for the smooth lower plate.

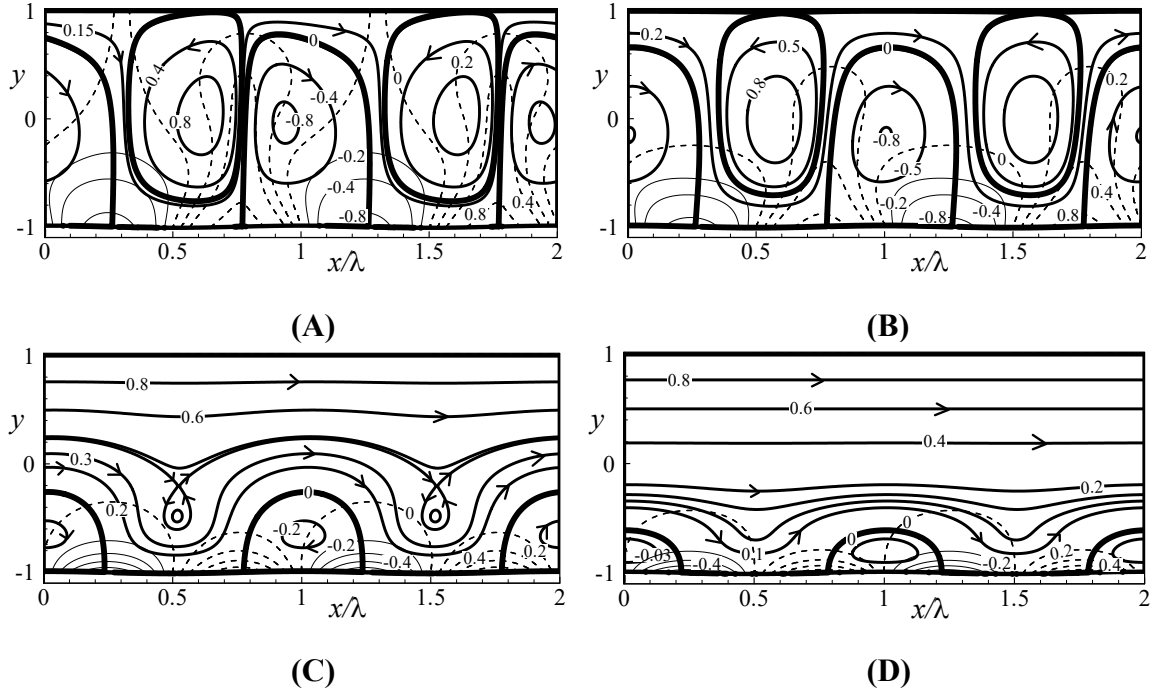


**Figure 6-10:** Variations of the flow and temperature field for  $\Omega = \pi/2$ ,  $Ra_p = 1000$ ,  $y_b = 1$ ,  $Re = 1$  for (A)  $\alpha = 1$ , (B)  $\alpha = 2$ , (C)  $\alpha = 5$ , (D)  $\alpha = 8$ . Thin dashed and solid lines illustrate the positive and negative isotherms, respectively.

### 6.3 Effects of the Reynolds number

The change of driving force as a function of  $Re$  is illustrated in Figure 6-11. It can be seen that the force-reducing effect is a strong function of  $Re$  for all  $\Omega$ 's. The magnitude of  $\Delta F$  increases almost proportionally to  $Re$  for small  $Re$ 's, reaches a maximum at  $Re \sim 5-6$  and then decreases with a higher rate. The flow topologies shown in Figure 6-13 demonstrate that the decrease of  $\Delta F$  is associated with the reduction of convection bubbles and confinement of convection effects to a thin boundary layer near the lower plate at higher  $Re$ . Variations of the flow rate follow a similar pattern (see Figure 6-12), i.e. it increases at first almost proportionally to  $Re$ , reaches a maximum at  $Re \sim 5-6$  and then decreases.

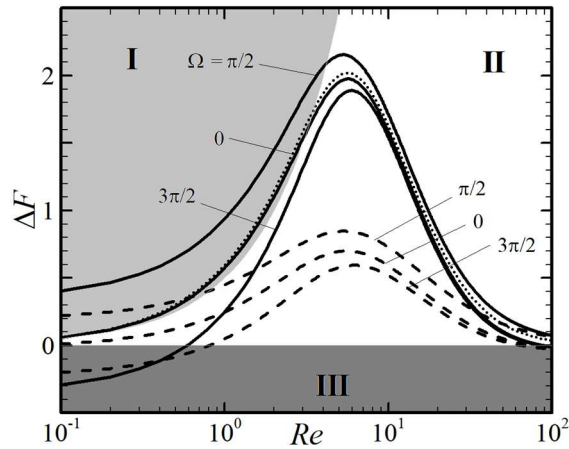


**Figure 6-11:** Variations of  $\Delta F$  as a function of  $Re$  for  $y_b = 0.01$ ,  $Ra_p = 1000$  and  $\alpha = 2, 3$  (solid and dashed lines, respectively). Dotted lines illustrate results for the smooth lower plate. The light gray shaded area (zone I) identifies conditions requiring the use of braking force. The white area (zone II) identifies conditions resulting in a reduction of the driving force. The dark gray shaded area (zone III) identifies conditions requiring an increase of the driving force.

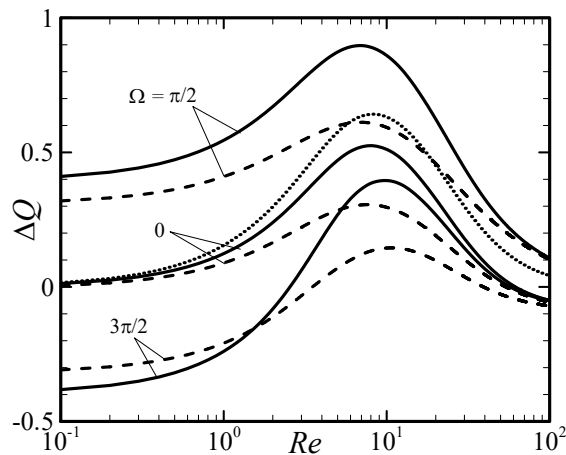


**Figure 6-12:** Variations of  $\Delta Q$  as a function of  $Re$  for  $y_b = 0.01$ ,  $Ra_p = 1000$  and  $\alpha = 2, 3$  (solid and dashed lines, respectively). Dotted lines illustrate results for the smooth lower plate.



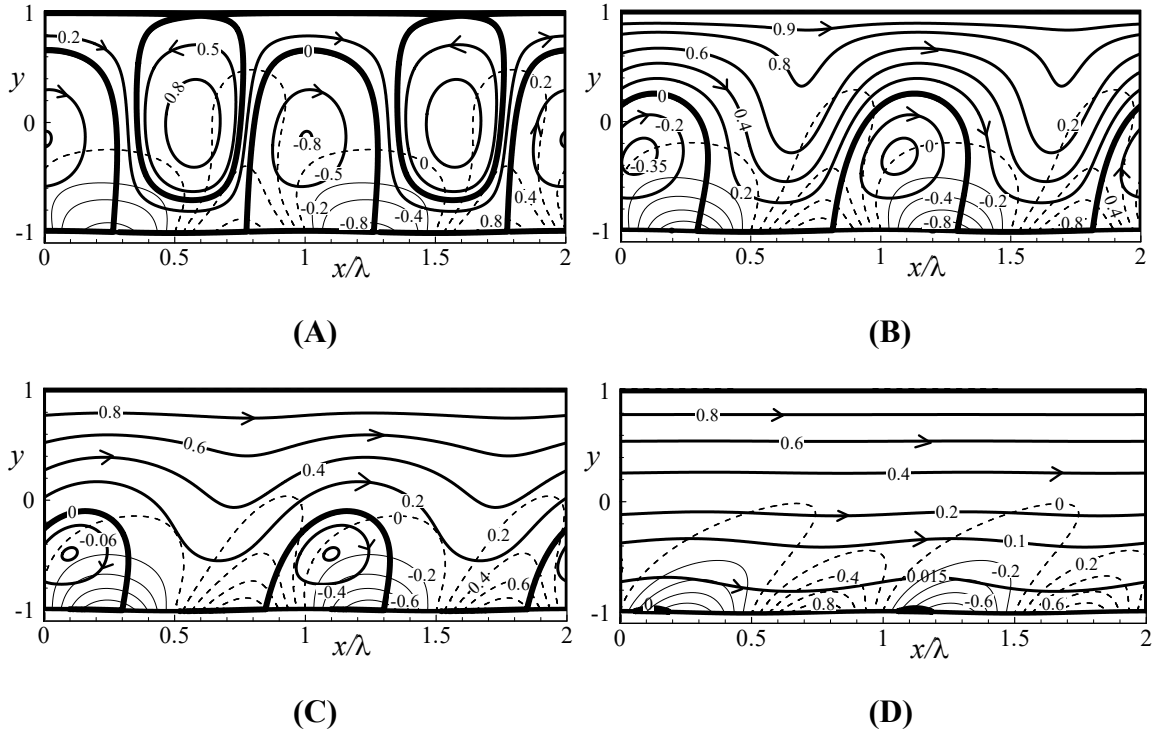


**Figure 6-13:** Variations of the flow and temperature fields for  $\Omega = \pi/2$ ,  $Ra_p = 1000$ ,  $y_b = 1$ ,  $\alpha = 2$  for (A)  $Re = 1$ , (B)  $Re = 5$ , (C)  $Re = 10$ , (D)  $Re = 50$ . Thin dashed and solid lines illustrate the positive and negative isotherms.

## 6.4 Effects of the groove amplitude

The effect of increasing the amplitude of surface irregularities on the driving force is illustrated in Figure 6-14. In general, an increase of the groove amplitude increases the force augmentation. This augmentation may be either positive or negative, depending on the phase difference  $\Omega$ . When the most effective phase difference is used ( $\Omega = \pi/2$ ) together with the most effective wavenumber ( $\alpha = 2$ ), the force reduction (zones I and II) increases for all  $Re$ 's. When the least effective phase difference is used ( $\Omega = 3\pi/2$ ), the magnitude of force reduction decreases and, if the groove amplitudes are large enough, driving force must increase, i.e.  $\Delta F < 0$  (zone III).

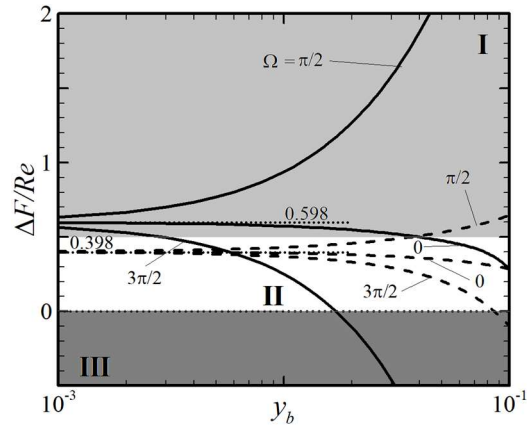


**Figure 6-14:** Variations of  $\Delta F/Re$  as a function of  $y_b$  for  $Ra_p = 1000$ ,  $\alpha = 2$ ,  $Re = 1, 5$  (solid and dashed lines, respectively). Dotted lines illustrate the solution for the smooth plate. The light gray shaded area (zone I) identifies conditions requiring the use of braking force. The white area (zone II) identifies conditions resulting in a reduction of the driving force. The dark gray shaded area (zone III) identifies conditions requiring an increase of the driving force.

The difference in the flow rate  $\Delta Q$  varies in a similar manner (see Figure 6-15). For favorable phase differences, larger amounts of fluid are pulled by the plate, and for the non-favorable phase differences, smaller amounts of fluid are pulled with magnitudes of the augmentation increasing with  $y_b$ . This trend is similar for all  $Re$ 's considered in this study. Both  $\Delta F$  and  $\Delta Q$  increase proportionally to  $y_b$  for all phase differences considered.

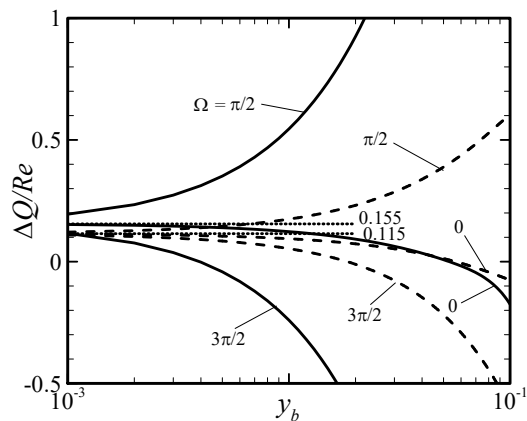


**Figure 6-15:** Variations of  $\Delta Q/Re$  as a function of  $y_b$  for  $Ra_p = 1000$ ,  $\alpha = 2$  and  $Re = 1, 5$  (solid and dashed lines, respectively). Dotted lines illustrate solutions for the smooth lower plate.

A closer look at the flow fields (see Figure 6-16) for  $\Omega = \pi/2$  reveals that as  $y_b$  increases, the convection rolls contract. This facilitates an increase of the stream tube and an increase of the net horizontal flow rate. An increase of the groove amplitude results in an increase of the thermal drift effect (the  $x$ -component of the surface pressure force increases) and, hence, change in the force  $\Delta F$  increases. Selection of the appropriate  $y_b$  can place the system response either in zone I or zone II.

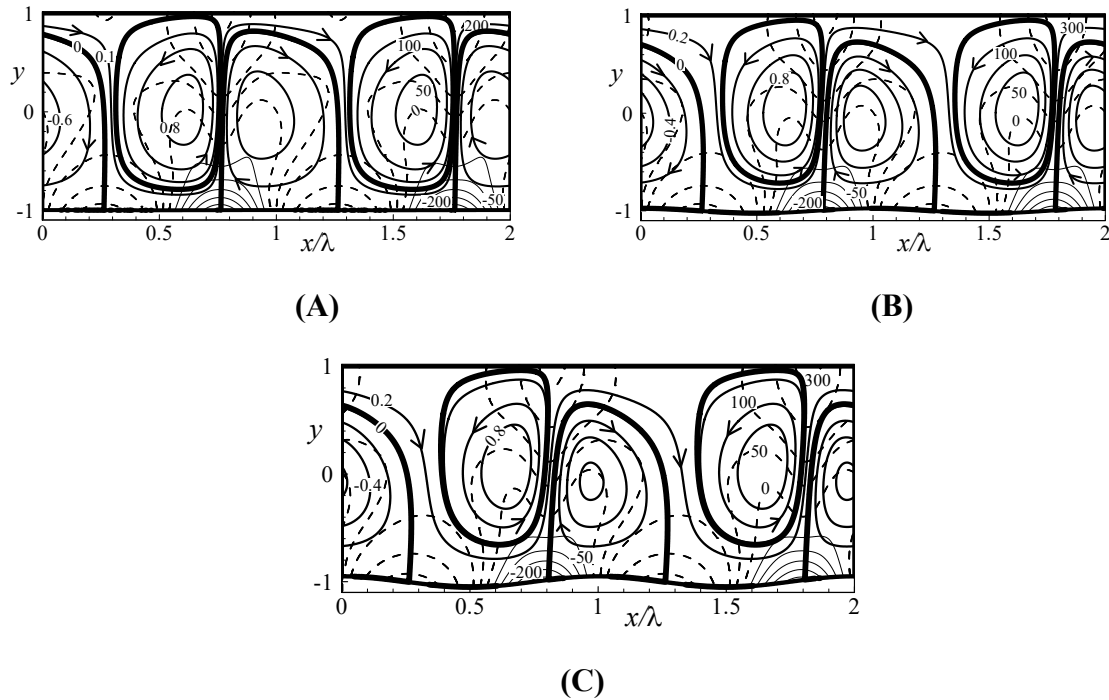


**Figure 6-16:** Variations of the flow and pressure fields for  $\Omega = \pi/2$ ,  $Ra_p = 1000$ ,  $\alpha = 1$ ,  $Re = 1$  for (A)  $y_b = 0.001$ , (B)  $y_b = 0.025$ , and (C)  $y_b = 0.05$ . Thin dashed and solid lines illustrate the positive and negative isobars.

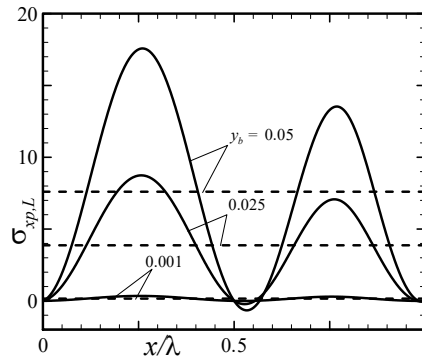


**Figure 6-17:** Variations of the  $x$ -component of the induced pressure force for the flow fields shown in Figure 6-16(A-C).

## 6.5 Effects of the heating intensity

The strength of the thermal drift increases with an increase of the heating intensity and, thus, the change in driving force is a strong function of  $Ra_p$ . As  $Ra_p$  is increased, the force reduction increases proportionally to  $Ra_p$  for favorable phase differences. A state of saturation develops for large enough  $Ra_p$  slowing down this growth. The saturation starts at a smaller  $Ra_p$  when  $Re$  is small (Figure 6-18). Change in  $\Delta F$  occurs due to the change in the thermal drift as well as the change in the size of the convection rolls. Flow topologies shown in Figure 6-20 illustrate the roll expansion and reduction of the stream tube due to an increase of  $Ra_p$ . The amount of fluid driven by the plate increases with  $Ra_p$  for favorable phase differences ( $\Omega = 0, \pi/2$ ) (see Figure 6-19).

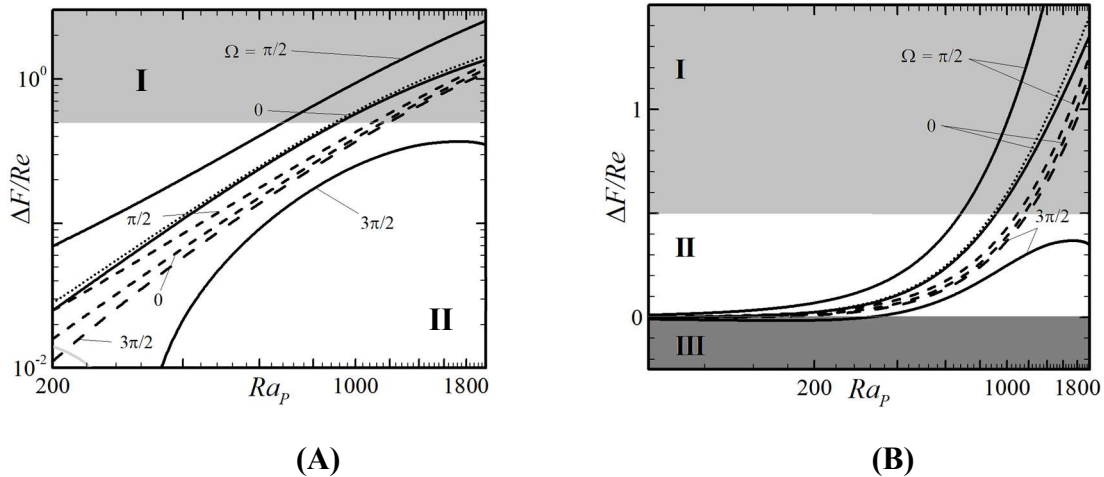


**Figure 6-18:** Variations of  $\Delta F/Re$  as a function of  $Ra_p$  for  $y_b = 0.01$ ,  $\alpha = 2$  and  $Re = 1, 5$  (solid and dashed lines, respectively). Dotted lines illustrate results for the smooth lower plate. Figure (A) displays results in the log-log scale while Fig. (B) uses the semi-log scale. The light gray shaded area (zone I) identifies conditions requiring the use of braking force. The white area (zone II) identifies conditions resulting in a reduction of the driving force. The dark gray shaded area (zone III) identifies conditions requiring an increase of the driving force.

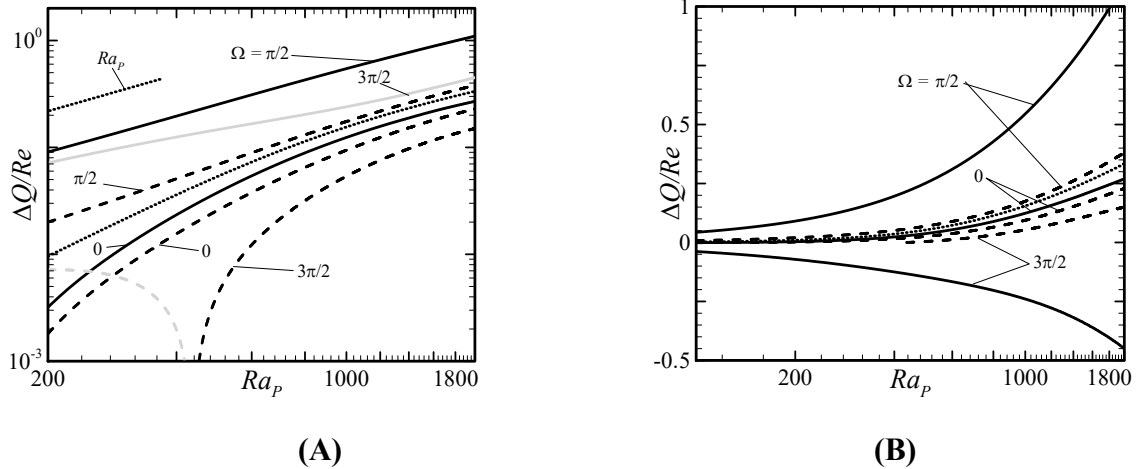


**Figure 6-19:** Variations of  $\Delta Q/Re$  as a function of  $Ra_p$  for  $y_b = 0.01$ ,  $\alpha = 1$  and  $Re = 1, 5$  (solid and dashed lines, respectively). Dotted lines identify results for the smooth lower plate. Grey lines identify negative values. Figure (A) displays results in the log-log scale while Fig. (B) uses the semi-log scale.

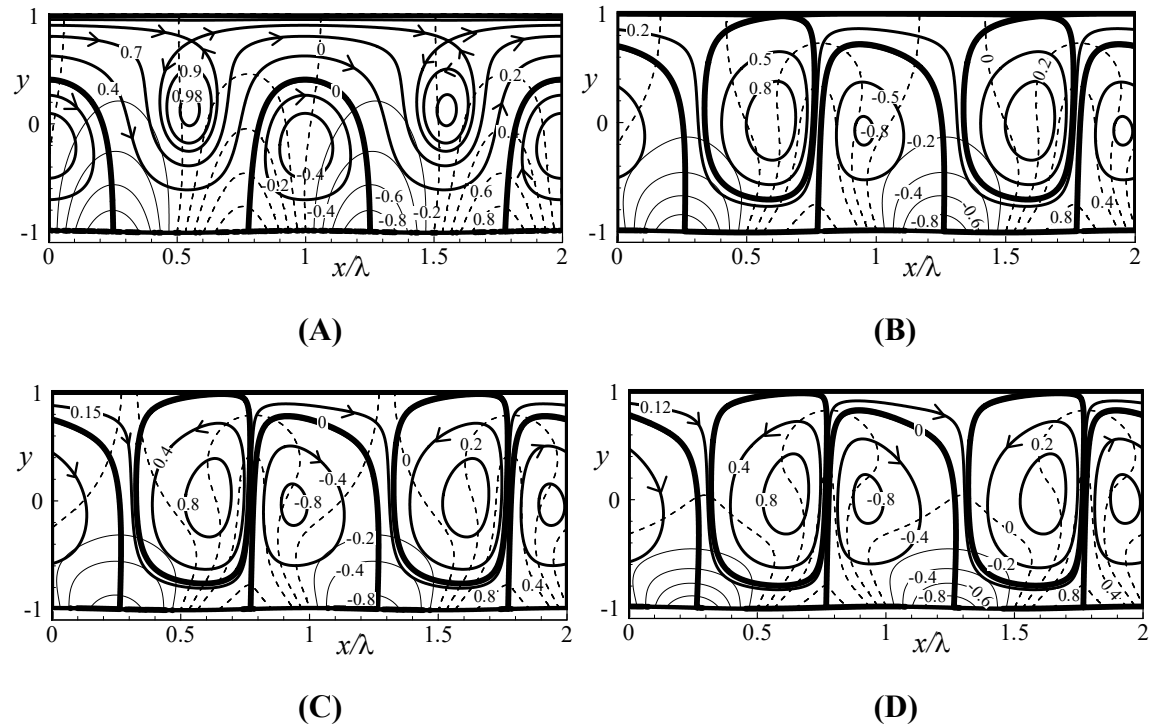


**Figure 6-20:** Variations of the flow and temperature fields for  $\Omega = \pi/2$ ,  $y_b = 1000$ ,  $\alpha = 1$ ,  $Re = 1$  for (A)  $Ra_p = 100$ , (B)  $Ra_p = 500$ , (C)  $Ra_p = 1000$ , (D)  $Ra_p = 2000$ . Thin dashed and solid lines identify the positive and negative isotherms.

## 6.6 Effects of the plates' mean temperature

It is important to determine how the system reacts when the mean temperatures of the plates are different. This situation is important in practical applications as it may not be possible to maintain equal mean temperatures of both plates. The difference in the mean temperatures is expressed in terms of the uniform Rayleigh number  $Ra_{uni}$ . Positive values for  $Ra_{uni}$  correspond to the lower plate having a higher mean temperature than the upper plate and negative values denote a colder lower plate.

Results presented in Figure 6-21 demonstrate that, for any phase difference  $\Omega$ , an addition of the uniform heating to the lower plate increases  $\Delta F$  while reduction of its temperature decreases  $\Delta F$ . This change in the driving force is approximately linear with  $Ra_{uni}$ . Variations of the force change for higher  $Re$ 's (see lines for  $Re = 5$ ) remain qualitatively similar for the range of  $Ra_{uni}$  studied. Variations of the force as a function of  $\alpha$  remain nearly identical for all phase differences for all  $Ra_{uni}$ 's with an upward shift resulting from an increase of  $Ra_{uni}$  and with a slight increase of the most effective  $\alpha$  (the most effective  $\alpha$  always remains between 2 and 3). Variations of the flow rate  $\Delta Q$  (Figure 6-22) follow the same pattern as variations of  $\Delta F$ .

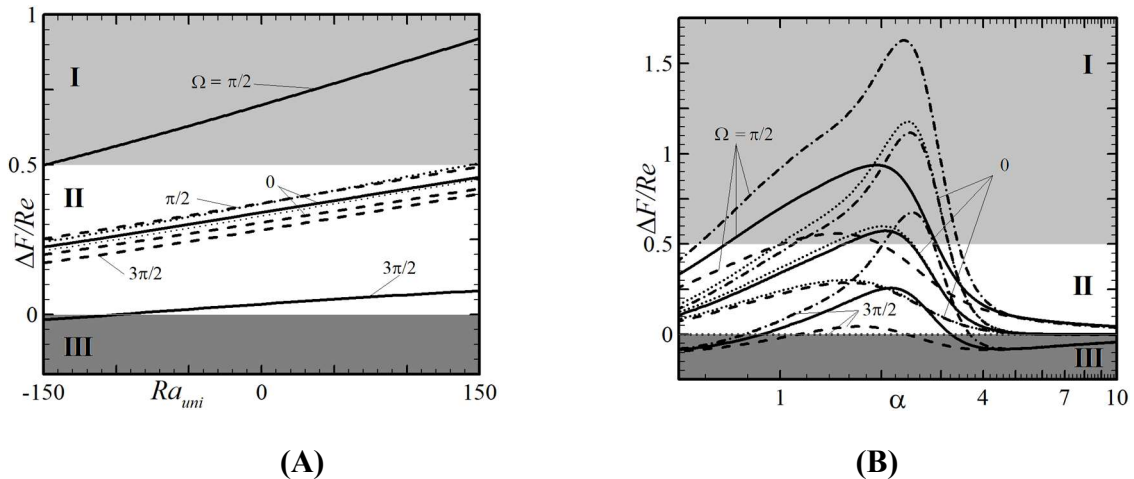


**Figure 6-21:** Variations of  $\Delta F/Re$  for  $Ra_p = 1000$ ,  $y_b = 0.01$  as a function of (A)  $Ra_{uni}$  for  $\alpha = 1$  and (B)  $\alpha$  for  $Re = 1$ . In (A), solid and dashed lines correspond to  $Re = 1, 5$ , respectively. In (B), dashed, solid and dashed-dotted lines correspond to  $Ra_{uni} = -150, 0, 150$ ,

respectively. Dotted lines identify results for the smooth lower plate. The light gray shaded area (zone I) identifies conditions requiring the use of braking force. The white area (zone II) identifies conditions resulting in a reduction of the driving force. The dark gray shaded area (zone III) identifies conditions requiring an increase of the driving force.

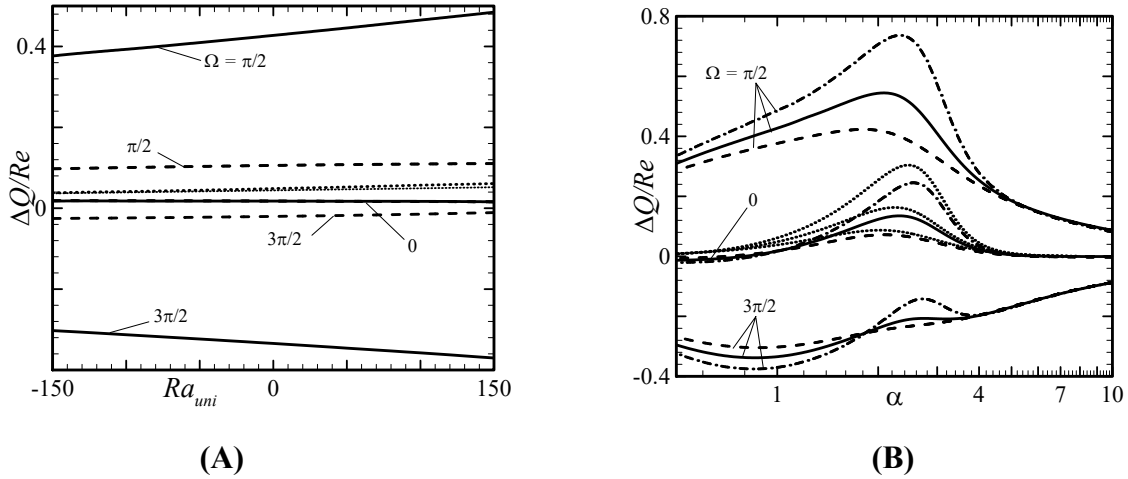


**Figure 6-22:** Variations of  $\Delta Q/Re$  for  $Ra_p = 1000$ ,  $y_b = 0.01$  as a function of (A)  $Ra_{uni}$  for  $\alpha = 1$  and (B)  $\alpha$  for  $Re = 1$ . In (A), solid and dashed lines correspond to  $Re = 1, 5$ , respectively. In (B), dashed, solid and dashed-dotted lines correspond to  $Ra_{uni} = -150, 0, 150$ , respectively. Dotted lines identify results for the smooth lower plate.

## 6.7 Effects of the Prandtl number

The Prandtl number describes transport properties with the conductive effect expected to play a larger role in small- $Pr$  fluids. For such fluids the magnitude of the thermal drift increases (Abtahi & Floryan, 2017a, b) and this leads to an increase of  $\Delta F$ . Results shown in Figure 6-23 demonstrate that a change of  $Pr$  from  $Pr = 10$  to  $Pr = 0.1$  increases  $\Delta F$  by almost three orders of magnitude (Figure 6-23). For a favorable phase difference,  $\Omega = \pi/2$ , the braking force which needs to be applied to the upper plate (zone I) increases with reduction of  $Pr$ . Change in the flow rate  $\Delta Q$  follows the same pattern as documented in Figure 6-24.

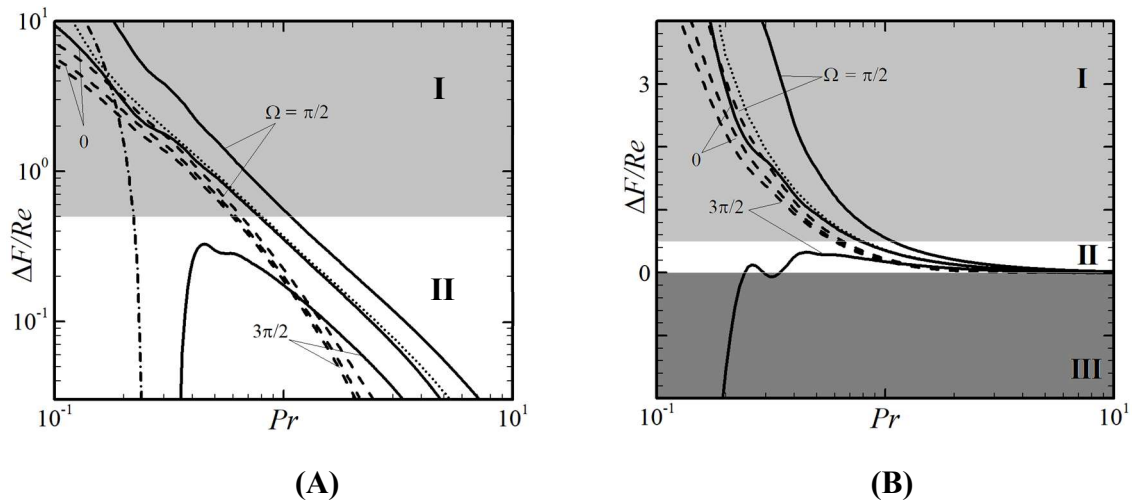


**Figure 6-23:** Variations of  $\Delta F/Re$  as a function of  $Pr$  for  $y_b = 0.01$ ,  $Ra_p = 1000$ ,  $\alpha = 2$  at  $Re = 1, 5$  (solid and dashed lines, respectively). Figure (A) displays results in the log-log scale while Fig. (B) uses the semi-log scale. In (A), dashed-dotted lines identify negative values. Dotted lines are used to identify results for the smooth lower plate at  $Re = 1$ . The light gray shaded area (zone I) identifies conditions requiring the use of braking force. The white area (zone II) identifies conditions resulting in a reduction of the driving force. The dark gray shaded area (zone III) identifies conditions requiring an increase of the driving force.

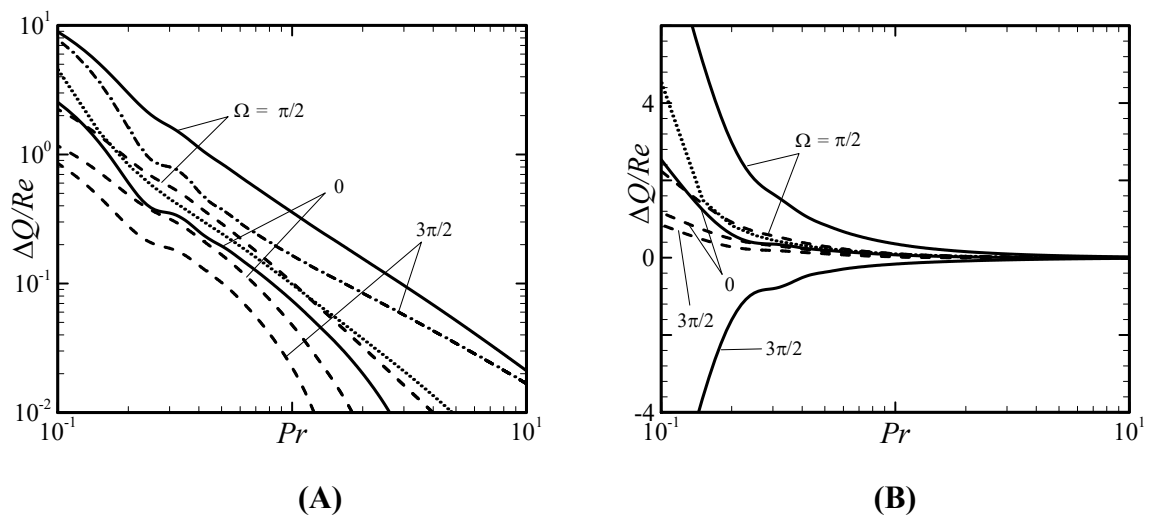


**Figure 6-24:** Variations of  $\Delta Q/Re$  as a function of  $Pr$  for  $y_b = 0.01$ ,  $Ra_p = 1000$ ,  $\alpha = 2$  at  $Re = 1, 5$  (solid and dashed lines, respectively). Fig. (A) displays results in the log-log scale while Fig. (B) uses the semi-log scale. In (A), dashed-dotted lines identify negative values. Dotted lines are used to identify results for the smooth lower plate at  $Re = 1$ .



The character of changes of  $\Delta F$  and  $\Delta Q$  as functions of  $\alpha$  remain qualitatively similar for all  $Pr$ 's with the relevant curves just shifting upwards for smaller  $Pr$ 's, as illustrated in Figure 6-25.

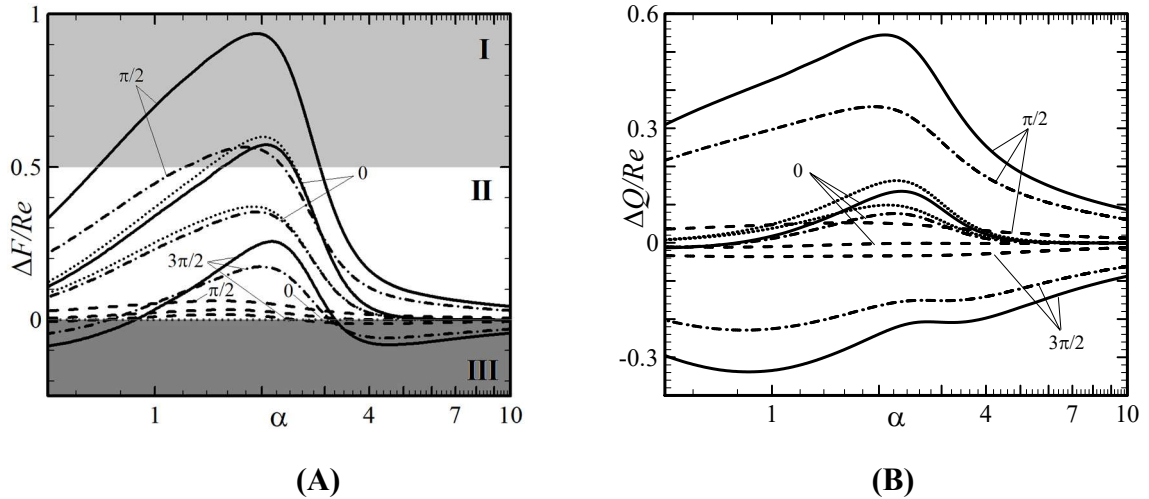


**Figure 6-25:** Variations of (A)  $\Delta F/Re$ , and (B)  $\Delta Q/Re$  as function of  $\alpha$  for  $y_b = 0.01$ ,  $Ra_p = 1000$ ,  $Re = 1$  and  $Pr = 0.71, 1, 5$  (solid, dashed-dotted and dashed lines, respectively). Dotted lines identify conditions for the smooth lower plate. The light gray shaded area (zone I) identifies conditions requiring use of braking force. The white area (zone II) identifies conditions resulting in a reduction of the driving force. The dark gray shaded area (zone III) identifies conditions requiring an increase of the driving force.

## 6.8 Heat transfer effects

The temperature differences between and along the plates generate heat flow in the vertical and horizontal directions. The vertical heat flux, expressed in terms of the mean Nusselt number  $Nu_{av}$ , is of more interest as it can be viewed as an energy cost associated with the use of heating for reduction of the driving force. Figure 6-26 demonstrates that  $Nu_{av}$  is a strong function of both  $\Omega$  and  $\alpha$ , and its magnitude reaches a maximum for  $\Omega \sim 0$  and  $\sim 2\pi$  (minimum at  $\Omega \sim 3\pi/4$ ) and for  $\alpha \sim 0.9-1$  whereas the maximum of  $\Delta F$  occurs at  $\Omega \sim \pi/2$  and at  $\alpha \sim 2$ .

The maximum of  $Nu_{av}$  occurs at  $Re \rightarrow 0$  (Figure 6-27A). An increase of  $Re$  reduces  $Nu_{av}$  through the elimination of convection effects (Figure 6-13). An increase in  $Ra_p$  results in

an increase of  $Nu_{av}$  proportional to  $Ra_p$ , which follows the same trend as  $\Delta F$ , with a slight reduction of growth due to saturation effects in the upper range of  $Ra_p$ 's considered (Figure 6-27B). Increasing the groove amplitude  $y_b$  can either increase or decrease  $Nu_{av}$  depending on the phase difference between the groove and heating patterns (Figure 6-27C).

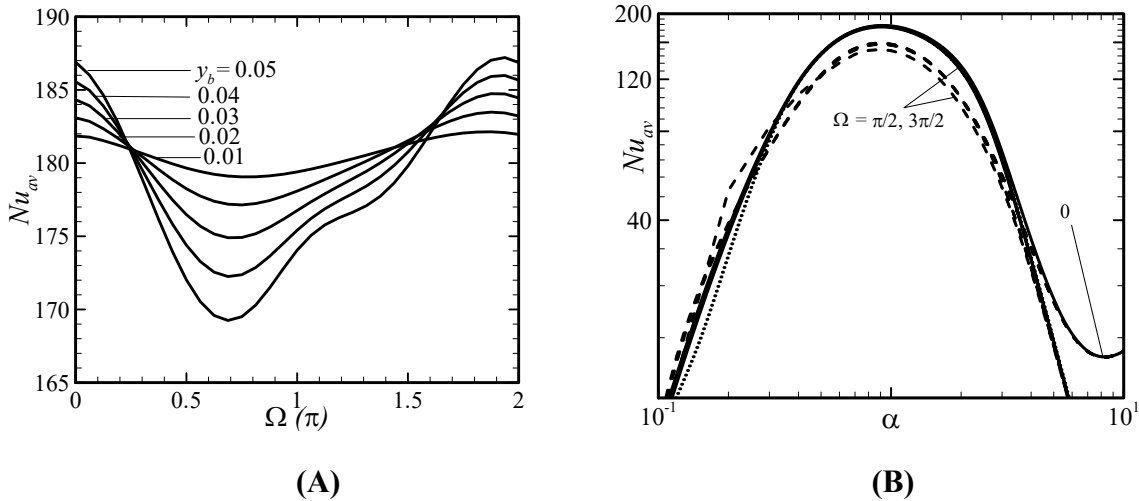


**Figure 6-26:** Variations of  $Nu_{av}$  as a function of (A)  $\Omega$  and (B)  $\alpha$ . In (A),  $Ra_p = 1000$ ,  $\alpha = 1$ ,  $Re = 1$ . In (B),  $Ra_p = 1000$ ,  $y_b = 0.01$ ,  $Re = 1, 5$  (solid and dashed lines, respectively). Dotted lines illustrate conditions for the smooth lower plate.

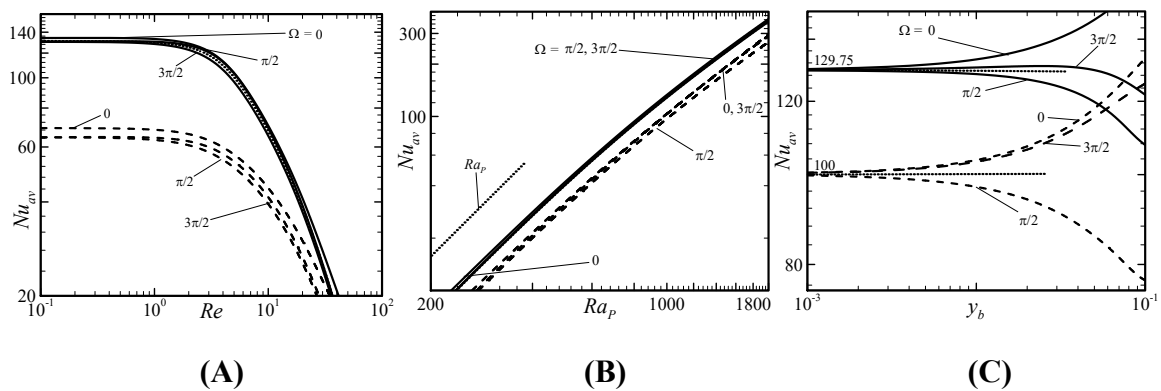


**Figure 6-27:** Variations of  $Nu_{av}$  as a function of (A)  $Re$ , (B)  $Ra_p$ , (C)  $y_b$ . In (A),  $Ra_p = 1000$ ,  $\alpha = 2$  (solid lines) and  $\alpha = 3$  (dashed lines),  $y_b = 0.01$ . In (B),  $y_b = 0.01$ ,  $\alpha = 2$ ,  $Re = 1$  (solid lines) and  $Re = 5$  (dashed lines). In (C),  $Ra_p = 1000$ ,  $\alpha = 2$ ,  $Re = 1$  (solid lines) and  $Re = 5$  (dashed lines). Thin dotted lines identify asymptotes.

An addition of the uniform heating component always leads to a change in the heat flow as it changes both the intensity of convection as well as adds a new conductive flux.  $Nu_{av}$  increases when the lower plate is heated ( $Ra_{uni} > 0$ ) and decreases when the lower plate is cooled ( $Ra_{uni} < 0$ ), and it varies in a qualitatively similar manner as a function of  $\alpha$  for all  $\Omega$ 's with the relevant curves shifted upwards when  $Ra_{uni}$  is increased (Figure 6-28). This increase of  $Nu_{av}$  with an increase of  $Ra_{uni}$  is also dependent upon  $Re$ .

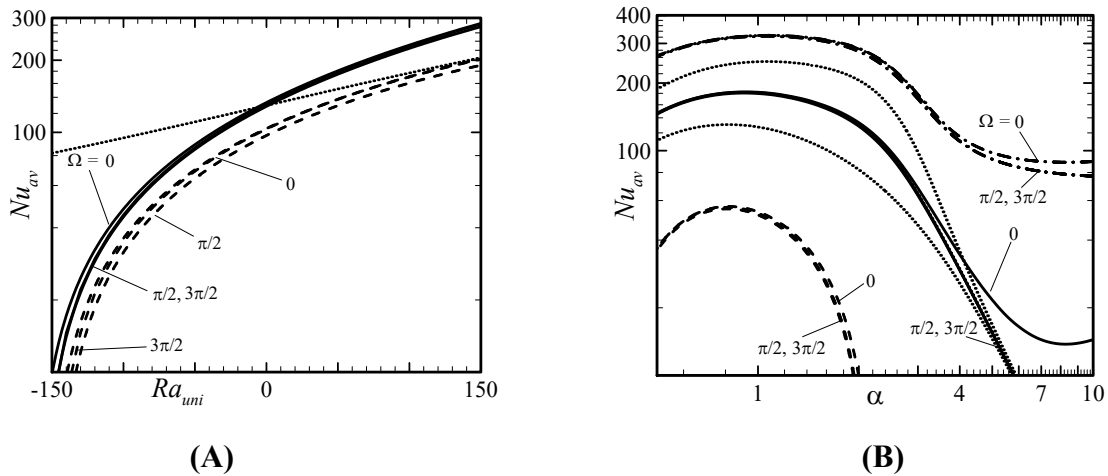


**Figure 6-28:** Variations of  $Nu_{av}$  as a function of (A)  $Ra_{uni}$ , and (B)  $\alpha$ . In (A),  $y_b = 0.01$ ,  $Ra_p = 1000$ ,  $\alpha = 2$ ,  $Re = 1$  (solid lines) and  $Re = 5$  (dashed lines). In (B),  $y_b = 0.01$ ,  $Ra_p = 1000$ ,  $Re = 1$ ,  $Ra_{uni} = -150$  (dashed lines),  $Ra_{uni} = 0$  (solid lines), and  $Ra_{uni} = 150$  (dashed-dotted lines). Dotted lines illustrate results for the smooth lower plate.

The effects of changing the types of fluids are illustrated in Figure 6-29. The most effective  $Nu_{av}$  is found for  $Pr \sim 0.5 - 1$  (such values correspond to gases, including air) with a strong dependence upon  $Re$ .  $Nu_{av}$  varies in a qualitatively similar manner as a function of  $\alpha$  for all  $\Omega$ 's of interest with the relevant curves shifting downwards with an increase of  $Pr$  (Figure 6-29B). Although this change is small for  $Pr \sim 0.71-1$ , a noticeable reduction occurs for  $Pr = 5$  for all phase differences.

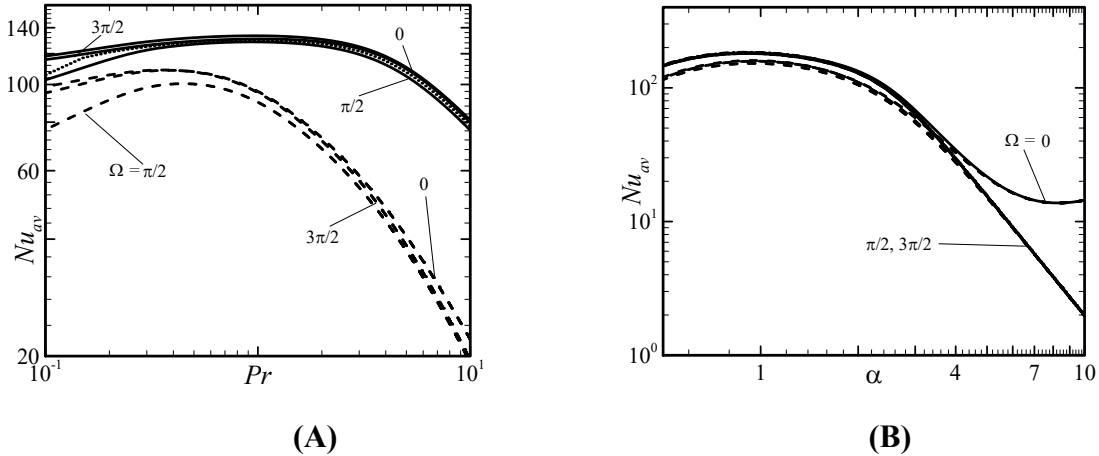


**Figure 6-29:** Variations of  $Nu_{av}$  as a function of (A)  $Pr$ , and (B)  $\alpha$ . In (A),  $y_b = 0.01$ ,  $Ra_p = 1000$ ,  $\alpha = 2$ ,  $Re = 1$  (solid lines) and  $Re = 5$  (dashed lines). In (B),  $y_b = 0.01$ ,  $Ra_p = 1000$ ,  $Re = 1$ ,  $Pr = 0.71$  (solid lines),  $Pr = 1$  (dashed-dotted lines), and  $Pr = 5$  (dashed lines). Dotted lines illustrate results for the smooth lower plate.

## 6.9 Summary

Flow responses to different combinations of geometric irregularities (surface grooves) and heating irregularities (spatial heating pattern) applied at the lower plate have been analyzed. Although no external pressure gradient exists in the flow system, the interaction of the heating and the grooves generates a horizontal pressure force. This induced pressure force (thermal drift) assists with the reduction of the driving force required to maintain movement of the upper plate if a favorable phase difference between heating and the grooves is used. An unfavorable phase difference causes a backward flow in the lower region of the channel, and thereby increases the required driving force. The most favorable phase difference was found to be  $\Omega = \pi/2$ , and the least favorable phase difference was found to be  $\Omega = 3\pi/2$ . The magnitude of the induced pressure force decreases with an increase of the Reynolds number  $Re$ , and increases with an increase of the heating intensity  $Ra_p$ . Hence, the change in the driving force  $\Delta F$  decreases with an increase of  $Re$  and increases with an increase of  $Ra_p$ . An increase in  $Ra_{uni}$  and decrease in the Prandtl number  $Pr$  magnify this effect. Conditions where an external braking force needs to be used to prevent the plate from accelerating have been identified.

## Chapter 7

### 7 Conclusions and Recommendations

#### 7.1 Conclusions

Mechanisms suitable for the control of the driving force in the shear-driven flows utilizing surface and temperature irregularities have been studied. The model problem involves two parallel plates, a moving upper plate which drives the flow and a stationary lower plate. An external force has to be applied to the upper plate to maintain its movement. Changes in the magnitude of this force in response to geometric and heating irregularities at the lower plate were sought. Effects of these irregularities were modelled using the Immersed Boundary Conditions concept. The relevant field equations were solved using an algorithm described by Abtahi, *et al.*, (2016). The spatial discretization relied on the Fourier expansions in the horizontal direction and Chebyshev expansions in the vertical direction.

The analysis began with an investigation of the effects of a spatially periodic heating applied at the stationary, smooth lower plate. An external force was needed to maintain movement of the upper plate at the prescribed rate expressed in terms of the Reynolds number ( $Re$ ). The spatially periodic heating resulted in a sinusoidal temperature distribution of the lower plate whose periodicity was expressed in terms of the wavenumber ( $\alpha$ ) and the amplitude was expressed in terms of the periodic Rayleigh number ( $Ra_P$ ). The difference between the mean temperatures of the upper and lower plates was expressed in terms of the uniform Rayleigh number ( $Ra_{uni}$ ) whose positive values corresponded to the lower plate having a higher temperature. The formation of secondary flows was avoided by using relatively low heating intensities ( $Ra_P < 3000$ ). Heating in the case of a stationary upper surface created counter-rotating rolls driven by the buoyancy effects. When the upper plate moved, the fluid movement between the plates resulted from a competition between the buoyancy-driven effects and the plate-driven motion. The latter created a rectilinear motion that led to the reduction and eventual elimination of the rolls when  $Re$  was large enough ( $Re > 70 - 80$ ). It was found that heating always reduced the force required to

maintain the prescribed movement of the upper plate. The force reduction was a strong function of the heating wavenumber. The largest force reduction was found at  $\alpha \sim 1.8^{-2}$ . This reduction rapidly decreased when the wavenumber was either too high or too low. An increase in  $Ra_{uni}$  and decrease in the Prandtl number ( $Pr$ ) resulted in a larger force reduction. An increase in  $Re$  washed away the rolls and decreased the force reduction with its complete elimination at  $Re \sim 100$ . Use of the proper heating could result in the complete elimination of the driving force. Conditions were identified where an external braking force was needed to prevent the plate from accelerating.

The second step involved the analysis of the effect of surface irregularities placed at the isothermal lower plate. The analysis was limited to irregularities which did not change the mean distance between the plates and was focused on the transverse grooves with arbitrary shapes. It included the analysis of the effects of different spatial groove distributions and was limited to grooves having an amplitude of less than 10% of the channel opening. Different groove shapes were analyzed leading to the formulation of the reduced geometry model. The essence of this model was the demonstration that the replacement of the actual groove shape with the first mode of its Fourier expansion produced an error in the prediction of the required pulling force which is acceptable in most applications. The long wavelength grooves produced spatial flow modulations that resulted in small force increases. The short wavelength grooves resulted in larger force increases due to the blockage effect. This effect was associated with the lift-up phenomenon where the reduction of the gap between the groove sidewalls forced the stream to move away from the grooved plate reducing the effective hydraulic channel opening.

The last step involved analysis of the combined effects of grooves and periodic heating. Only sinusoidal grooves were studied. It was found that the presence of temperature and surface irregularities might either increase or decrease the driving force. The interaction between the heating and the grooves induced a horizontal pressure force (thermal drift) which might act either in the direction of the upper plate movement or opposite. The relative position of the temperature and surface irregularities was expressed in terms of the phase angle ( $\Omega$ ). When the heating patterns overlapped with the groove pattern ( $\Omega = 0$ ), i.e. the wall temperature maxima overlapped with the groove peaks, a reduction of the driving

force was achieved but its magnitude was smaller than that achieved by heating the smooth plate. As the position of the heating changed relative to the position of the grooves, both the magnitude and the direction of the driving force changed. It was found that the maximum force reduction occurred at  $\Omega = \pi/2$ , whereas the maximum increase of the driving force occurred at  $\Omega = 3\pi/2$ . The magnitude of the force augmentation was found to be a strong function of the system wavenumber with the maximum change occurring for  $\alpha \sim 2-3$  with its rapid reduction if either too big or too small  $\alpha$ 's were used. This magnitude was also a strong function of the groove amplitude and the heating intensity. It was also found that an increase of  $Ra_{uni}$  and a decrease of  $Pr$  amplified force augmentation.

It was concluded that the temperature and surface irregularities can be used as effective means for control of the driving force in the shear-driven flows.

## 7.2 Future recommendations

Effects of temperature and surface irregularities in the shear-driven flows were analyzed.

The following questions may be considered for future work:

- This thesis was limited to the analysis of two-dimensional grooves. It would be of interest to determine how the flow would react to the presence of three-dimensional grooves.
- Surface irregularities in the form of transverse grooves were considered. It would be of interest to determine the effects of longitudinal grooves.
- The analysis was limited to low heating intensities to prevent the formation of secondary states. It is of interest to determine conditions leading to the formation of secondary states and how these states may affect the driving force.
- The analysis was focused on the small  $Re$ -flows as stronger flows wash away convection rolls. It is of interest to determine the system response for stronger flows and more intense heating.
- The spatial heating patterns studied in this thesis were limited to sinusoidal forms. It is of interest to determine how the system would respond to heating with other spatial distributions.

- Time-dependent surface topographies were studied in the literature (Bielarz & Kalliadasis, 2003; Mancktelow & Grasmann, 1997). Determining the effect of time variations of surface topographies on the driving force would be of interest.
- Optimization of distributions of the temperature and surface irregularities could increase the range of variations of the driving force. Determination of the optimal distributions would be of interest in the development of flow control devices.



## References

- Abtahi, A., & Floryan, J. M. (2017a). Convective heat transfer in non-uniformly heated corrugated slots. *Phys. Fluids*, 29(10). <https://doi.org/10.1063/1.4989686>
- Abtahi, A., & Floryan, J. M. (2017b). Natural convection and thermal drift. *J. Fluid Mech.*, 826, 553–582. <https://doi.org/10.1017/jfm.2017.426>
- Abtahi, A., & Floryan, J. M. (2017). Natural convection in a corrugated slot. *J. Fluid Mech.*, 815; 537-569.
- Abtahi, A., Hossain, M. Z., & Floryan, J. M. (2016). Spectrally accurate algorithm for analysis of convection in corrugated slots. *Comput. Maths Applics.*, 72(10), 2636–2659. <https://doi.org/10.1016/j.camwa.2016.09.019>
- Abtahi, S. A. (2017). *Convection in Corrugated Slots*. Masters thesis. Department of Mechanical and Materials Engineering, University of Western Ontario.
- Ahlers, G., Grossmann, S., & Lohse, D. (2009). Heat transfer and large scale dynamics in turbulent Rayleigh-Benard convection. *Rev. Mod. Phy.*, 81; 503-537.
- Ashihara, K., & Hashimoto, H. (2010). Theoretical Modeling for Microgrooved Journal Bearings Under Mixed Lubrication. *J. Tribol.*, 132(4), 42101. <https://doi.org/10.1115/1.4002214>
- Aydin, E. M., & Leutheusser, H. J. (1991). Plane-Couette flow between smooth and rough walls. *Exp. Fluids*, 11, 302–312.
- Bechert, D. W., Bruse, M., Van Der Hoeven, J. G. T., & Hoppe, G. (1997). Experiments on drag-reducing surfaces and their optimization with an adjustable geometry. *J. Fluid Mech.*, 338; 59-87.
- Bénard, H. (1900). Les tourbillons cellulaires dans une nappe liquide. *Revue Générale Science Pure et Applique*, 11; 1261-1271.

- Bergeles, A. E. (2001). The implications and challenges of enhanced heat transfer for the chemical process industries. *Chem. Eng. Res. Des.*, 79; 437-444.
- Bielarz, C., & Kalliadasis, S. (2003). Time-dependent free-surface thin film flows over topography. *Phys. Fluids*, 15(9), 2512–2524. <https://doi.org/10.1063/1.1590978>
- Bodenschatz, E., Pesh, W., & Ahlers, G. (2000). Recent developments in Rayleigh-Benard convection. *Annu. Rev. Fluid Mech.*, 32; 709-778.
- Bonn, D., Amarouchène, Y., Wagner, C., Douady, S., & Cadot, O. (2005). Turbulent drag reduction by polymers. *J. Phys. Condens. Matter*, 17(14). <https://doi.org/10.1088/0953-8984/17/14/008>
- Bruse, M., Bechert, D. W., Van Der Hoeven, J. G. T., & Hoppe, G. (1993). Experiments with conventional and with novel adjustable drag-reducing surfaces. *Near Wall Turbulent Flows (Elsevier)*, 719–738.
- Chilla, F., & Schumacher, J. (2012). New perspectives in turbulent Rayleigh-Benard convection. *Eur. Phy. J.*, 35; 58-82.
- Choi, H., Moin, P., & Kim, J. (1991). On the effect of riblets in fully developed laminar channel flows. *Phys. Fluids*, 3; 1892-1896.
- Chu, D. C., & Karniadakis, G. (1993). A direct numerical simulation of laminar and turbulent flow over riblet-mounted surfaces. *J. Fluid Mech.*, 250; 1-42.
- Chu, D., Henderson, R., & Karniadakis, G. (1992). Parallel spectral-element-Fourier simulation of turbulent flow over riblet-mounted surfaces. *Theor. Comput. Fluid Dyn.*, 3; 219-229.
- Darcy, H. (1857). Recherches expérimentales relatives au mouvement de l'eau dans les tuyaux. *Mallet-Bachelier*.
- Deguchi, K., & Nagata, M. (2011). Bifurcations and Instabilities in Sliding Couette flow. *J. Fluid Mech.*, 678; 156-178.

- Desmet, G., & Baron, G. V. (2000). The possibility of generating high-speed shear-driven flows and their potential application in liquid chromatography. *Anal. Chem*, 72(9), 2160–2165.
- Dewan, A., Mahanta, P., Sumithra Raju, K., & Suresh Kumar, P. (2004). Review of passive heat transfer augmentation techniques. *Proc. Instn. Mech. Engrs. A: J. Power Energy*, 218; 509-527.
- Durst, F. (2008). *Fluid mechanics: With problems and solutions, and an aerodynamic laboratory*. Springer-Verlag Berlin Heidelberg. <https://doi.org/10.1007/b138775>
- Floryan, D., & Floryan, J. M. (2015). Drag reduction in heated channels. *J. Fluid Mech.*, 765; 353-395.
- Floryan, J. M. (2002). Centrifugal Instability of Couette Flow over a wavy wall. *Phys. Fluids*, 14, 312–322.
- Floryan, J. M. (2003). Wall-Transpiration-Induced Instabilities in Plane Couette Flow. *J. Fluid Mech.*, 488, 151–188.
- Floryan, J. M. (2012). The thermo-superhydrophobic effect. *Bull. Amer. Phys. Soc.*, 51(1); X.50.00015.
- Freund, G., Pesch, W., & Zimmermann, W. (2011). Rayleigh-Benard convection in the presence of spatial temperature modulations. *J. Fluid Mech.*, 673; 318-348.
- Gamrat, G., Favre-Marinet, M., LePerson, S., Baviere, R., & Ayela, F. (2008). An experimental study and modelling of roughness effects on laminar flow in microchannels. *J. Fluid Mech.*, 594; 399-423.
- Gibbs, J. W. (1898). Fourier's Series. *Nature*, 59; 200.
- Gibbs, J. W. (1899). Fourier's Series. *Nature*, 59; 606.
- Goldstein, D. B., & Tuan, T. C. (1998). Secondary flow induced by riblets. *J. Fluid Mech.*, 363; 115-151.

- Goldstein, D., Handler, R., & Sirovich, L. (1995). Direct numerical simulation of turbulent flow over a modelled riblet covered surface. *J. Fluid Mech.*, 302; 333-376.
- Goluskin, D., & Doering, C. R. (2016). Bounds for convection between rough boundaries. *J. Fluid Mech.*, 804, 370–386. <https://doi.org/10.1017/jfm.2016.528>
- Gottlieb, D., & Shu, C. W. (1997). On the Gibbs phenomena and its resolution. *SIAM Rev.*, 39(4); 644-668.
- Hagen, G. (1854). Über den Einfluss der temperature auf die Bewegung des Wasser in Röhren. *Math. Abh. Akad. Wiss.*, 17–98.
- Ho, C. M., & Tai, Y. C. (1998). Micro-electro-mechanical systems (MEMS) and fluid flows. *Annu. Rev. Fluid Mech.*, 30; 579-612.
- Hossain, M. Z. (2011). *Convection Due to Spatially Distributed Heating*. PhD dissertation. Department of Mechanical and Materials Engineering, University of Western Ontario.
- Hossain, M. Z., Floryan, D., & Floryan, J. M. (2012). Drag reduction due to spatial thermal modulations. *J. Fluid Mech.*, 713; 398-419.
- Hossain, M. Z., & Floryan, J. M. (2014). Natural convection in a fluid layer periodically heated from above. *Phys. Rev. E*, 90; 023015.
- Hossain, M. Z., & Floryan, J. M. (2015). Mixed convection in a periodically heated channel. *J. Fluid Mech.*, 768; 51-90.
- Hossain, M. Z., & Floryan, J. M. (2016). Drag reduction in a thermally modulated channel. *J. Fluid Mech.*, 791; 122-153.
- Hughes, G. O., & Griffiths, R. W. (2008). Horizontal convection. *Annu. Rev. Fluid Mech.*, 40; 185-208.
- Hurst, E., Yang, Q., & Chung, Y. M. (2014). The effect of Reynolds number on turbulent drag reduction by streamwise travelling waves. *J. Fluid Mech.*, 759, 28–55. <https://doi.org/10.1017/jfm.2014.524>

- Husain, S. Z., & Floryan, J. M. (2013). Efficient solvers for the IBC method. *Comput. Fluids*, 84; 127-140.
- Joseph, P., Cottin-Bizonne, C., Benoit, J. M., Ybert, C., Journet, C., Tabeling, P., & Bocquet, L. (2006). Slippage of water past superhydrophobic carbon nanotube forests in microchannels. *Phys. Rev. Lett.*, 97; 156104.
- Ligrani, P. M., Oliviera, M. M., & Blaskovich, T. (2003). Comparison of heat transfer augmentation techniques. *AIAA Journal*, 41; 337-362.
- Lohse, D., & Xia, K. Q. (2010). Small scale properties of turbulent Rayleigh-Benard convection. *Annu. Rev. Fluid Mech.*, 42; 335-364.
- Mahfoze, O., & Laizet, S. (2017). Skin-friction drag reduction in a channel flow with streamwise-aligned plasma actuators. *Int. J. Heat Fluid Fl.*, 66, 83–94. <https://doi.org/10.1016/j.ijheatfluidflow.2017.05.013>
- Malevich, A. E., Mityushev, V. V, & Adler, P. M. (2008). Couette flow in channels with wavy walls. *Acta Mech.*, 197,247-283.
- Mancktelow, N. S., & Grasemann, B. (1997). Time-dependent effects of heat advection and topography on cooling histories during erosion. *Tectonophysics*, 270(3–4), 167–195. [https://doi.org/10.1016/S0040-1951\(96\)00279-X](https://doi.org/10.1016/S0040-1951(96)00279-X)
- Maxworthy, T. (1997). Convection into domains with open boundaries. *Annu. Rev. Fluid Mech.*, 29; 327-371.
- McCoy, J. H., Brunner, W., Pesch, W., & Bodenschatz, E. (2008). Self organization of topological defects due to applied constraints. *Phys. Rev. Lett.*, 101; 254102.
- Mittal, R., & Iaccarino, G. (2005). Immersed boundary methods. *Annu. Rev. Fluid Mech.*, 37; 239-261.
- Mohammadi, A. (2013). *Flows in grooved channels*. PhD dissertation. Department of Mechanical and Materials Engineering, University of Western Ontario.

- Mohammadi, A., & Floryan, J. M. (2012). Mechanism of drag reduction by surface corrugation. *Phys. Fluids*, 24; 013602.
- Mohammadi, A., & Floryan, J. M. (2013a). Groove optimization for drag reduction. *Phys. Fluids*, 25; 113601.
- Mohammadi, A., & Floryan, J. M. (2013b). Pressure losses in grooved channels. *J. Fluid Mech.*, 725; 23-54.
- Mohammadi, A., & Floryan, J. M. (2014). Effects of longitudinal grooves on the Couette-Poiseuille flow. *J. Theor. Comp. Fluid Mech.*, 28; 549-572.
- Moody, L. F. (1944). Friction factors for pipe flow. *Trans. ASME*, 66; 671-684.
- Moradi, H. V. (2014). *Effects of surface topographies on heat and fluid flows*. PhD dissertation. Department of Mechanical and Materials Engineering, University of Western Ontario.
- Moradi, H. V., & Floryan, J. M. (2013). Flows in annuli with longitudinal grooves. *J. Fluid Mech.*, 716; 280-315.
- Niavrani, A., & Priezjev, N. V. (2009). The effective slip length and vortex formation in laminar flow over a rough surface. *Phys. Fluids*, 21 (052105).
- Nikuradse, J. (1933). Strömungsgesetze in Rauhen Rohren. *VDI-Forschungsheft*.
- Ou, J., Perot, J. B., & Rothstein, J. P. (2004). Laminar drag reduction in microchannels using ultrahydrophobic surfaces. *Phys. Fluids*, 16; 4635-4643.
- Ou, J., & Rothstein, J. P. (2005). Direct velocity measurements of the flow past drag reducing ultrahydrophobic surfaces. *Phys. Fluids*, 17; 103606.
- Papautsky, I., Brazzle, J., Ameel, T., & Frazier, A. B. (1999). Laminar fluid behavior in microchannels using micropolar fluid theory. *Sensor. Actuat. A-Phys.*, 73; 101-108.
- Peskin, C. S. (2002). The immersed boundary method. *Acta Numer.*, 11; 479-517.

- Priezjev, N. V., & Troian, S. M. (2006). Influence of periodic wall roughness on the slip behavior at liquid/solid interfaces: molecular-scale simulations versus continuum predictions. *J. Fluid Mech.*, 554; 25-46.
- Quere, D. (2008). Wetting and roughness. *Annu. Rev. Mater.*, 38; 71-99.
- Rayleigh, J. W. S. (1916). On convection currents in a horizontal layer of fluid, when the higher temperature is on the under side. *Phil. Mag.*, 32; 529-546.
- Reyssat, M., Yeomans, J. M., & Quere, D. (2008). Impalement of fakir drops. *Europhys. Lett.*, 81; 26006.
- Rim, K. S., & Yun, B. I. (2013). Gibbs phenomenon removal by adding heaviside functions. *Adv. Comp. Math*, 38 (4); 683-699.
- Romanov, V. A. (1972). Stability of plane-parallel Couette flow. *Func. Anal. Applics.*, 7; 137-146.
- Rothstein, J. P. (2010). Slip of superhydrophobic surfaces. *Annu. Rev. Fluid Mech.*, 42; 89-109.
- Sahlin, F., Glavatskih, S. B., Almqvist, T., & Larsson, R. (2005). Two-Dimensional CFD-Analysis of Micro-Patterned Surfaces in Hydrodynamic Lubrication. *J. Tribol.*, 127(1), 96. <https://doi.org/10.1115/1.1828067>
- Samaha, M. A., Tafreshi, H. V., & Gad-El-Hak, M. (2011). Modeling drag reduction and meniscus stability of superhydrophobic surfaces comprised of random roughness. *Phys. Fluids*, 23; 012001.
- Segawa, T., Mizunuma, H., Murakami, K., Li, F. C., & Yoshida, H. (2007). Turbulent drag reduction by means of alternating suction and blowing jets. *Fluid Dyn. Res.*, 39(7), 552–568. <https://doi.org/10.1016/j.fluidyn.2007.01.002>
- Seiden, G., Weiss, S., McCoy, J. H., Pesch, W., & Bodenschatz, E. (2008). Pattern forming system in the presence of different symmetry breaking mechanisms. *Phys. Rev. Lett.*,

101; 214503.

- Sharp, K. V, & Adrian, R. J. (2004). Transition from laminar to turbulent flow in liquid filled microtubes. *Exp. Fluids*, 36; 741-747.
- Siddique, M., Khaled, A. R. A., Abdulhafiz, N. I., & Boukhary, A. Y. (2011). Recent advances in heat transfer enhancements: A review report. *Int. J. Chem. Eng.*, 1–28.
- Siggers, J. H., Kerswell, R. R., & Balmforth, N. J. (2004). Bounds on horizontal convection. *J. Fluid Mech.*, 517; 55-70.
- Sobhan, C. B., & Garimella, S. V. (2001). A comparative analysis of studies on heat transfer and fluid flow in microchannels. *Microsc. Therm. Eng.*, 5; 293-311.
- Szumbariski, J., & Floryan, J. M. (1999). A direct spectral method for determination of flows over corrugated boundaries. *J. Comput. Phys.*, 153; 378-402.
- Toppaladoddi, S., Succi, S., & Wettlaufer, J. S. (2015). Tailoring boundary geometry to optimize heat transport in turbulent convection. *Europhys. Lett.*, 111(4). <https://doi.org/10.1209/0295-5075/111/44005>
- Truesdell, R., Mammoli, P., Vorobieff, P., Van Swol, P., & Brinker, C. J. (2006). Drag reduction on a patterned superhydrophobic surface. *Phys. Rev. Lett.*, 97; 044504.
- Valdés, J. R., Izquierdo, S., Miana, M. J., & Jiménez, M. A. (2012). Modelling of Couette flow in microchannels with textured surfaces. *Proceedings of the Institution of Mechanical Engineers, Part J: Journal of Engineering Tribology*, 226(1), 14–22. <https://doi.org/10.1177/1350650111416298>
- Virk, P. S. (1975). Drag reduction fundamentals. *AIChE Journal*, 21(4), 625–656. <https://doi.org/10.1002/aic.690210402>
- Walsh, M. J. (1980). Drag characteristics of V-groove and transverse curvature riblets. In G. R. Hough (Ed.), *Viscous Drag Reduction* (Vol. 72, pp. 168–184). AIAA.
- Walsh, M. J. (1983). Riblets as a viscous drag reduction technique. *AIAA J.*, 72; 485-486.



- Walsh, M. J., & Lindemann, A. M. (1984). Optimization and application of riblets for turbulent drag reduction. In *AIAA 22nd Aerospace Sciences Meeting* (pp. 84–347). Reno, NV.
- Wang, L., Wang, W., Wang, H., Ma, T., & Hu, Y. (2014). Numerical Analysis on the Factors Affecting the Hydrodynamic Performance for the Parallel Surfaces With Microtextures. *J. Tribol.*, *136*(2), 21702. <https://doi.org/10.1115/1.4026060>
- Weinstein, S. J., & Ruschak, K. J. (2004). Coating Flows. *Annu. Rev. Fluid Mech.*, *36*(1), 29–53. <https://doi.org/10.1146/annurev.fluid.36.050802.122049>
- Weiss, S., Seiden, G., & Bodenschatz, E. (2012). Pattern formation in spatially forced thermal convection. *New J. Phys.*, *14*; 053010.
- Xia, G., Chai, L., Zhou, M., & Wang, H. (2011). Effects of structural parameters on fluid flow and heat transfer in a microchannel with aligned fan-shaped re-entrant cavities. *Int. J. Therm. Sci.*, *50*; 411-419.
- Yamamoto, A., Hasegawa, Y., & Kasagi, N. (2013). Optimal control of dissimilar heat and momentum transfer in fully developed turbulent channel flow. *J. Fluid Mech.*, *733*; 189-230.
- Zhou, M., Li, J., Wu, C., Zhou, X., & Cai, L. (2011). Fluid drag reduction on superhydrophobic surfaces coated with carbon nanoforest tubes. *Soft Matt.*, *7*; 4391-4396.

## Appendices

### Appendix A: Recurrence formulae and Chebyshev inner products

Chebyshev polynomials satisfy the following relations

$$T_0(y) = 1, \quad T_1(y) = y, \quad T_{k+1}(y) = 2yT_k(y) - T_{k-1}(y), \quad \text{for } k \geq 2 \quad (\text{A.1a-c})$$

$$D^n T_{k+1}(\hat{y}) = 2nD^{n-1}T_k(\hat{y}) + 2\hat{y}D^n T_k(\hat{y}) - D^n T_{k-1}(\hat{y}), \quad \text{for } n \geq 1 \quad (\text{A.2})$$

The inner product of two Chebyshev polynomials are defined as,

$$\langle T_j(\hat{y}), T_k(\hat{y}) \rangle = \int_{-1}^1 T_j(\hat{y})T_k(\hat{y})\omega(\hat{y}) d\hat{y}, \quad (\text{A.3})$$

where  $\omega(\hat{y}) = (1 - \hat{y}^2)^{-1/2}$  is the weight function. Its evaluation results in

$$\langle T_j, T_k \rangle = \frac{\pi}{2} C_k \delta_{ik} \begin{cases} 0, & \text{for } j \neq k \\ \pi, & \text{for } j = k = 0 \\ \pi/2, & \text{for } j = k > 0 \end{cases} \quad (\text{A.4})$$

where  $\delta_{i,k}$  is the Kronecker delta and  $C_k = \begin{cases} 2, & k = 0 \\ 1, & k \geq 1 \end{cases}$

The first, second, and fourth derivatives of a Chebyshev polynomial can be expressed as,

$$DT_k = 2k \sum_{l=0}^{l=k-1} \frac{1}{c_l} T_l, \quad \text{for } k - l = \text{odd}, k \geq l+1 \quad (\text{A.5a})$$

$$D^2 T_k = \sum_{l=0}^{l=k-2} \frac{1}{c_l} (k^2 - l^2) T_l, \quad \text{for } k - l = \text{even}, k \geq l+2 \quad (\text{A.5b})$$

$$D^3 T_k = \sum_{l=0}^{l=k-2} \frac{1}{c_l} (k^2 - l^2) \left[ 2l \sum_{z=0}^{z=l-1} \frac{1}{c_z} T_z \right], \quad \text{for } k - l = \text{even}, l - z = \text{odd},$$

$$\text{when } k \geq l+2, \quad l \geq z+1 \quad (\text{A.5c})$$

$$D^4 T_k = \sum_{l=0}^{l=k-2} \frac{1}{c_l} k(k^2 - l^2) D^2 T_l, \quad \text{for } k - l = \text{even}, k \geq l+2 \quad (\text{A.5d})$$

The following inner products of the Chebyshev polynomials can be evaluated explicitly as,

$$\langle T_j, DT_k \rangle = k\pi, \quad \text{for } k-j=\text{odd}, k \geq j+1 \quad (\text{A.6a})$$

$$\langle T_j, D^2T_k \rangle = k(k^2 - j^2)\frac{\pi}{2}, \quad \text{for } k-j=\text{even}, k \geq j+2 \quad (\text{A.6b})$$

$$\langle T_j, D^3T_k \rangle = \sum_{i=0}^{l=k-2} \frac{1}{C_i} k(k^2 - l^2) [\pi l],$$

$$\text{for } \begin{cases} k-j = \text{even}, & k \geq l+2 \\ l-j = \text{odd}, & l \geq j+1 \end{cases} \quad (\text{A.6c})$$

$$\langle T_j, D^4T_k \rangle = \sum_{i=0}^{l=k-2} \frac{1}{C_i} k(k^2 - l^2) \left[ l \left( l^2 - j^2 \frac{\pi}{2} \right) \right],$$

$$\text{for } \begin{cases} k-l = \text{even}, & k \geq l+2 \geq j+4 \\ i-j = \text{even}, & l \geq j+2 \end{cases} \quad (\text{A.6d})$$

The integral of a Chebyshev polynomial  $I_k(\hat{y}) = \int_{-1}^{\hat{y}} T_k(\hat{y})$  can be evaluated analytically as,

$$I_0(\hat{y}) = T_1(\hat{y}) + 1, \quad (\text{A.7a})$$

$$I_1(\hat{y}) = \frac{T_2(\hat{y})-1}{4}. \quad (\text{A.7b})$$

## Appendix B: Evaluation of viscous and pressure forces at the lower plate

The surface stresses acting on the fluid at the lower plate ( $\sigma_L$ ) are expressed as

$$\sigma_L = [n_{x,L} \quad n_{y,L}] \begin{bmatrix} \tau_{xx} - p & \tau_{xy} \\ \tau_{yx} & \tau_{yy} - p \end{bmatrix}_{yL} \quad (\text{B-1})$$

where

$$\tau_{xx} = 2 \frac{\partial u}{\partial x}, \quad \tau_{xy} = \tau_{yx} = \frac{\partial u}{\partial y} + \frac{\partial v}{\partial x}, \quad \tau_{yy} = 2 \frac{\partial v}{\partial y} \quad (\text{B-2})$$

denote the viscous component of the stress tensors and

$$[n_{x,L} \quad n_{y,L}] = N_L [-\alpha y_b \sin(\alpha x) \quad -1] \quad (\text{B-3})$$

are components of the normal unit vector with  $N_L = [1 + (\alpha y_b \sin(\alpha x))^2]^{-1/2}$ . The  $x$  and  $y$  components of the surface stresses are expressed as

$$\sigma_{x,L} = \sigma_{xv,L} + \sigma_{xp,L} = N_L \left[ -2\alpha y_b \sin(\alpha x) \frac{\partial u}{\partial x} - \left( \frac{\partial u}{\partial y} + \frac{\partial v}{\partial x} \right) \right]_{yL} + N_L [\alpha y_b \sin(\alpha x) p]_{yL}. \quad (\text{B-4})$$

$$\sigma_{y,L} = \sigma_{yv,L} + \sigma_{yp,L} = N_L \left[ -\alpha y_b \sin(\alpha x) \left( \frac{\partial u}{\partial y} + \frac{\partial v}{\partial x} \right) - 2 \frac{\partial v}{\partial y} \right]_{yL} + N_L [p]_{yL} \quad (\text{B-5})$$

where  $\sigma_{xv,L}, \sigma_{yv,L}$  are generated by viscous effects while  $\sigma_{xp,L}, \sigma_{yp,L}$  are generated by the pressure. The  $x$ - and  $y$ -components of forces acting on the fluid per unit length in the  $x$  – direction are

$$F_{x,L} = F_{xv,L} + F_{xp,L} = \lambda^{-1} \int_0^\lambda (\sigma_{xv,L} + \sigma_{xp,L}) N_L^{-1} dx. \quad (\text{B-6})$$

$$F_{y,L} = F_{yv,L} + F_{yp,L} = \lambda^{-1} \int_0^\lambda (\sigma_{yv,L} + \sigma_{yp,L}) N_L^{-1} dx. \quad (\text{B-7})$$

## Curriculum Vitae

**Name:** Sakib Shadman

**Post-secondary Education and Degrees:** Islamic University of Technology  
Gazipur, Dhaka, Bangladesh  
2012-2016 B.Sc. (Mechanical Engineering)

The University of Western Ontario  
London, Ontario, Canada  
2016-2018 M.E.Sc (Mechanical and Materials Engineering)

**Honours and Awards:** Western Graduate Research Scholarship  
2016-2018

Organization of Islamic Cooperation (OIC) Scholarship  
2013-2016

**Related Work Experience** Teaching Assistant  
The University of Western Ontario  
2016-2018

Lecturer  
Sonargaon University  
Dhaka, Bangladesh  
2016-2016